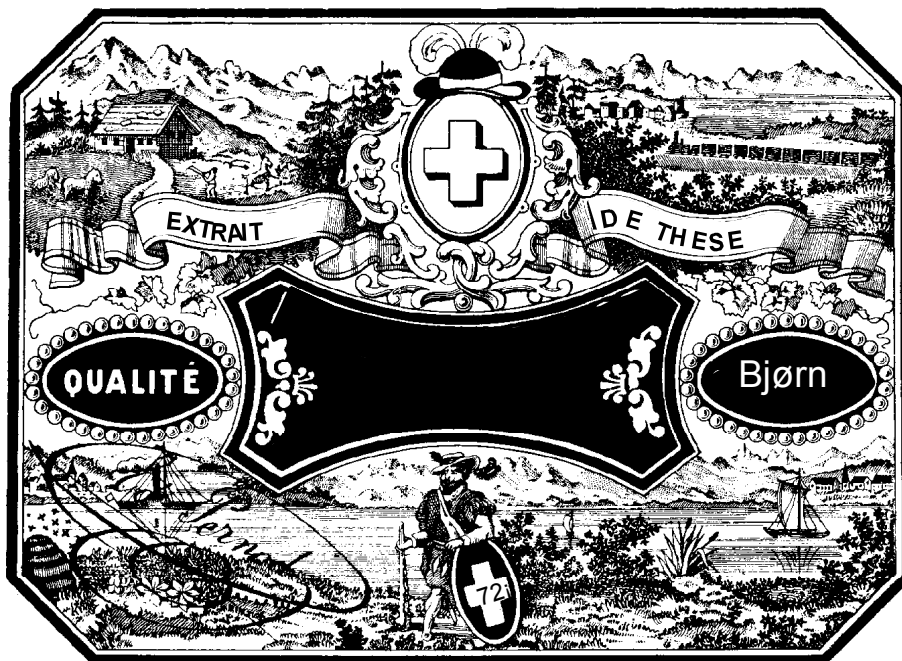


# NUCLEATION AND GROWTH IN METAL-ON-METAL EPITAXY : THE INFLUENCE OF STRAIN AND SURFACE RECONSTRUCTION



THÈSE N° 1773 (1998)

PRÉSENTÉE AU DÉPARTEMENT DE PHYSIQUE

ÉCOLE POLYTECHNIQUE FÉDÉRALE DE LAUSANNE

POUR L'OBTENTION DU GRADE DE DOCTEUR ÈS SCIENCES

PAR

Björn FISCHER

# Résumé

Cette thèse a pour cadre la croissance épitaxiale de couches minces métalliques déposées en phase gazeuse par jet moléculaire. Son but est de mieux comprendre les effets liés à la présence d'un substrat non homogène ou d'un désaccord de maille entre le substrat et le dépôt sur les processus microscopiques régissant la nucléation et la croissance. Les études ont été effectuées à l'aide d'un microscope à effet tunnel à température variable.

Plusieurs systèmes ont été étudiés durant cette thèse. Le premier d'entre eux est la croissance homoépitaxiale de l'aluminium sur l'Al(111). Ce système peut être considéré comme notre système de référence car 1) le substrat est homogène (sur une même terrasse) et donc la diffusion est parfaitement isotrope, 2) le substrat et le dépôt sont de même nature, si bien qu'aucune contrainte due au désaccord de maille ne perturbe la croissance. Pour ce système une barrière de diffusion pour les atomes déposés de  $42 \pm 4$  meV ainsi qu'une fréquence d'essai de  $\approx 10^7 \text{ s}^{-1}$  ont été déterminées en appliquant la théorie de la nucléation. Le deuxième système étudié est la croissance de l'aluminium sur l'Au(111). Contrairement à l'Al(111) la surface (111) de l'or n'est pas homogène car elle présente une reconstruction de surface dite en "chevron" constituée de dislocations. Les paramètres de maille des deux composants de ce système ne diffèrent toutefois que de 0.75%, et par conséquent, les effets de contraintes sont supposés jouer un rôle négligeable lors de la nucléation et de la croissance. Les mesures ont permis de montrer que la reconstruction modifie de façon importante la diffusion d'atomes. A basse température, les atomes déposés ne peuvent pas diffuser librement sur la surface mais sont confinés entre deux dislocations de la

reconstruction. Une barrière de  $30 \pm 5$  meV et une fréquence d'essai de  $\approx 10^3$  s<sup>-1</sup> ont été mesurées pour la diffusion dans les régions pseudomorphes situées entre deux dislocations. Ce n'est qu'à plus haute température que les atomes déposés acquièrent une énergie suffisante pour pouvoir franchir les dislocations. Des simulations Monte-Carlo cinétiques ont été effectuées de façon à chiffrer l'importance de cette barrière. Enfin, à partir de 220 K les deux composants du système forment un alliage ce qui entraîne une modification de la reconstruction.

Il est intéressant de noter que pour ces deux premiers systèmes, les valeurs obtenues pour les barrières de diffusion sont les plus faibles jamais observées pour des systèmes métal sur métal. De même, les fréquences d'essai sont inférieures de plusieurs ordres de grandeur à la valeur "universelle" habituellement obtenue pour les systèmes métal sur métal.

Le dernier système étudié est le Cu sur le Ni(100). Ce système permet d'étudier l'effet des contraintes liées au désaccord de maille (+2.6%) sur la croissance. Nous avons constaté que ces effets se traduisent par des modifications de la morphologie des îlots déjà pour des recouvrements très faibles (0.03 monocouches). Les îlots contenant plus de 500 atomes apparaissent ramifiés, bien que pour des substrats quadratiques seuls des îlots de formes compactes sont attendues (des îlots ramifiés ne sont prévus que pour des températures extrêmement basses et pour des conditions de croissance loin de l'équilibre thermodynamique). Nous démontrons que ces structures permettent une relaxation optimale des contraintes sur le pourtour des îlots. Un second mécanisme de relaxation de contrainte a été révélé par la croissance multicouche. Dès lors que la ramification des îlots ne permet plus une relaxation de contrainte suffisante, un second mécanisme prend le relais: le système déplace des rangées monoatomiques de Cu de leur position d'équilibre vers une position de plus faible coordination. Cette relaxation donne lieu à une structure en franges dépassant légèrement de la surface. A chaque couche de cuivre supplémentaire ces franges s'élargissent d'un atome pour finalement donner naissance à des facettes intérieures d'orientation (111).

# Abstract

The objective of this thesis is to contribute to a better understanding of strain effects in metal epitaxial growth. On the one hand, strain can induce surface reconstructions, which have a strong impact on the growth kinetics. On the other hand, for lattice mismatched systems, strain is always present within the epitaxial film. To attack these problems, measurements employing variable temperature scanning tunneling microscopy (STM) were performed for several metal on metal systems.

The first system is the homoepitaxy of aluminum on the Al(111) surface. This system can be considered as a "reference" system since 1) the substrate is homogeneous thus the diffusion is perfectly isotropic, 2) substrate and deposit are of the same nature, and thus strain effects play no role during growth. For this system a diffusion barrier for adatom migration of  $42 \pm 4$  meV and an attempt frequency of about  $10^7$  s<sup>-1</sup> have been obtained applying mean-field nucleation theory. The second topic is the heteroepitaxial growth of Al on the Au(111) surface. In contrast to Al(111), the close-packed (111) surface of gold is not homogeneous, as it exhibits a surface reconstruction ("chevron" structure) consisting of dislocations lines. The lattice misfit for the materials is 0.75%, and thus strain effects are expected to play a negligible role during nucleation and growth. Our data demonstrate that the reconstruction perturbs in a significant manner the diffusion behaviour of deposited adatoms. At low temperature deposited adatoms cannot diffuse freely on the substrate but are confined within two dislocation lines of the reconstruction. A diffusion barrier of  $30 \pm 5$  meV and an attempt frequency of  $\approx 10^3$  s<sup>-1</sup> have been derived for the diffusion in the pseudomorphic areas located between two dislocations lines. Adatoms can only cross

the dislocations at temperatures exceeding  $\approx 200$  K. Kinetic Monte-Carlo simulations have been performed in order to obtain a quantitative estimation of this effective barrier which was determined to 560 meV. At even higher temperatures ( $> 220$  K) surface alloy formation sets in, whereupon a surface layer with increased atom density and hexagonal dislocation pattern evolves.

A striking results for both growth of Al on Al(111) and Au(111) is that the diffusion barriers obtained for these two systems are the lowest ever measured for metal on metal systems. These extremely low barriers correlate with similarly drastic lowered attempt frequencies, several orders of magnitude lower than the "universal" value generally obtained for metal on metal systems. It is suggested that this behaviour is a consequence of a diffusion mechanism which cannot be simply understood in the traditional "hopping" picture.

Finally, growth of Cu on the Ni(100) surface was investigated. This system is well-suited to study the effects of strain on nucleation and growth (lattice mismatch +2.6%). Already at coverages as low as 0.03 monolayer, we found strain-driven growth morphologies. Islands larger than 500 atoms are ramified. This is a striking observation, as for square lattices only compact islands are expected (non-compact islands are only predicted for extremely low temperatures or growth conditions far away from equilibrium). We demonstrate that these ramified structures are determined by the efficient strain relaxation at step-edges.

# Contents

Résumé .....	i
Abstract.....	iii
<b>1 Introduction.....</b>	<b>1</b>
<b>2 Experimental .....</b>	<b>5</b>
2.1 Setup of the experiment.....	5
2.2.1 Introduction .....	12
2.2.2 Calculation of eigenfrequencies .....	12
2.2.3 Experimental setup and results.....	13
2.3 Sample preparation.....	20
<b>3 Nucleation and Growth.....</b>	<b>23</b>
3.1 Growth scenarios .....	23
3.1.1 Thermodynamics growth.....	23
3.1.2 Kinetics - atomic processes .....	25
3.2 Basics of mean-field nucleation theory.....	28
<b>4 Nucleation and self diffusion of Al on Al(111).....</b>	<b>31</b>
4.1 Introduction.....	31
4.2 STM observations and analysis.....	32
4.2.1 Nucleation and diffusion .....	32
4.2.2 Islands shapes .....	37

4.3	Comparison of STM results with ab initio calculations.....	39
4.4	Conclusion.....	42
<b>5</b>	<b>Nucleation kinetics on a substrate with dislocations: Al/Au(111) .....</b>	<b>43</b>
5.1	Introduction .....	43
5.2	The ( $\sqrt{3} \times 22$ ) reconstruction of the Au(111) surface .....	45
5.3	Nucleation and diffusion behaviour .....	47
5.4	Kinetic Monte-Carlo simulations .....	54
5.5	Comparison of the $\{E_m, v_0\}$ pair for several metal on metal systems.....	60
5.6	Conclusion.....	63
<b>6</b>	<b>Growth and surface alloying of Al on Au(111) at room temperature.....</b>	<b>65</b>
6.1	Introduction .....	65
6.2	Island and thin film morphology.....	66
6.3	Al–Au surface alloy formation.....	69
6.4	Conclusion.....	75
<b>7</b>	<b>Strain relief in submonolayer islands of Cu on Ni(100).....</b>	<b>77</b>
7.1	Introduction .....	77
7.2	Characterization of the island shape transition .....	81
7.3	Quantitative analysis of the island shape transition .....	85
7.4	Thermodynamics of coherently strained islands .....	88
7.5	Relaxation of edge atoms at the island perimeter.....	91
7.6	Determination of strain energy from island shape.....	95
7.7	Conclusion.....	97
<b>8</b>	<b>Outlook</b>	<b>98</b>
	<b>Acronyms .....</b>	<b>101</b>
	<b>Bibliography.....</b>	<b>102</b>

# Chapter 1

## Introduction

Thin film structures with smooth interfaces are of fundamental importance in electronics, optics, and magnetism. Electronic devices, coatings, displays, sensors, and numerous other technologies all depend on the quality of the deposited thin films. As the field of thin films develops rapidly, new discoveries and applications appear, such as vapor phase growth of complex inorganic materials (e.g. perovskite structure high- $T_c$  superconductors [1]) or thin film growth of nematic liquid crystals for use in display technology [2]. Even if well-established methods exist for the production of high-quality films, there is still a strong interest in alternative methods which might be less expensive, more reliable, or capable of producing films with novel or improved properties. Examples of technological applications of thin films include quantum well laser diodes [3], new magnetic recording media [4], organic displays [2], and hard inorganic coatings used to increase the life time of cutting tools or for tribological applications [5]. The performance of such devices depends sensitively on the ability to grow ultrathin epitaxial films of selected material with atomic precision.

A commonly used technique to produce thin epitaxial layers is molecular beam epitaxy (MBE). Nowadays MBE is extensively used to grow epitaxial multilayers for technological applications (e.g. semiconductor devices). However, MBE may also be a powerful tool to create model systems for one of the fastest growing research fields: nanoscience. There are several approaches to fabricate nanostructures on a surface, all of them have their specific advantages and disadvantages. The probably most spectacular one is direct atomic manipulation with scanning-probe methods [6-8], where the desired structures are assembled atom by atom with the tip of a scanning



tunneling microscope. Though arbitrary atomic scale structures can be created using such techniques, the main drawback of this method is its time consuming serial character. Another attractive method, based on kinetic limitations, is self-organized growth: At low substrate temperatures and appropriate deposition rates the dominance of kinetics in epitaxial growth can be used to tailor artificial structures. By exploiting the dependence of the mobility of adsorbed atoms on the symmetry of the surfaces, the substrate temperature and on the deposition flux, it is possible to grow nanostructures of varying shape and size [9]. This method has the advantage of creating a large number of structures simultaneously in a parallel process [9]. A drawback, however, is the often limited degree of control over the atomic motions in diffusion and nucleation processes. Here a more detailed insight into the processes involved can help to find novel ways to optimize, for instance, the uniformity of the resulting nano-structures. The objective of this thesis is to contribute to a better understanding of strain effects on microscopic processes involved in thin film growth and self-assembly on metal surfaces.

The first part of this thesis focuses on diffusion and growth phenomena on an inhomogeneous substrate, which results from surface strain; our model system is the nucleation and growth of Al on the Au(111) surface. In this context surface reconstruction and surface alloying which are two physical mechanisms that may induce changes in the surface morphology and thereby affect diffusion and nucleation processes are briefly introduced in the following.

- *Surface reconstruction:* The outermost layer of most metals is relaxed due to the smoothing of the surface electronic charge density, but the in-plane structure retains generally the bulk termination. However, some clean metal surfaces are known to spontaneously reconstruct, i.e. the in-plane surface structure deviates from the bulk plane structure. The most prominent examples are: the  $(1 \times 2)$  missing-row reconstruction on the fcc(110) surfaces of Pt and Au [10], the  $(7 \times 7)$  reconstruction of Si(111), and the  $(\sqrt{3} \times 22)$  "chevron" reconstruction of Au(111) [11]. The charge transfer resulting from the adsorption of molecules or atoms from the gas phase onto a metal surface can also induce a variety of reconstructions on surfaces which are otherwise stable [12]. The (110) surfaces of Pd, Ag, Cu and Ni are unreconstructed in its clean state, but they show an inherent tendency towards reconstruction when certain molecules are adsorbed. E.g. even the weak chemisorption of hydrogen is known to induce a  $(1 \times 2)$  missing-row reconstruction on the Ni(110) and the Pd(110) surfaces [13, 14].

• *Surface alloying:* During heteroepitaxial growth, i.e. when metal A is deposited on metal B, the growing adlayer and the substrate may intermix. In a number of cases it has been shown that elements intermix at the surface although they are immiscible in the bulk [15, 16]. The driving force for the so called surface alloying can be the reduction of the strain energy related to the atomic size mismatch of the two constituents [17]. Moreover, in systems which are known to form stable bulk alloys, the kinetics of surface mixing turned out to be important, as the nucleation kinetics in the initial stages of growth is substantially altered with respect to systems growing phase separated [18]. Pd on Cu(100), Au on Ni(111) or Ag on Cu(110) are examples for such systems [19].

The second part of this thesis is focusing on strain effects resulting from the lattice mismatch between the substrate and the deposit; in particular the influence of strain on the island shape is studied for the Cu on Ni(100) system. For heteroepitaxial growth, the lattice misfit is of fundamental importance. Depending on the value of the mismatch the growth morphology can be strongly modified, whereby strain relief mechanisms play an important role. In particular, the effects of the substrate geometry have to be considered: e.g. on fcc(111) surfaces two differing adsorption sites with similar adsorption energy exist, fcc and hcp. Due to this particularity of fcc(111) surfaces, strain can be accommodated easily by the introduction of fcc-hcp stacking faults. On fcc square lattices however, this mechanism is symmetrically impossible and the system has to find different means for strain relief.

The present thesis is structured as follows: the experimental results and their interpretation are presented in detail in chapters 4 to 7. These four chapters constitute the bulk part of this work and are largely written in the format of articles.

In chapter 2 the experimental setup is presented. It contains a brief description of the sample-holder, the variable temperature STM and a discussion on the vibrational behaviour of our STM and sample-holder. The preparation routines for all systems are also discussed.

Chapter 3 comprises the basics of nucleation and growth as well as the principle results from nucleation mean-field theory necessary for the analysis of our experimental results.

Chapters 4, 5 and 6 illustrate the effect of surface reconstruction and surface alloying on the diffusion, nucleation and growth of Al atoms on a close-packed metal surface. In chapter 4 we present our results for the diffusion and nucleation behaviour of homoepitaxy of Al on the Al(111) surface. The saturation islands density and the

shapes of aluminum islands are analysed and compared with results from *ab initio* calculations. The decision to study homoepitaxy of Al on Al(111) was taken with care. Indeed, for this system most complications related to epitaxial growth analysis are avoided: The Al(111) close packed surface is the thermodynamically most stable orientation and exhibits no reconstruction, and as for all homoepitaxial systems, alloying, strain and chemical effects do not play any role. The fifth chapter presents an analysis for the diffusion and nucleation of Al adatoms on the reconstructed Au(111) surface. For this system strain is expected to be negligible (0.75% lattice misfit), and no alloying occurs at low temperature. Thus, the main difference between the Al/Al(111) and the Al/Au(111) system is the presence of the reconstruction in the latter. This allows us to study the diffusion and nucleation on a non homogenous surface, and to compare the results with the measurements performed on the homogeneous Al(111) surface. Kinetic Monte-Carlo simulations were performed in order to rationalize the saturation island density behaviour in the low temperature regime. We briefly discuss at the end of this chapter the correlation between the diffusion barriers and the attempt frequencies for metal on fcc(111) metal surface systems. Our data indicate 220 K to be the upper limit before surface alloying sets in for the Al/Au(111) system. In chapter 6 we investigate the modifications of the Au(111) surface reconstruction produced by the alloying between the deposited aluminum and the Au(111) surface.

Chapter 7 contains the results of our analysis of Cu deposition on the Ni(100) surface. In this case the substrate surface exhibits no reconstruction, and no alloying is observed for temperatures below 450 K. For this system the strain, although small, plays a crucial role (+2.6% misfit). We focalise in this chapter on strain relief due to island shape modifications.

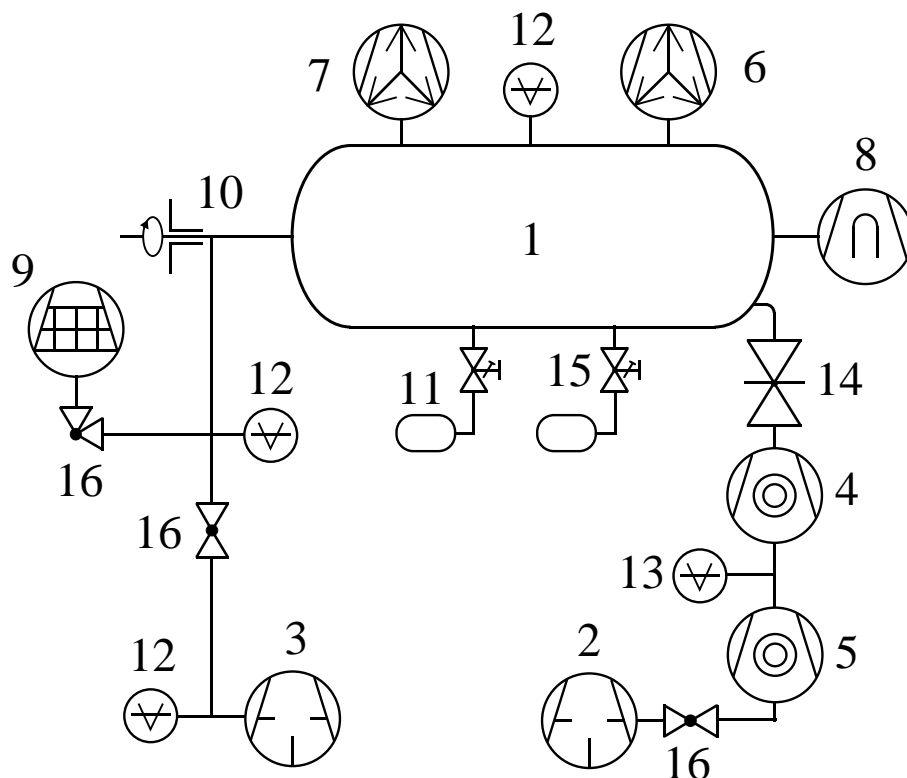
## Chapter 2

# Experimental

### 2.1 Setup of the experiment

The study of relevant processes involved in metal epitaxy requires a contamination free substrate. In order to obtain clean, well defined surfaces all experiments were performed under UHV conditions. The UHV chamber - stainless steel, copper flanged - is pumped by a combination of rotary, turbo molecular, ion and titanium sublimation pumps. A sketch of the pumping system setup and the chamber is shown in Fig. 2.1. After bakeout (160-180°C), a vacuum better then  $2 \times 10^{-10}$  mbar was obtained; the total pressure was measured by ionization gauges. During STM-measurements, the rotary and turbo molecular pumps are stopped, as the vibration and sound are highly obstructive, and the pumping is achieved with the ion and adsorption pumps only (see Fig. 2.1).

The main analysis tool used in the present thesis is a variable-temperature STM [20, 21]. The STM employed is of the « beetle » type [22]. Its geometry of three supporting piezo tubes fixed to an aluminum head with the central scanning piezo tube (the central piezo is laid out as a « single tube scanner » [23]) is appropriate for variable-temperature applications, as thermal contractions and dilatations of the support and scan piezos cancel each other to first approximation, leading to reduced thermal drift problems. Measurements are done by positioning the STM head on a circular triple helix Mo-ramp surrounding the sample. For the coarse approach of the tip, as



1	UHV chamber	9	N <sub>2</sub> cooled adsorption pump
2	Two stage rotary vane pump (16m <sup>3</sup> /h), duo 016 B, Balzers, Lichtenstein.	10	Differentially pumped rotary feedthrough
3	Rotary vane pump (16m <sup>3</sup> /h), Trivac Leybold, Germany.	11	Gas inlet system
4	Turbomolecular pump (350 l/s), 340 M Leybold, Germany.	12	Ionization gauge head (Bayard-Alpert), IE 414, Leybold, Germany
5	Turbomolecular pump (15 l/s), TPD 020 Balzers, Lichtenstein.	13	Pirani gauge head
6	Ion pump (200 l/s), PID 200N Meca2000, France	14	Bellows-sealed gate valve
7	Ion pump (240 l/s) VacIon Plus 300 StarCell, Varian, Italy	15	Leak valve
8	Titanium sublimation pump	16	Seal valve

**Fig. 2.1.** Sketch of the vacuum system

well as for lateral movement over the sample, an inertial drive is used, i.e. asymmetric sawtooth voltage pulses are applied to the external piezos, leading to alternate bending and sliding over the ramp [24]. Some of the principal advantages of this microscope type are :

- The design of the « beetle » STM is compact. Due to its « pocket size » and its rigid construction, it is rather insensitive to external vibrations.
- For operation, the STM is simply placed on the sample holder. No complicated and possibly fragile sample transfer mechanisms are necessary. As the sample remains mounted to the manipulator during all operations, the realization of a temperature control system for STM *in situ* studies is largely facilitated.

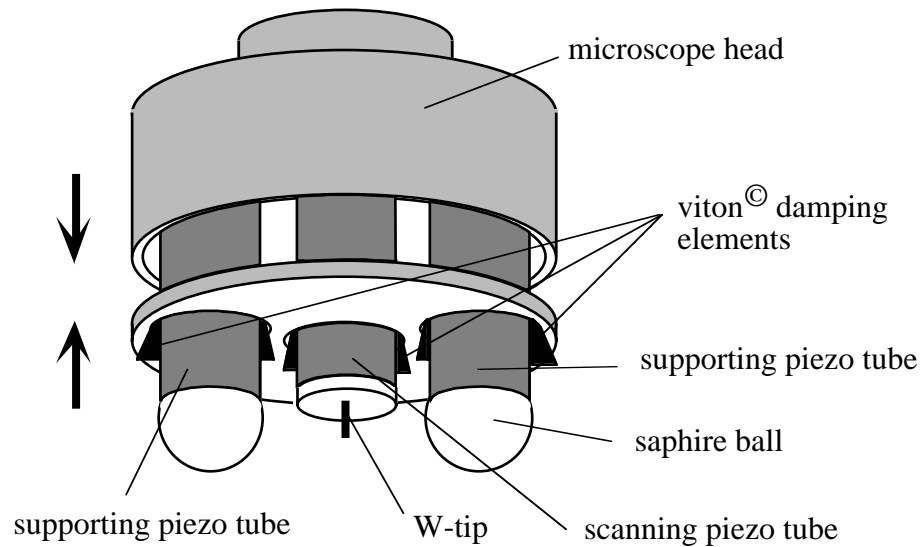


**Fig. 2.2.** The STM-Head with two of the outer piezos and the central single tube scanner. Small pieces of viton, clamped between the metal plate that can be screwed under the STM and the piezos tubes, efficiently damp vibrations of the piezo tubes. From [25].

Two different STM's were used in the course of this thesis. The change to a new design of microscope was motivated by an analysis of the vibrational properties of the beetle-type STM [25]. The vibrational modes with the lowest eigenfrequencies are those of a bending of the piezo tubes (see § 2.2). By increasing the diameter of the piezos from 3.2 mm to 6.4 mm, the lowest eigenfrequencies of the microscope could be tuned to approximately 5.5 kHz [26] (2 kHz with the original STM). A further improvement of the vibrational behavior was achieved by damping the

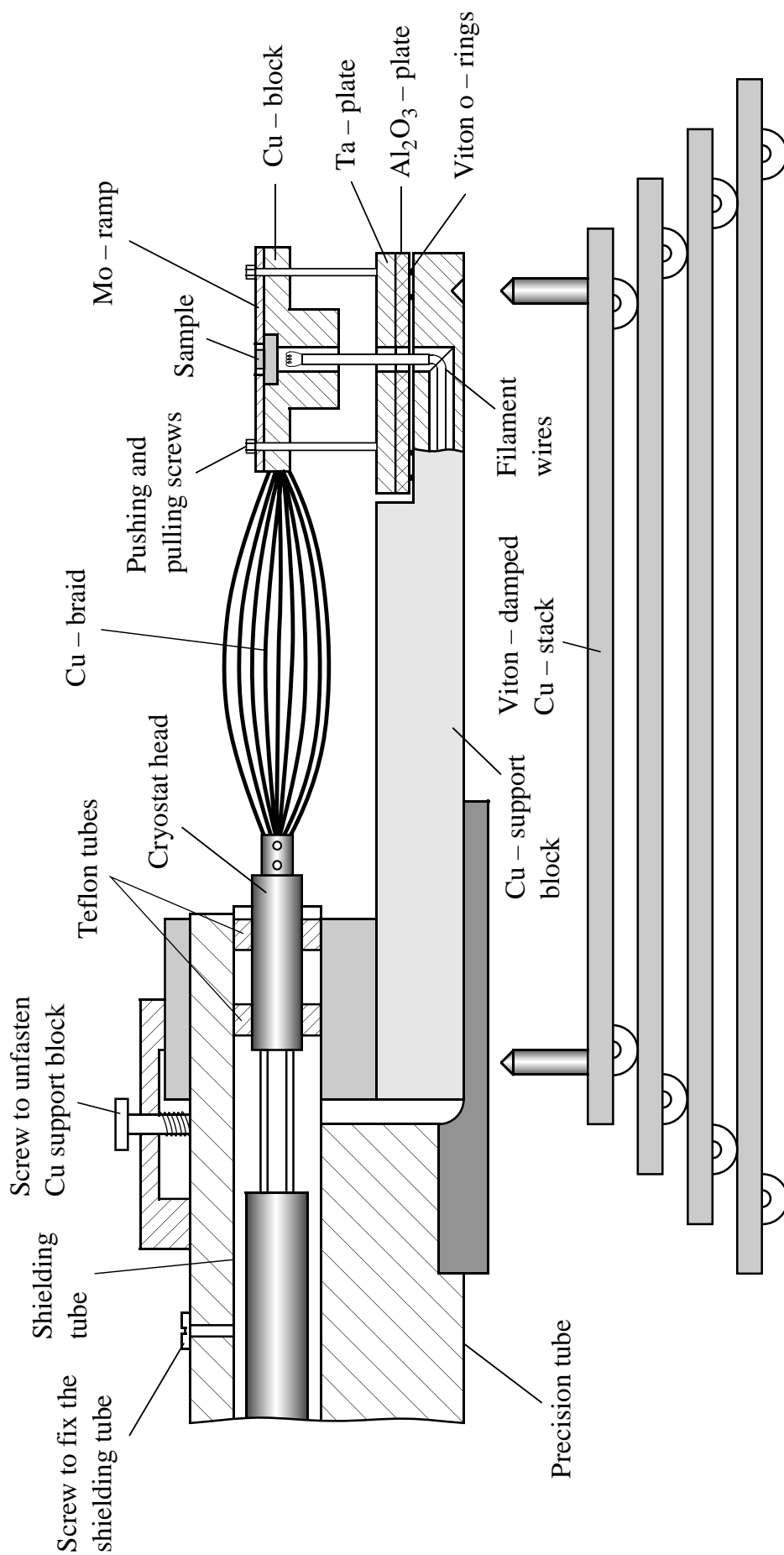


**Fig. 2.3.** Side view of the manipulator and the sample holder. In the STM mode the copper support block is uncoupled from the precision tube and rests on the viton - damped Cu - stack.

vibrations of the piezos tubes by small pieces of viton clamped between the tubes and a metal plate that can be screwed under the head of the microscope (Fig. 2.2).

Two different electronic feed-back controls and data acquisition systems were used for the experiments: i) a home-built electronics similar to the original Besocke beetle-type control unit [27]; ii) a commercial STM control unit developed by RHK Technology [28]. The second control system showed a much better signal to noise ratio than the first. Furthermore, it is equipped with a 16-bit A/D converter for data acquisition (the Besocke-type electronics allows only for data treatment with 8-bit precision). This allows for a markedly finer graduation of the absolute height information, with simultaneously a sufficiently large dynamic range to cope with typical experimental problems like inclined scanning planes or vertical drift. Various additional features such as tunneling spectroscopy, improved image treatment and data evaluation are implemented. In case of i) the problem of the smaller dynamic range is usually circumvented by applying a high pass filter with a cutoff frequency of 33 Hz to the data before representation and storage. The resulting image is a kind of differentiated signal and emphasizes the relative change in height of neighboring points. The images recorded in this differential mode appear as if the surface was illuminated from the left. In case of ii) the larger dynamic range allows the height variations to be recorded directly and imaged in a gray scale representation.

All images shown in this thesis were recorded in the constant current mode, where the distance between the sample and the tip of the STM is adjusted during scanning to keep the tunneling current constant. Even though this mode is often called « topographic », the STM does not image the geometric position of atoms or their nuclei, but reflects a convolution of electronic and structural properties of the surface.

In addition to the STM, the chamber is equipped with the following tools for sample preparation and surface analysis:

- An ion gun for sputtering (Ion gun: home built; power supply: PS-IQE 10/35, Specs, Germany)
- A Knudsen type evaporator for metals (WKC3, W.A. Technology Ltd., England)
- A backview LEED system (SPECTALEED, Omicron, Germany)
- An Auger electron spectrometer: Cylindrical sector analyzer (CSA 300) combined with an 5 kV electron gun (EFK 50) (Focus/Omicron, Germany)



Figure 2.3 shows a sketch of the manipulator and sample holder. One can distinguish three functional units: The actual sample holder comprising the circular ramp for tip approach and the *in situ* part of the temperature control system, the copper support block and damping stack, and finally the precision tube connected to a long travel manipulator including the cryostat. To ensure the compatibility of the sample holder with the different analysis instruments, and to optimize the performance of the STM, each unit has been modified several times during this thesis.

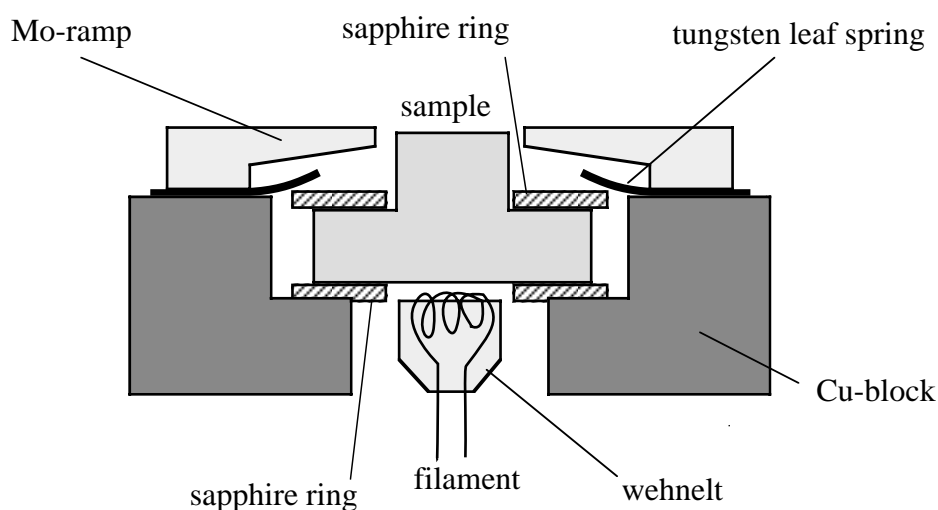


**Fig. 2.4.** Sketch of the sample fixation. The sample is clamped between two sapphire rings for electrical isolation. This design permits effective cooling of the sample via the Cu sample holder, and isolates the sample thermally during flash annealing.

The first unit includes the sample holder itself. The hat-shaped crystal is clamped at its brim to a copper block by means of a molybdenum ring, the latter providing the circular ramps for tip approach. The crystal is thermally coupled to the liquid-He flux cryostat via the copper block. The coupling is made by a copper braid to combine a maximum of thermal conductivity with a minimum of vibrational contact. The crystal is electrically isolated from both Mo-ring and Cu block by two sapphire washers. Sapphire combines a high thermal conductivity at low temperature (60 W/cmK @ 40 K) facilitating an effective cooling of the sample with a low conductivity at high temperature (0.4 W/cmK @ 300 K) permitting to heat only the sample during flash annealing. Due to the use of the fragile sapphire rings clamping of the crystal to the holder with screws is not practical. Instead, the upper ring is pressed by tungsten leaf springs; [20] which solves also the problem of sample loosening after repeated heating and cooling cycles, caused by the different thermal expansion coefficients of

the materials (see Fig. 2.4). Heating is achieved either by radiation or electron bombardment from a home made W-Re (4% Re,  $\varnothing = 0.2$  mm) filament mounted at the backside of the sample. The temperature is measured by a K-type (NiCr–Ni) thermocouple spot-welded to the sample, and a commercial temperature controller [29]. The copper block is mounted on a tantalum plate by pushing and pulling screws. This system is separated from the main copper support block by an  $\text{Al}_2\text{O}_3$  plate and small viton o-rings (see Fig. 2.3) and can thus be electrically isolated. This feature is important for future EELS measurements.

The second unit is composed by the main support block and the damping stack. During all operations except STM measurements, the main support block is attached to the precision tube. During STM measurements the support block with the sample unit is placed on a viton damped stack and is now decoupled from the rest of the manipulator to reduce the vibrational coupling (See § 2.2).

The last unit includes the remainder of the manipulator, i.e. the precision tube of the long travel translational manipulator (Omniax 600, Vacuum Generator, England. Travel length: 600 mm) combined with a differentially pumped rotary feedthrough, and the cryostat, placed inside the precision tube. In order to suppress possible vibrations at the head of the cryostat, the shielding tube is fixed at three different positions with screws. A short teflon tube surrounds the shielding tube at the position of fixing to avoid thermal losses. For the same reason the head of the cryostat is hold by three short teflon tubes (see Fig. 2.3).

Tests indicate that 800 K is the maximum possible sample temperature for STM measurements. Beyond this limit the piezolegs of the STM are excessively heated and there is a strong risk for the piezo material [30] to depolarize, causing the destruction of the STM. Due to thermal losses at the cryostat and the nonideal coupling between the copper braid and sample holder, the lowest temperature we accessed was 50 K. In this thesis we focalize on low temperatures, and only results obtained between 60 K and 350 K will be presented. STM measurements below room temperature were performed with full cooling power, and the desired temperature was maintained by radiative counter heating of the sample. The relative temperature stability is 0.1 K. The absolute accuracy of temperature measurements was estimated to 2.5 K above and 5 K below 200 K.

## 2.2 Vibration analysis

### 2.2.1 Introduction

STM measurements require a great mechanical stability ( $1 \times 10^{-12}$  m). In order to ensure such a stability, vibrational damping is essential. Building vibrations, noise from pumps or high frequencies due to voices or the like (100 Hz to kHz range) are sufficient to ruin the microscope resolution [31]. The sample is, during experiments, isolated from external vibrations by two damping stages. First a low-frequencies damping achieved by suspension of the whole UHV chamber with springs from the ceiling. This leads to an efficient vibration isolation against all relevant external vibrations (building, walking, ...). Higher frequencies (above 100 Hz) are damped by a stack of copper plates separated by viton on which the sample holder is positioned during the measurements (see Fig. 2.3).

Nevertheless, the system still has its eigenfrequencies, which may interfere with the STM imaging. A vibration analysis is therefore useful to try to minimize the effects of the eigenfrequencies, i.e. to optimize the resolution of the STM. Eigenfrequencies of a similar STM head have already been investigated [25]. In this thesis we focalize on the eigenfrequencies of the STM head when coupled to the sample holder and posed on the stack.

### 2.2.2 Calculation of eigenfrequencies

A beetle type STM head consists of a solid disk supported by three piezo tubes legs. Resonances involve a deformation (bending, stretching) of these piezo legs. Three intrinsic vibrational modes of the disk with respect to the ramp can be thought of an horizontal translation (H), vertical translation (V), and rotation (R) around the symmetry axis (see Fig. 2.5).

We calculate the resonance frequencies for a disk of mass  $M$  sitting on three tubes with mass  $m$  and spring constant  $K_{\perp}$  and  $K_{\parallel}$  for bending and stretching motion respectively. In this calculation, we assume that the legs are fixed to the ramp. For a tube with length  $L$ , inner diameter  $d$ , outer diameter  $D$  and elastic modulus  $E$ , the spring constants are [32, 33]:

$$K_{\perp} = \frac{3\pi}{64} E \frac{D^4 - d^4}{L^3} \quad \text{and} \quad K_{\parallel} = \frac{\pi}{4} E \frac{D^2 - d^2}{L}$$

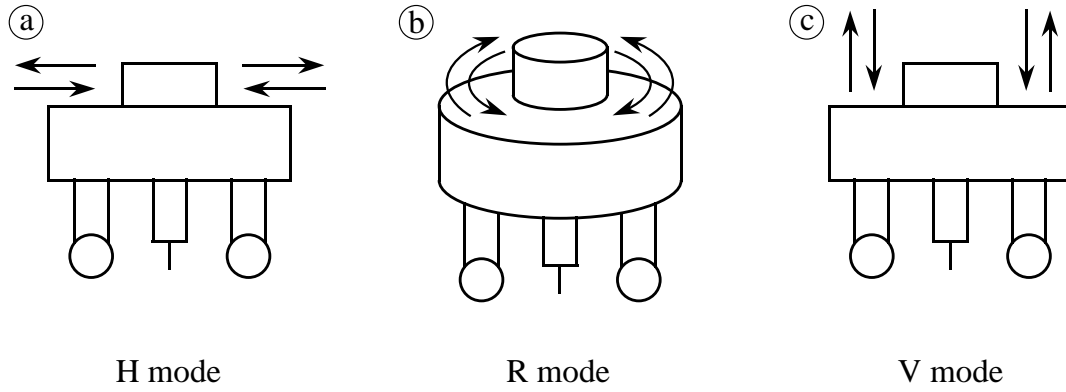


**Fig. 2.5.** The three intrinsic vibrational modes of the STM head. a) H mode b) R mode and c) V mode.

The horizontal translation mode frequency is given by  $f_H = \frac{1}{2\pi} \sqrt{\frac{3K_{\perp}}{M + 3m}}$  (2.1)

(the factor of three accounts for the number of legs)

The rotational motion frequency is given by  $f_R = \frac{1}{2\pi} \sqrt{\frac{6K_{\perp}}{M + 3m}} = \sqrt{2}f_H$  (2.2)

( $M$  and  $K_{\perp}$  have been replaced by the moment of inertia  $I$  of the STM, and the torsional spring constant  $K_{\perp}r^2$ ,  $r$  being the distance of the piezo to the center of the head of the STM).

The vertical translation frequency is given by  $f_V = \frac{1}{2\pi} \sqrt{\frac{3K_{\parallel}}{M + 3m}}$  (2.3)

Our STM is assembled from piezo tubes with  $L = 14$  mm,  $D = 6.3$  mm,  $d = 5.3$  mm and an elastic modulus  $E = 6.0 \times 10^{10}$  N/m<sup>2</sup>. The disk has a weight of 16.3 g and each piezo weighs 0.72 g. The resulting eigenfrequencies are  $f_H \cong 3.2$  kHz,  $f_R \cong 4.6$  kHz and  $f_V \cong 13$  kHz. These values are of course only an estimation of the real eigenfrequencies.

### 2.2.3 Experimental setup and results

We studied the response of our system (STM + sample holder) to a simulated noise source of tunable frequency. We applied a sine wave (2Vpp) to the +x electrode of the scan piezo. The in-phase piezoelectric voltage pickup from the +x electrode of a leg piezo (Fig. 2.6) (reflecting its bending) is monitored with a lock-in amplifier. Thus mode H is excited and monitored. During the measurements the STM head is posed on the Mo-ring. This technique has already been described by other groups (e.g. [33]).

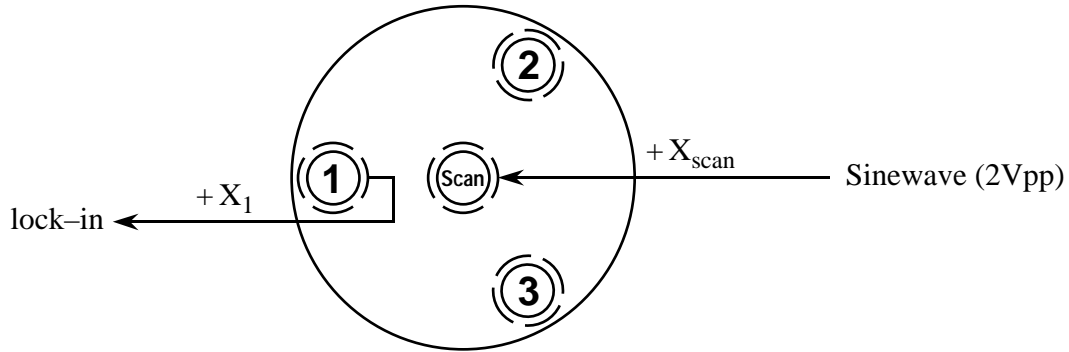


**Fig. 2.6.** Setup of the vibration analysis experiment. A sinewave is applied to the central piezo, and the signal is collected on the corresponding electrode of an external piezo. From [33].

Figure 2.7 shows a spectra obtained by this method. It covers the frequency region from 1 to 19 kHz. One observes large resonance peaks between 3.4 kHz and 19 kHz. The onset of a strong resonance peak at 3.4 kHz could be assigned to the intrinsic mode H vibration for which we calculated a resonance frequency of 3.2 kHz. The peak at 12.8 kHz may be the V mode excited by coupling.

Unexpectedly, additional resonances at lower frequency were found in the range 500 – 2200 Hz, as shown in Fig. 2.10. These resonances are, however, of smaller amplitude than those of Fig. 2.7 (compare the peak at  $\approx 2$  kHz, note that the scale in Fig. 2.7 is a factor 20 lower than in Fig. 2.10). Resonances in this frequency range could perturb the STM imaging process ( $\approx$  scanning rate) and must therefore be damped as efficiently as possible. This phenomena was already observed by Behler et al. [33]. They attributed this effect to the characteristics of the microscopic contacts between the sapphire balls and their support (Mo-ring). Due to the low frequency range where the resonances occur, they cannot be assigned to intrinsic resonances of the STM head or the support. They must be related to a rattling motion of the entire STM head with respect to the ramp. Such a motion is likely, as the STM head is only fixed to the surface of the ramp by its own weight. The properties of these contacts, such as adhesion and friction, change when the STM is moved to different locations. It is possible that small particles (dust, wear particles...) between the sapphire

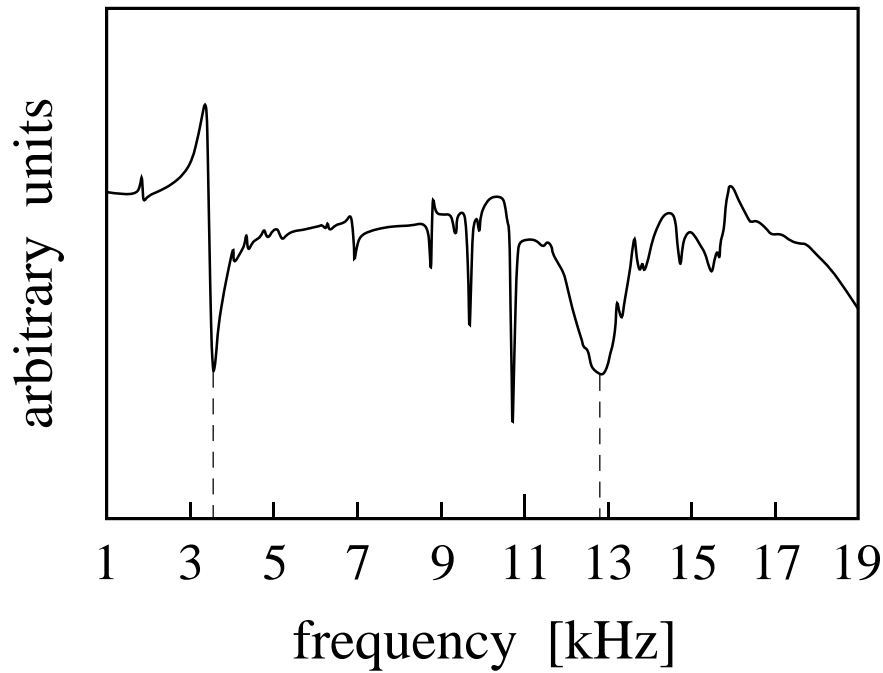


**Fig. 2.7.** Resonance behaviour of the STM head positioned on the sample holder. One could easily distinguish the H mode at 3.4 kHz and the probable V mode at 12.8 kHz.

balls and their support may also play a role. These rattling motions can involve three basic modes: horizontal translation, vertical translation and rotation around the symmetry axis. In this case, vertical motion also includes tilting the STM head back and forth around a horizontal axis.

In order to minimize effects of these resonances, we performed several tests with our STM head and sample holder. Figure 2.8 shows the STM head resonance behavior when its weight is changed (b). During these measurements the STM head was not placed on the sample holder, but on a stack formed by 3 stainless steel plates separated by viton rings. Generally we observed a shift in the position of the resonance peaks towards lower frequencies as expected. As an example, the peak at 1.32 kHz is shifted by 0.59 kHz to 0.73 kHz, when the STM head is loaded with 11.8 g (corresponding to 65% overload with respect to its original weight).

Adding load to the STM head leads to a better contact between the sapphire balls and their support, and should reduce the rattling motion. This behavior can easily be seen in Fig. 2.8, where the amplitude of every resonance peak is lowered by at least a factor two. The same experience was performed with the STM head placed on the sample holder, upon where similar results were obtained.

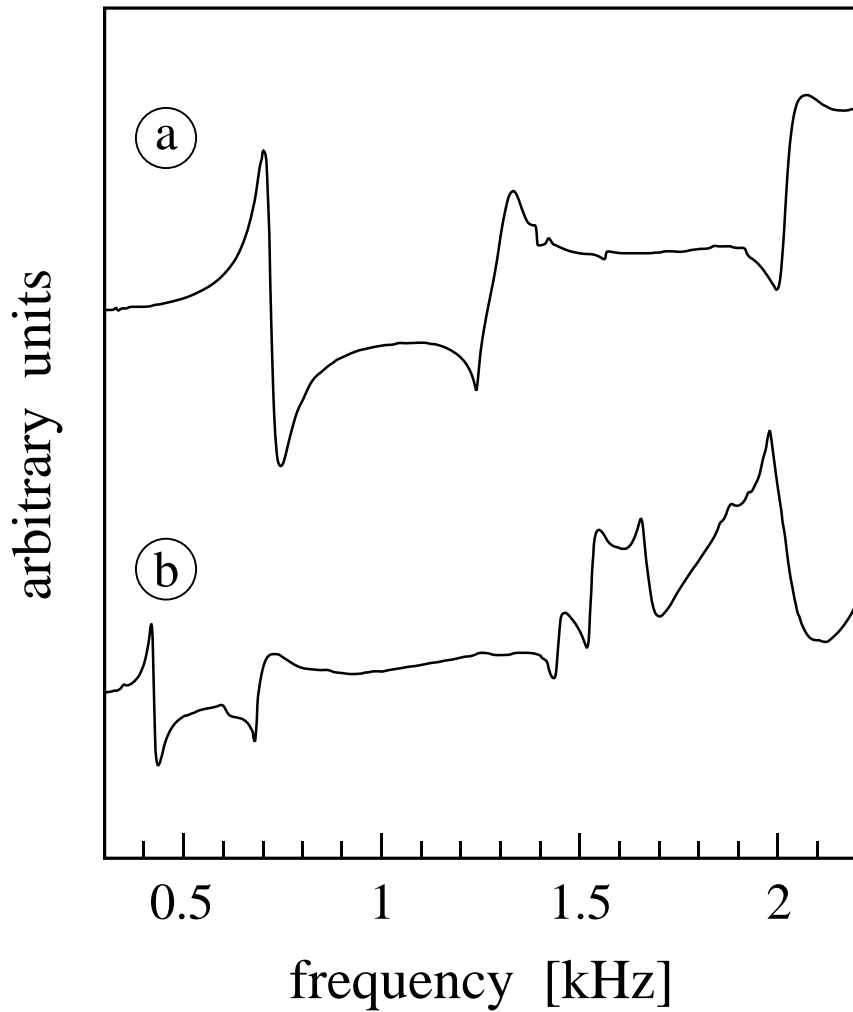


**Fig. 2.8.** Effect of the STM head weight on the vibration behaviour. a) with no extra load; b) with an extra load of 11.8 g. All peaks are shifted toward lower frequencies. The corresponding amplitudes are lowered by a factor  $\approx 2$ .

Figure 2.9 shows the STM head behavior when positioned on a stainless steel stack. Each spectrum corresponds to a different moment of inertia, i.e. size and weight of the last plate of the stack (as shown in Table 2.1). The estimated moment of inertia of the STM head and the actual sample holder are  $1 \times 10^{-6}$  [kgm<sup>2</sup>] and  $5.7 \times 10^{-3}$  [kgm<sup>2</sup>], respectively. It is obvious that the amplitudes of the resonance peaks are increasing with the plates' momentum. The best damping is thus achieved when the STM head and the supporting element (plate (a) in this case) have comparable momentum.

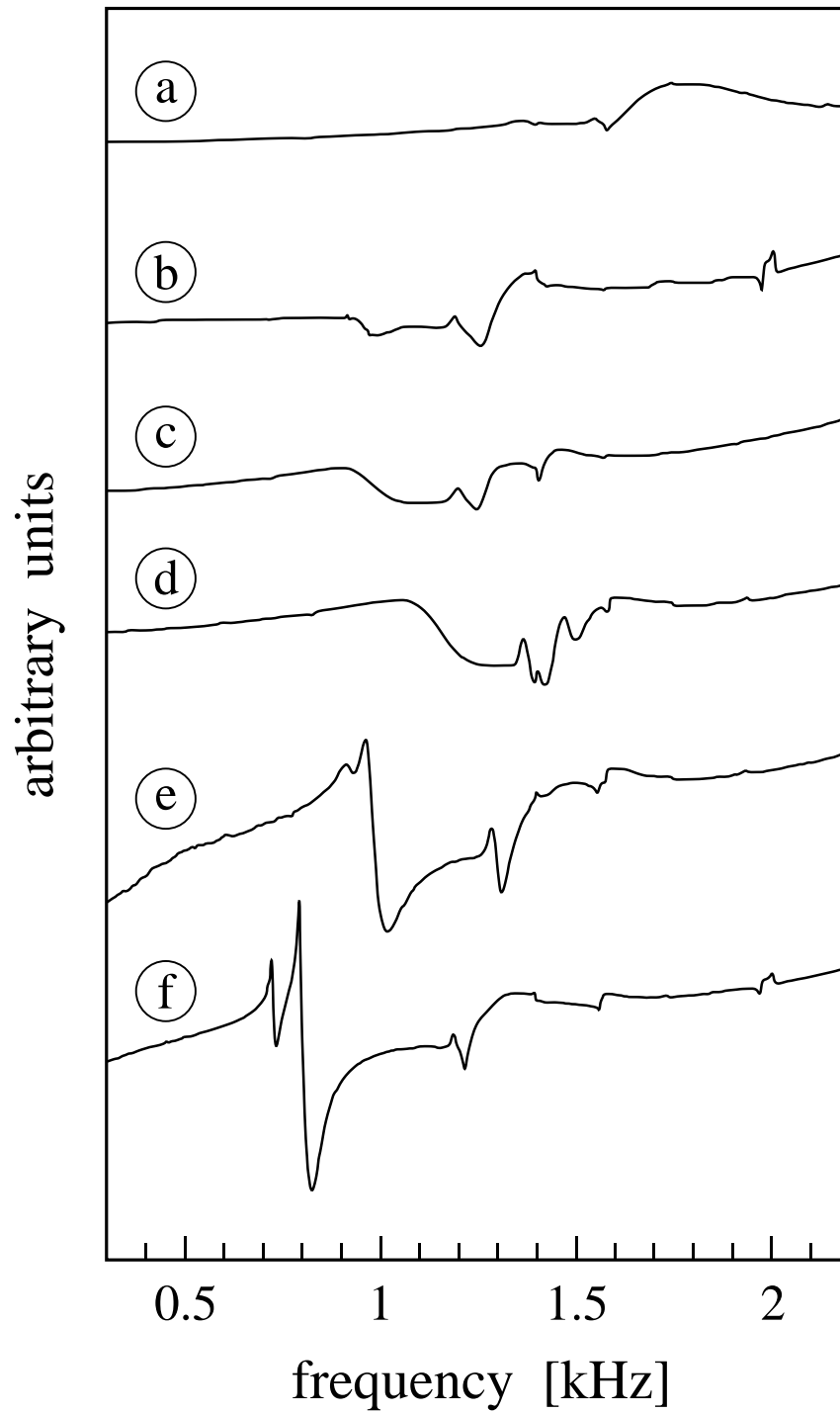


**Fig. 2.9.** STM head resonance behaviour when positioned on a viton damped stack. Each spectrum corresponds to a different moment of inertia of the last plate of the stack (see Table 2.1).



	Moment of inertia [kgm <sup>2</sup> ]
STM head	$\approx 1 \times 10^{-6}$
plate a	$1.27 \times 10^{-5}$
plate b	$3.50 \times 10^{-5}$
plate c	$1.39 \times 10^{-4}$
plate d	$1.42 \times 10^{-4}$
plate e	$4.45 \times 10^{-4}$
sample-holder	$\approx 5.7 \times 10^{-3}$
plate f	$3.63 \times 10^{-2}$

**Table 2.1.** Values of the moments of inertia for the plate used as last stage of the damping stack. The estimated moments of the STM head and the actual sample holder are  $I_{\text{STM}} \approx 1 \times 10^{-6}$  [kgm<sup>2</sup>] and  $I_{\text{s-h}} \approx 5.7 \times 10^{-3}$  [kgm<sup>2</sup>], respectively.

This observation led to a modification of our sample holder. In order to lower its momentum (i.e. to diminish the vibrations), we placed between the Al<sub>2</sub>O<sub>3</sub> plate and Cu support block four viton rings (see Fig. 2.3) ( $\varnothing = 5$  mm and  $d = 1.5$  mm). The introduction of this additional damping stage had a substantial effect on the amplitudes of the resonance peaks. All of them were diminished by factors between four and ten, and no significant frequency shift was observed (see Fig. 2.10).

The better understanding resulting from these tests, have been used to improve in a significant manner the vibrational stability of the instrumental set-up. The calculated eigenfrequencies for the horizontal and vertical modes are in good agreement

	H mode	V mode	R mode
Calculated resonances [kHz]	3.2	13	4.6
Measured resonances [kHz]	3.4	$\approx 12.8$	—

**Table 2.2.** Calculated and measured values of the eigenfrequencies of the STM head coupled to the sample holder.

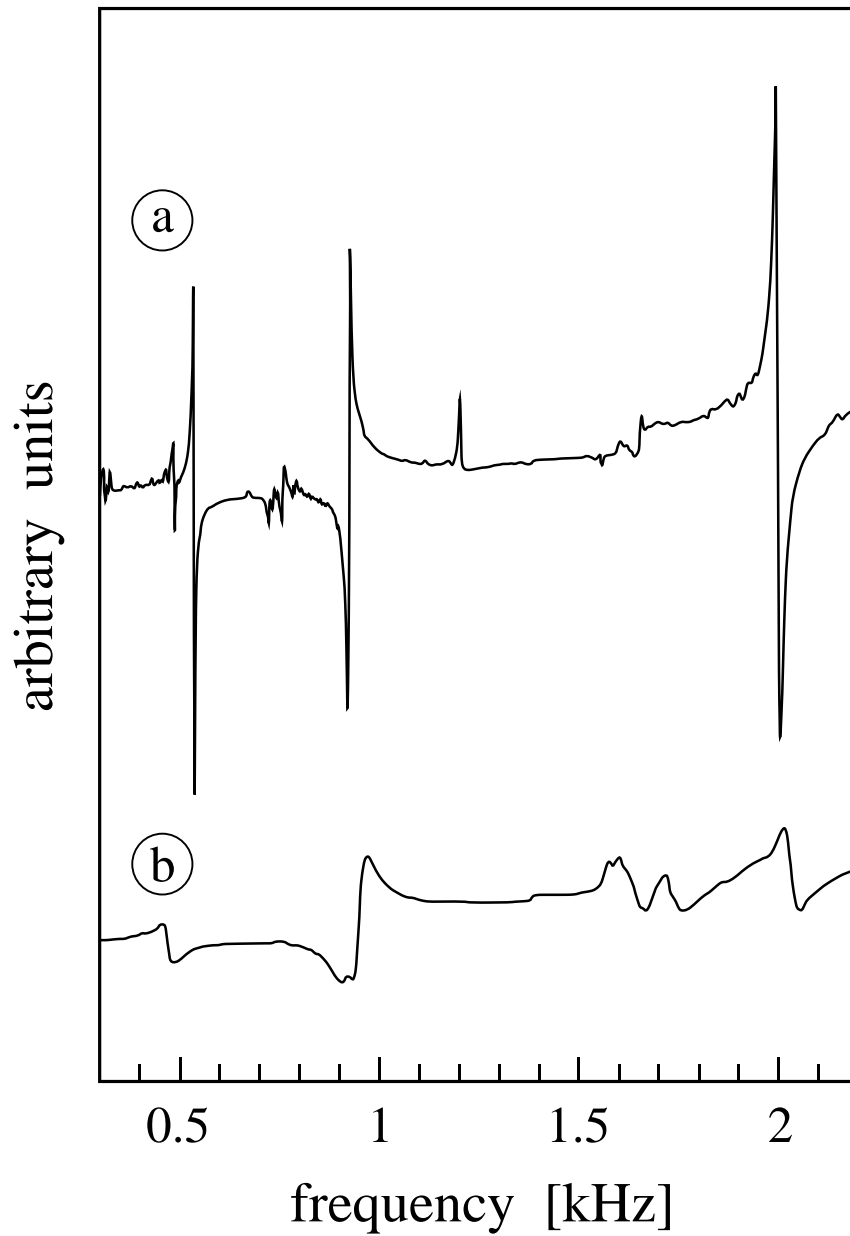


**Fig. 2.10.** The introduction of the third damping stage modified significantly the vibrational behaviour of the STM head. a) before modification; b) after placing four viton rings between the  $\text{Al}_2\text{O}_3$  plate and the Cu support block (see Fig. 2.3).

with the experimental values (see Table 2.2). The simple experimental set-up used for these measurements does not allow us to excite the rotational mode. For this reason only the calculated value appears in Table 2.2. Further improvement of vibrational

stability would require fundamental modifications in the geometry of the sample holder. Also the construction of a new STM with enhanced weight might increase the stability, but on the other hand, it will lower the eigenfrequencies of the STM head.

## 2.3 Sample preparation

All samples used were hat-shaped and commercially purchased, the precision of the cut was guaranteed by the manufacturer to be  $0.16\text{--}0.25^\circ$ . Different cleaning procedures were adopted for each crystal:

- Al(111)
  - a) Argon sputtering at room temperature.
  - b) Several flash anneals (min. 5 times). Finally the sample was heated to 800 K for a short time (2–5 sec) and slowly cooled back to 300 K.

Sputtering was done using Ar ions with a kinetic energy of about 0.5 keV. An Ar pressure of  $(1\text{--}3)\times 10^{-6}$  mbar was used to obtain a total sputter current of  $3\text{ }\mu\text{A}/\text{cm}^2$  on the sample and the Mo-ring. Each cycle lasted (20–25) min.
- Au(111)
  - a) Argon sputtering at room temperature
  - b) Flash anneals. The sample was heated to 1000 K for (15–30) sec.

Sputtering was done using Ar ions with a kinetic energy of about 0.8 keV. An Ar pressure of  $(1\text{--}4)\times 10^{-6}$  mbar was used to obtain a total sputter current of  $(0.6\text{--}1)\text{ }\mu\text{A}/\text{cm}^2$  on the sample. Each cycle lasted about 15 min.
- Ni(100)
  - a) Argon sputtering at elevated sample temperature  $T_s = 550\text{ K}$ .
  - b) Flash anneals. The sample was heated to 1100–1200 K for about half a minute. However, at the beginning of the cleaning process occasional flashes to temperatures as high as 1400 K have been proven to accelerate sample preparation [34].
  - c) Argon sputtering at room temperature.
  - d) Flash annealing.

Sputtering was done using Ar ions with a kinetic energy of about 2.3 keV. An Ar pressure of  $(1\text{--}4)\times 10^{-6}$  mbar was used to obtain a sputter current of  $(0.6\text{--}1)\text{ }\mu\text{A}/\text{cm}^2$  on the sample. Each cycle lasted typically 15–20 min. The last sputtering cycle before copper deposition was always a non-heated one to avoid

contamination of the surface by impurities diffusing from the bulk, above all carbon [35].

All these procedures were carried out several times before each measurement. These treatments results in a clean surface. Impurities (oxygen, carbon,...) were below the detection limit of Auger electron spectroscopy. The corresponding LEED measurements exhibited accordingly low background patterns characteristic for the respective clean metal surfaces.

- Copper (Balzers, 99.99% pure) was deposited by thermal evaporation at growth rates between  $5 \times 10^{-5}$  and  $1 \times 10^{-2}$  ML/s, corresponding to temperatures of the Knudsen cell between 840 and 1150°C.

- Aluminum (Goodfellows 99.999% pure) was deposited by thermal evaporation at a growth rate of  $6.5 \times 10^{-4}$  ML/s, corresponding to a temperature of the Knudsen cell of 950°C. AES spectras have been taken before measurements to ensure that no contamination or oxidation occurred during evaporation.

The growth rates were calibrated from STM images at monolayer coverage, where borderline effects and the resulting inaccuracies are minimal.



## Chapter 3

# Nucleation and Growth

This chapter briefly describes the background of growth phenomena at surfaces and provides the necessary basis for the analysis of the experimental results. After the discussion of two different approaches generally used for the description of epitaxially grown films, the basics of the mean-field nucleation theory are presented. The latter comprises the theoretical results indispensable for the derivation of microscopic parameters of major interest in thin film growth.

### 3.1 Growth scenarios

#### 3.1.1 Thermodynamics growth

The thermodynamic classification of growth modes was first addressed by Bauer [36]. It divides the film morphology into three classes determined by the balance of interfacial and surface free energies. However, it should be noted that growth is by definition impossible at equilibrium conditions. As required by the principle of detailed balance, all atomic processes then proceed in two opposite directions with equal rates. Hence there is no net growth and crystal growth must clearly be treated as a non-equilibrium kinetic phenomenon [37]. In terms of thermodynamics, therefore, growth can only be considered very close to equilibrium and must be treated as a quasi-equilibrium process. Bauer's criterion, the so-called wetting condition, is given by: [36, 38, 39]

$$\Delta\gamma = \gamma_f + \gamma_i - \gamma_s \quad (3.1)$$

$\gamma_f$ ,  $\gamma_i$ ,  $\gamma_s$  being the surfaces free energies of the film surface, substrate and film-substrate interface, respectively. Equation 3.1 allows a formal distinction of the three growth modes depending on the sign of  $\Delta\gamma$ . If  $\Delta\gamma \leq 0$  the energy balance will favor "wetting" of the surface by the deposited film, and layer-by-layer growth (Frank–van der Merwe growth) is expected. For  $\Delta\gamma > 0$  the wetting condition is no longer fulfilled and 3D islands growth (Volmer–Weber growth) can be expected. There is an interesting intermediate case, named Stranski–Krastranov growth, where a

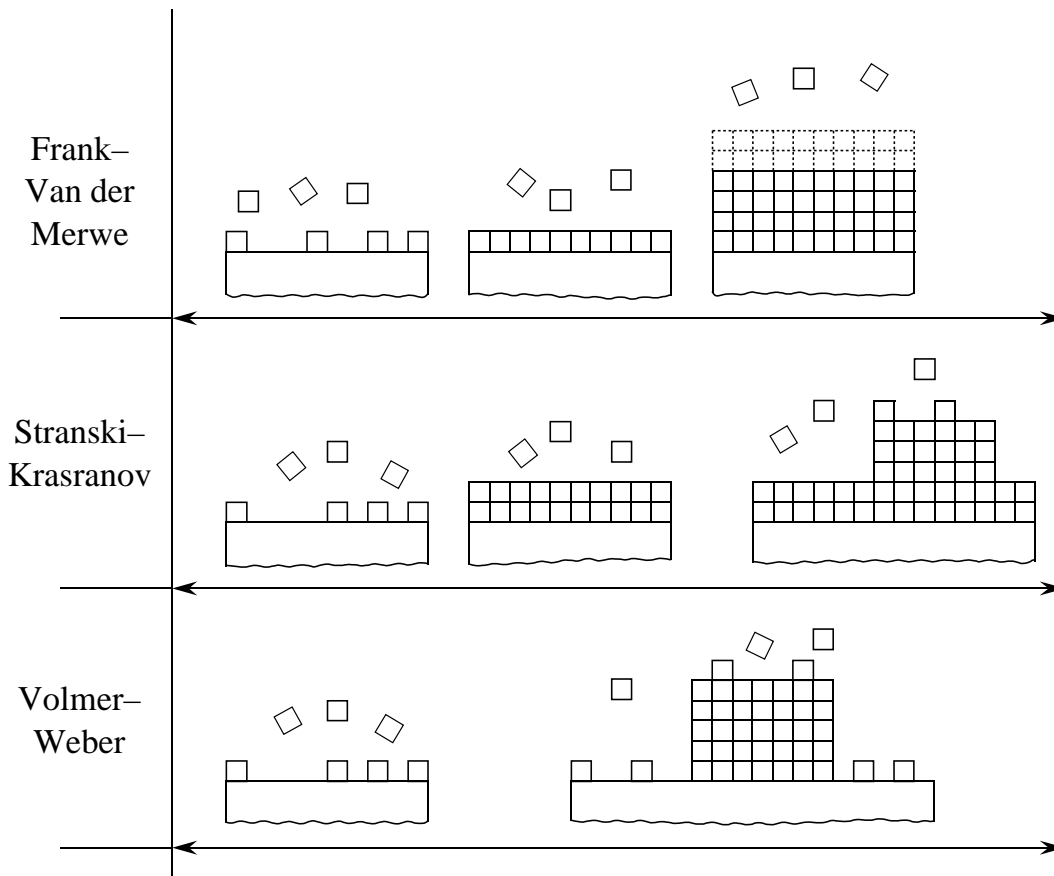


**Fig. 3.1.** Schematic representation of the three thermodynamic growth modes. a) two-dimensional (layer-by-layer) growth, b) three-dimensional (3D) growth, c) the hybrid case of three-dimensional "islanding" after layer-by-layer growth of one or several monolayers (from [40]).

transition from 2D to 3D growth occurs at a critical film thickness. While layer-by-layer growth is (thermodynamically) always expected for homoepitaxial systems (see chapter 4) the existence of a lattice mismatch between substrate and adlayer (see e.g. chapter 7) in heteroepitaxy influences the energy balance in Equation 3.1. Misfit strain energy contributions can modify  $\gamma_i$  with increasing film thickness, so that a change in the growth mode from layer-by-layer to 3D growth occur.

From the thermodynamic picture described above there remains a lack of microscopic understanding of the processes contributing to thin film growth. The assignment of macroscopic properties like surface free energies to structures that are at the atomic or nanoscale, e.g. small 2D cluster consisting of just few atoms, is not obvious [39, 41]. In addition, the experimental conditions during deposition by MBE lead generally to a supersaturation which is by orders of magnitude higher than the corresponding equilibrium pressure. Hence it is nearly impossible to give reliable predictions of the growth mode only by means of thermodynamic arguments. If the studied system is far away from equilibrium, the kinetics of the atomistic processes that occur during the film growth dominate the thermodynamics. Nevertheless the knowledge of the thermodynamic properties is important as they can be regarded as the driving force for kinetic processes.

### 3.1.2 Kinetics - atomic processes

In the kinetic picture, based on atomistic models, the growth mode is a complex balance of many competing processes, as sketched schematically in Fig. 3.2. The film morphology, as the outcome of this competition, is strongly influenced by the experimental conditions, i.e. the surface temperature and symmetry, the flux of adatoms impinging on the surface (deposition rate) and the choice of the material. Each of the atomic processes is characterized by an activation energy and a prefactor. At a given temperature  $T_s$  and deposition rate  $R$  certain processes might be kinetically inhibited, whereas others are rate determining. Arrhenius-type exponential laws describe mathematically these activated processes. In the following, surface diffusion and cluster aggregation which are at the origin of film growth, are briefly described:

- Surface diffusion.

Individual adatoms are located on the surface at a minimum energy adsorption site. In the case of metal on metal growth these sites correspond generally to the continuation of the bulk stacking sequence (except for reconstructed surfaces) such as a fourfold



hollow on a quadratic fcc(100) or a threefold hollow on a hexagonal fcc(111) surfaces. Adatoms may undergo transitions between two adjacent adsorption sites if the energy provided by thermal fluctuations of the lattice is large enough, i.e. if the temperature is sufficiently high. Thus depending on the substrate temperature, the adatoms migrate along the surface by overcoming the activation barrier  $E_m$  at the saddle point between neighboring sites. The hopping image for the transition is only valid for  $kT_s \ll E_m$ , which means that the residence time spent at the adsorption site is long in comparison with the time spent in the transition state. Between jumps, the adatoms therefore loses all memory of its original direction, and thus a random migration evolves. For  $kT_s \gg E_m$  the hopping image is no longer valid as no energetic barrier hinders the lateral displacements of adatoms.

The classic Einstein relation  $\langle \Delta x^2 \rangle = 2Dt$  describes well the statistics of the motion of single metal atoms on metal substrates [42]. The mean square displacement

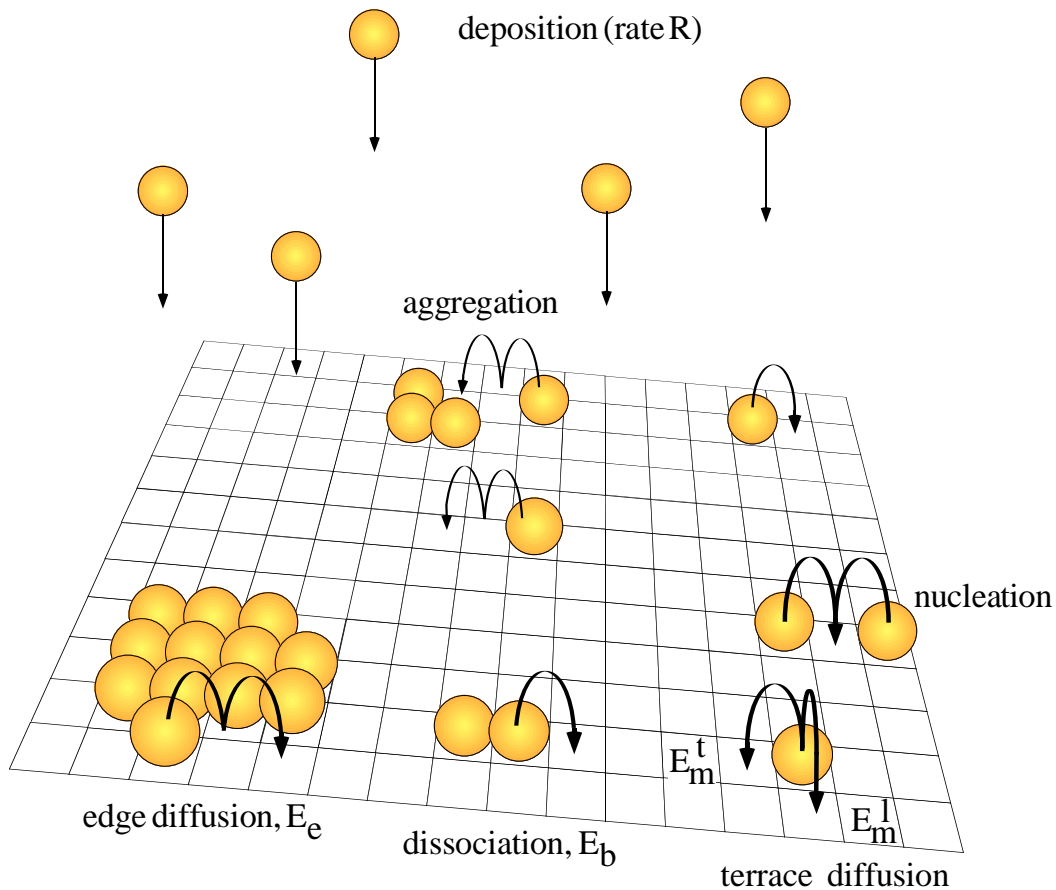


**Fig. 3.2.** Important atomic processes in the kinetics of 2-D film growth

$\langle \Delta x^2 \rangle$  along one coordinate is proportional to the diffusion time interval  $t$  and the diffusivity  $D$ . The connection with the energetic corrugation of the substrate is given by the Arrhenius behaviour  $D = D_0 \exp\{-E_m/kT_s\}$  where  $D_0$  is the preexponential factor,  $E_m$  denotes the activation energy for the adatoms terrace migration,  $k$  is the Boltzmann constant, and the pre-exponential factor  $\nu_0$  is the attempt frequency. Under the assumption of uncorrelated hops and negligible entropy of activation, the following relation is valid:  $D_0 = \nu_0 l^2 / 2d$ , where  $l$  is the distance between two adsorption sites (jump length),  $d$  is the dimensionality of diffusion and  $\nu_0$  is the attempt frequency.  $\nu_0$  can be interpreted as the number of attempts per unit time that the system tries to overcome the barrier  $E_m$ . The order of magnitude of  $\nu_0$  is given by the universal factor  $kT_s/h$ . Thus, the attempt frequency  $\nu_0$  corresponds to the typical frequency of lattice vibrations ( $\approx 10^{12} - 10^{13}$  Hz) and its temperature dependence is usually negligible with respect to the Boltzmann-factor.

#### • Cluster aggregation

Adatoms supplied from a 3D gas phase above the substrate diffuse on the surface so that initially a 2D gas phase is generated by the deposition flux. When the 2D gas phase reaches a certain super-saturation, nucleation of 2D clusters can set in provided the substrate temperature is low enough to avoid step-flow growth. The size of the 2D cluster depends on both the substrate temperature and the lateral binding energies of the adatoms, i.e. the adatom-adatom interaction energy, and can be as low as one atom. The critical cluster size " $i$ " is thereby defined as the largest unstable cluster size, i.e. only clusters with sizes  $j > i$  have a higher probability to grow than to decay [43]. A cluster having the critical size (= critical nucleus) becomes a stable cluster upon incorporation of one additional adatom. In the case where surface diffusion is inhibited, the critical cluster size is 0.

The image in Fig. 3.3. illustrates how the different cluster populations which are present on the surface can interact. Nucleation of critical, and growth of stable clusters are competing processes since both reduce the monomer density  $n_1$ . With increasing deposition time adatoms are predominantly captured by stable clusters which cover finally the whole substrate. Nucleation theory predicts the saturation island density  $n_x(R, T_s)$  as a function of the external growth parameters [43]. Comparison with experiments requires the knowledge of the critical cluster size  $i$ , its binding energy  $E_i$ , the adatom diffusivity  $D$  (assuming immobile clusters), and the time constant of evaporation  $\tau_a$ . The function  $n_x(R, T_s)$  depends strongly on the critical cluster size  $i$  since the probability to produce statistically a certain cluster type changes dramatically

with the number of atoms involved. With increasing temperature  $T_s$  the critical size  $i$  increases due to thermal dissociation of clusters, explaining the  $n_x(R, T_s)$  dependence on the cluster binding energy  $E_i$ .

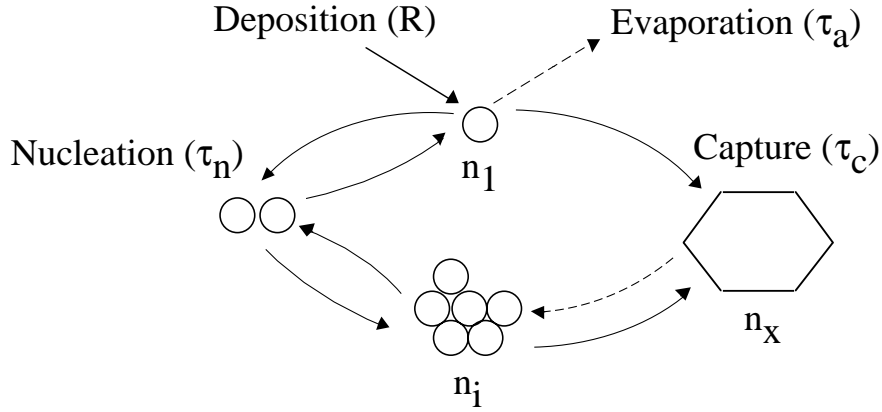


**Fig. 3.3.** Schematic illustration of the interaction between different cluster populations  $n_j$  in the early stages of film growth. The adatom concentration  $n_1$  determines the density of critical clusters ( $n_i$ ) and of stable nuclei ( $n_x$ ). The decrease of  $n_1$  depends on the time constants for nucleation ( $\tau_n$ ), evaporation ( $\tau_a$ ) and the capture rate ( $\tau_c$ ) of stable nuclei. This loss is compensated by the deposition flux  $R$ . The two dotted lines indicate the processes which are less important at low temperatures, i.e. the desorption of adatoms and the decay of stable clusters. (From [43])

## 3.2 Basics of mean-field nucleation theory

The mean-field theory (for a review see [43]) for nucleation and growth, is based on the resolution of the differential rate equations accounting for the underlying atomic processes described above. One result of this theory, proven by experiment [24], is the scaling between the density of stable islands  $n_x$  in the saturation island density regime, the deposition flux  $R$  and the surface diffusion constant  $D$ :

$$n_x \propto \left(\frac{D}{R}\right)^{-\chi} \quad (3.2)$$

$R$  is one of the external parameters; the variation of the diffusion constant  $D$  can be realized by changing the substrate temperature  $T_s$ :  $D = (v_0/2d)\exp(-E_m/(kT_s))$ .

In the expression 3.2, the scaling exponent  $\chi$  depends on the desorption rate, the dimensionality of the deposit, the type of diffusion (isotropic, anisotropic) and the size of the critical nucleus (see § 3.1.2). In the case of copper on Ni(100) the film grows mainly in the layer-by-layer mode<sup>1</sup> (see chapter 7). For Al/Al(111) and Al/Au(111) two-dimensional growth is also observed for coverages below  $\approx 0.3$  ML<sup>2</sup> (see chapters 4 to 6), hence for all systems studied in this thesis the dimensionality of the deposit is 2. Desorption can be neglected for temperatures below 400 K since at this temperature the nominal vapour pressure corresponds to  $10^{-35}$  mbar [45]. Accordingly, we present the results of the rate equation analysis and the mean-field nucleation theory for 2D growth and complete condensation (no re-evaporation). The normally given version of the main result of the nucleation theory is (see e.g. [46]):

$$n_x \cong \eta(\theta, i) \left(\frac{D}{R}\right)^{-\chi} \exp\left(\frac{E_i}{(i+2)kT_s}\right) \quad (3.3)$$

$$\text{where}^3 \ D = \frac{v_0}{4} \exp(-E_m/(kT_s)) \quad (3.4)$$

Here,  $i$  and  $E_i$  denote the number of atoms in the critical cluster (see § 3.1.2) and its total binding energy respectively, and  $\chi = i/(i+2)$ .  $\eta(\theta, i)$  is a function of the coverage  $\theta$ . Numerical values for  $\eta(\theta, i)$  can be found in [43], Fig. 6(c). In the saturation regime,  $\eta(\theta, i)$  is almost constant ( $\approx 0.25$  in our case). Hence, in this regime minor coverage fluctuations will have no effect on island densities and one can safely assume the temperature  $T_s$  and the flux  $R$  to be the only relevant external parameters.

<sup>1</sup> The low step-edge barrier characteristic for most of fcc(100) surfaces leads usually to layer-by-layer growth. For these surfaces the intralayer mass transport is sufficiently fast to allow atoms to leave the tops of growing two-dimensional islands as soon as they arrive. The growing ad-layer will be complete before second-layer nucleation sets in and thus layer-by-layer growth results.

<sup>2</sup> A fcc(111) surface has a rather high step-edge barrier compared to its diffusion barrier. Hence growth on fcc(111) surfaces is in most cases 3-D [25, 44]. However, in the saturation regime, the fraction of incoming atoms landing on an existing island is negligible and thus mean-field theory for 2-D growth applies.

<sup>3</sup> Here  $D$  is expressed in lattice units per second.  $D$  can also be expressed in cm<sup>2</sup>/s as in § 3.1.2.

Equation 3.3 predicts an Arrhenius behavior of the saturation island density, which can be used to determine the activation energy of terrace diffusion  $E_m$ . Two comments have to be added to this result.

1) With the size of the critical cluster  $i$  and the binding energy  $E_i$ , there are other free parameters in the theory. For an unequivocal determination of  $E_m$  one has thus to work in the low-temperature range where the dimer is stable<sup>4</sup> and thus  $i = 1$  and  $E_i = 0$ . There are three ways to determine up to which temperature the dimer is stable. Firstly, direct inspection of the sizes of stable islands in the nucleation regime for a given temperature [47]. Secondly, deposition at a temperature where dimers are surely stable and a subsequent annealing experiment. At a certain temperature, the island density will start to decrease and the mean island size will increase due to the onset of dimer and trimer decay (Ostwald ripening). Thirdly, examination of the dependence of the saturation island density on deposition flux as predicted by Equation 3.3. The last method, however, can not be applied if we want to put nucleation theory itself on the test.

2) For the integration of the rate equations, steady state conditions are assumed. This assumption holds only for  $D/R > 10^5$ . If the diffusion of adatoms is too slow, a large supersaturation of adatoms is formed during the deposition, and a part of them is still left after stopping the flux. The rate equations then have to be integrated under different starting conditions. This effect is called "post-nucleation" (see e.g. [48]). It decreases the island densities found in the experiment below the predictions of Equation 2.5. In chapter 6 this effect is observed for the Cu/Ni(100) system at low temperature (for  $T_s < 170$  K, the  $D/R$  ratio is approximately  $10^2$ ).

---

<sup>4</sup> There is no intrinsic difference in the physics of nucleation theory if the dimer is not stable. At a given temperature and for a given system, there is always a "critical" cluster which itself is not stable but will become stable upon incorporation of another atom. "Stable" refers to the time scale of the deposition. There is always a certain decay rate for clusters of any size. But if the impinging flux of diffusing atoms to the cluster is much higher than the rate of dissociation of atoms from the cluster, we can regard the cluster as stable.

## Chapter 4

# Nucleation and self diffusion of Al on Al(111)

### 4.1 Introduction

Aluminum is the most widely used interconnect material in semiconductor devices [49]. Reduced dimensions in chip design imply that the quality of interconnects and thus the control of the Al deposition become increasingly important. The understanding and the control of the microscopic processes which take place in the epitaxy are thus of fundamental importance. The close packed (111) surface of aluminum is the thermodynamically most stable surface and exhibits no reconstruction, and of course, neither chemical nor strain effects are expected to play a role during homoepitaxy. For these reasons Al/Al(111) can be considered as "reference system" for diffusion and growth of aluminum.

Furthermore aluminum is a prototype of a simple s-p metal (due to the lack of d electrons). For this reason it can be modeled as a quasi free electron metal. In contrast to d metals modelling from first principle calculations is thus feasible. *Ab initio* calculations have been performed by Stumpf and Scheffler [50] in order to extract the microscopic parameters for the diffusion and the binding energy of an Al adatom on the Al(111) surface. They also investigated the growth behaviour and the island shapes as a function of temperature of the Al/Al(111) system.

Up to now only one experimental study on Al/Al(111) homoepitaxy can be found in the literature. Homoepitaxy of Al on Al(111) has previously been studied by

Hinch et al [51]. Using HAS to study the surface topography changes induced by chemical vapor deposition (CVD), they concluded that the growth at temperatures above 350 K proceeds by a step flow mechanism. In addition, few investigations on the growth of aluminum thin films on close packed metal surfaces [52, 53], or on the growth of metals on the Al(111) surface [54, 55] were reported. All these studies were carried out using indirect methods (XPS, UPS, ARUPS, AES, ...) or reciprocal space methods (LEED, SPA-LEED, ...) and they concentrate on the growth mode and electronic structure of the thin films deposited. E.g. for the Al/Ag(111) system, alloy formation and layer by layer growth is expected at room temperature [52, 53]. For the Cu/Al(111) system quasi layer by layer growth occurs already at 120 K [54]. So far quantitative experimental data characterizing the self-diffusion and nucleation of aluminum on Al(111) are still missing.

In this chapter we present the first STM study of the nucleation and growth of Al on Al(111) as a function of temperature. Section 4.2 includes the extracted values from the island density for the diffusion barrier and attempt frequency and contains a discussion of the islands shapes. A comparison with predicted island shapes and calculated values for the diffusion barrier of an Al adatom are presented in section 4.3.

## 4.2 STM observations and analysis

### 4.2.1 Nucleation and diffusion

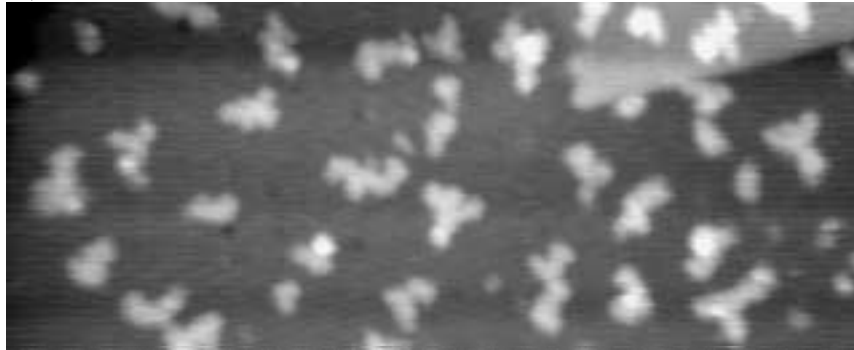
The first gross feature of the homoepitaxial growth of aluminum is that no islands are observed on the Al(111) surface for room temperature growth, even on rather large terraces. This is a clear indication for a very low barrier for diffusing adatoms leading to a step flow growth mode at room temperature. We thus investigated the Al nucleation behaviour for temperatures between 60 K and 200 K. Above  $\approx 200$  K, hardly any islands are observed on terraces, and of course no island density could be extracted with reasonable statistics.

Figure 4.1 shows a series of STM images characterizing the nucleation behaviour of 0.15 ML of Al on Al(111) as a function of the substrate temperature during deposition. When concentrating on the island density one observes, as expected, a decrease of the island density with increasing deposition temperature. The island density decrease appears continuously indicating that in the studied temperature

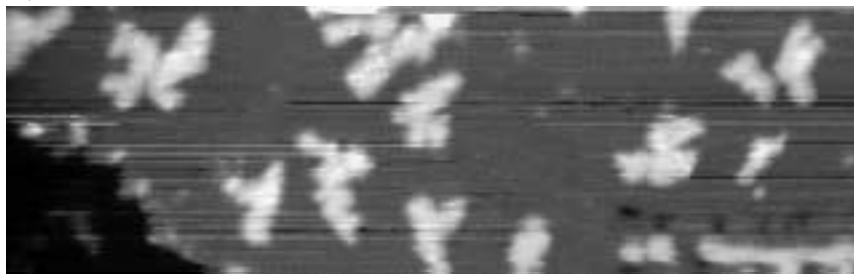
a) 60 K



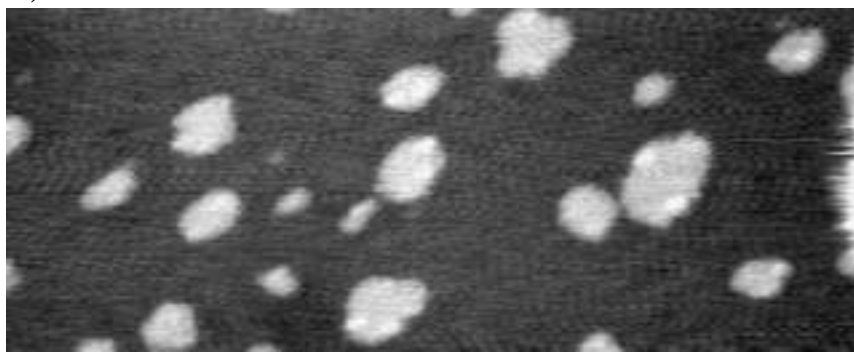
b) 80 K



c) 100 K



d) 180 K



A horizontal scale bar with vertical end caps. Above the bar, the text "200 Å" is written.

**Fig. 4.1.** STM images showing the evolution of the island density as a function of the substrate temperature for deposition of Al on Al(111) ( $\theta = 0.15$  ML, flux =  $6.2 \times 10^{-4}$  ML / s). Sizes and deposition temperatures as indicated.



range no change of the critical nucleus size occurs. This qualitative picture is reflected by the Arrhenius plot of the island densities extracted from the STM data shown in Fig. 4.2.

KMC calculations performed by Bogicevic et al. [56] indicate a diffusion barrier for an Al dimer on the Al(111) surface of  $E_{m-dimer} \cong 120$  meV and that dimer dissociation takes place only at elevated temperatures. Since the dimer diffusion barrier is much higher than the terrace diffusion barrier, the island density remain determined by the monomer density up to temperatures of 180 K. A similar behaviour has been observed for the growth of Si on the Si(001) surface. For this system dimer diffusion sets in at  $\approx 300$  K, but the island density remains determined by the monomer density up to  $\approx 600$  K [57, 58]. In the studied temperature range the dimer is thus assumed to be stable, which implies that the critical nucleus size is  $i = 1$  [56]. The same result has been obtained by Stumpf and Scheffler [50] using *ab initio* methods. They found a

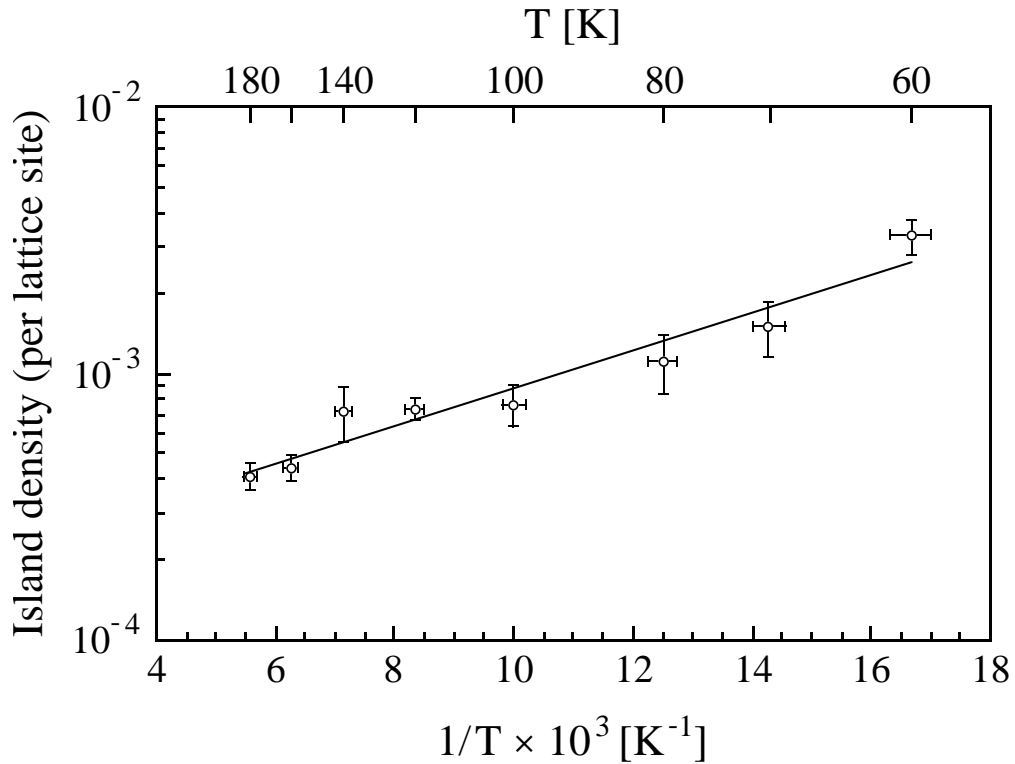


**Fig. 4.2.** Arrhenius representation of the saturation island densities derived from averaging over series of STM images obtained on different substrate areas for each temperature ( $\theta = 0.15$  ML, flux =  $6.2 \times 10^{-4}$  ML/s). The island densities were corrected for lateral drift by considering drift vectors of consecutive images.

binding energy for the Al dimer of 0.58 eV and, as a consequence, the dimer to be stable below 250 K. From the slope and intercept of the straight line fitted to the island densities in Fig. 4.2, a diffusion barrier of  $E_m = 42 \pm 4$  meV and an attempt frequency of  $\nu_0 = 8 \times 10^{6 \pm 0.25} \text{ s}^{-1}$  are extracted respectively (see § 3.2).

This surface diffusion barrier is the lowest barrier ever measured for a homoepitaxial metal-on-metal system. An even smaller barrier has been found for the case of the heteroepitaxial growth of Al on Au(111) (see chapter 5). The extremely low diffusion barrier leads also to step decoration even at the lowest measured temperature (60 K).

At a temperature of 100 K aluminum grows 3-D as shown by the image in Fig. 4.3. For coverages as low as  $\theta_{Al} = 0.4$  ML small second layer islands form on the largest islands of the first layer. The interlayer mass transport is hindered by a high step-edge diffusion barrier (Ehrlich-Schwöbel). This can also be seen on Fig. 4.1a where no depletion zone is observed near the descending step edges. It is not surprising to find a high step-edge barrier, because most cases of homoepitaxy on close-packed metal surfaces studied so far exhibit multilayer growth, i.e. limited interlayer mass transport [44, 59]. This additional step-edge barrier is a decisive quantity determining the film morphology. From the STM image in Fig. 4.3 we can estimate the Ehrlich-Schwöbel barrier for Al on Al(111), employing an approach proposed by Meyer et al. [60]. Their method takes into account the fact that second-layer islands nucleate only when the first-layer islands reach a critical size. Upon measuring in STM images the corresponding critical radius (assuming a circular shape for the island) and the distance between the centers of first-layer islands, it is possible to estimate the additional step-edge barrier using the following relation:

$$\frac{R_{1,c}}{R_{0,c}} = \left( \frac{h_0}{h_1} + \frac{2 \exp(\Delta E_s / kT_s)}{R_{1,c}} \right)^{1/2} \quad (4.1)$$

$R_{1,c}$  is the critical size of the first layer island before second layer island nucleation occurs on top of it.  $R_{0,c}$  is the average distance between the centers of the first layer islands. The hopping probabilities on the bare surface and on the first layer are  $h_0$  and  $h_1$ , respectively. In case of homoepitaxy  $h_0 = h_1$ .  $\Delta E_s$  is the value of the additional step-edge barrier. Inversing Equation 4.1 in order to extract  $\Delta E_s$  yields:

$$\Delta E_s = kT_s \ln \left( \left( \left( \frac{R_{0,c}}{R_{1,c}} \right)^2 - 1 \right) \frac{R_{0,c}}{2} \right) \quad (4.2)$$

$R_{0,c}$  is difficult to determine analytically with precision due to the lack of symmetry of the first layer islands. However, it is possible to extract a reasonable value for  $R_{0,c}$  from the the Arrhenius representation of the saturation island density<sup>5</sup> (see Fig. 4.2). Applying Equation 4.2 for a temperature of 100 K, with  $R_{1,c} \approx 7$  lattice units extracted from the STM data and  $R_{0,c} \approx 42$  lattice units from Fig. 4.2, the estimation of the additional step-edge barrier yields:  $\Delta E_s = 57 \pm 20$  meV (the error in this result is dominated by that in the approximation of  $R_{0,c}$  and that of the critical size for nucleation of the second layer islands  $R_{1,c}$ ).

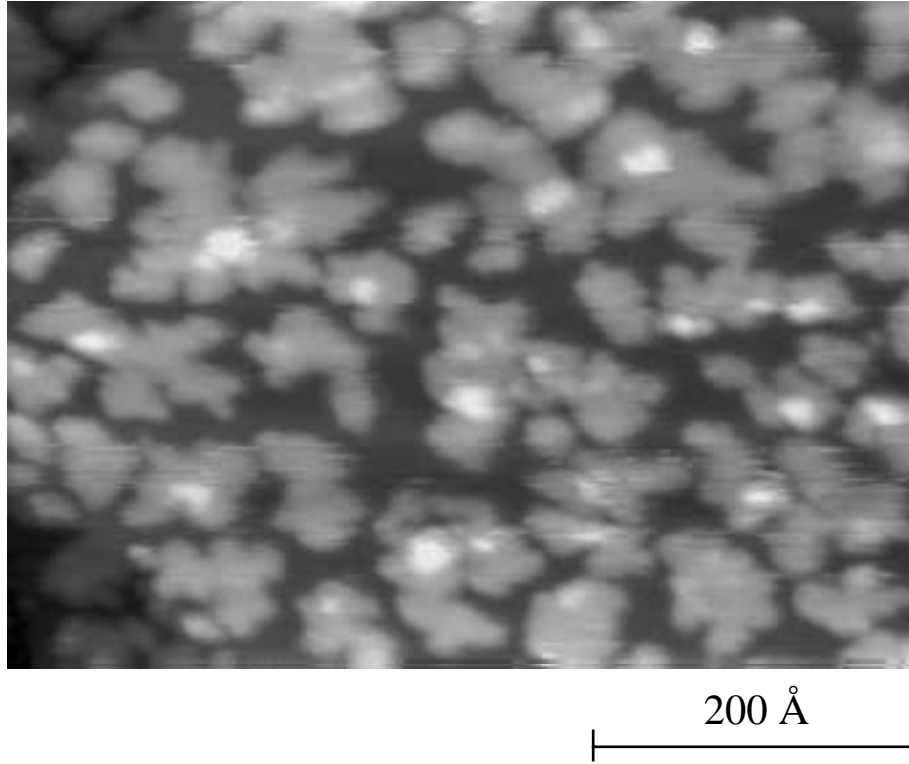


**Fig. 4.3.** Growth morphology of Al on Al(111) at 100 K. Second layer nucleation sets in at a coverage of  $\theta \cong 0.4$  ML (flux =  $6.2 \times 10^{-4}$  ML / s).

<sup>5</sup> By inverting the saturation island density, it is possible to extract the mean diffusion length of adatoms, which corresponds to the half of the average distance between two islands of the first layer.

### 4.2.2 Islands shapes

The island shape is influenced by the mobility at the island perimeter and the lateral impingement rate. Since the perimeter mobility depends on the temperature it is possible to control the island shape via the substrate temperature. At high temperature, islands are usually large and compact, and their shape is strongly influenced by the substrate symmetry. It is well known from earlier studies that on substrates with trigonal symmetry (e.g. (111) surfaces) in general hexagonally distorted islands evolve [61], while substrates with square or rectangular symmetry (e.g. (100), or (110) surfaces) lead to formation of square or rectangular islands [62, 63]. The reason for the compact shape is the high edge mobility of the deposited adatoms and the thermodynamic driving force to reduce the perimeter length for a given island size. At high enough temperatures the adatom thermal energy is usually much larger than the terrace step-edge barrier and therefore, the islands can reach their thermodynamic equilibrium shape. At low temperature this is not the case. The island shape is then governed by the growth kinetics. In addition to the substrate symmetry, processes as diffusion along the steps, terrace diffusion and flux play a major role. Depending on the respective energy barriers of these microscopic processes, different island shapes may evolve. As an example, fractal or dendritic two-dimensional adatom islands could be grown at low temperature by homoepitaxial or heteroepitaxial deposition on a fcc (111) or hcp (0001) surfaces [61, 64-68]. The substrate temperature is not the only external parameter that controls the island shape. E.g., Ag islands on Pt(111) exhibit a transition between randomly ramified and dendritic islands upon variation of the deposition flux  $R$  [24]. In the case of heteroepitaxy, the island shape may also be influenced by the strain due to the lattice mismatch between substrate and deposit material. This phenomenon will be further developed in chapter 6 for the case of Cu on Ni(100).

A series of STM images revealing the shapes of Al islands on Al(111) formed at different deposition temperatures is reproduced in Fig. 4.4. A consequence of the very low diffusion barrier measured for the Al/Al(111) system is that big compact islands still evolve at 200 K (Fig. 4.4e). Closer inspection reveals a quasi hexagonal shape of these compact islands. The system has thus reached its equilibrium, since for the (111) surface the hexagonal shape is the expected thermodynamic equilibrium shape. At a deposition temperature of 160 K the islands remain compact and mainly of hexagonal shape (Fig. 4.4d). At 140 K most islands are compact, however, some of them are slightly ramified (Fig. 4.4c). Upon lowering the deposition temperature to

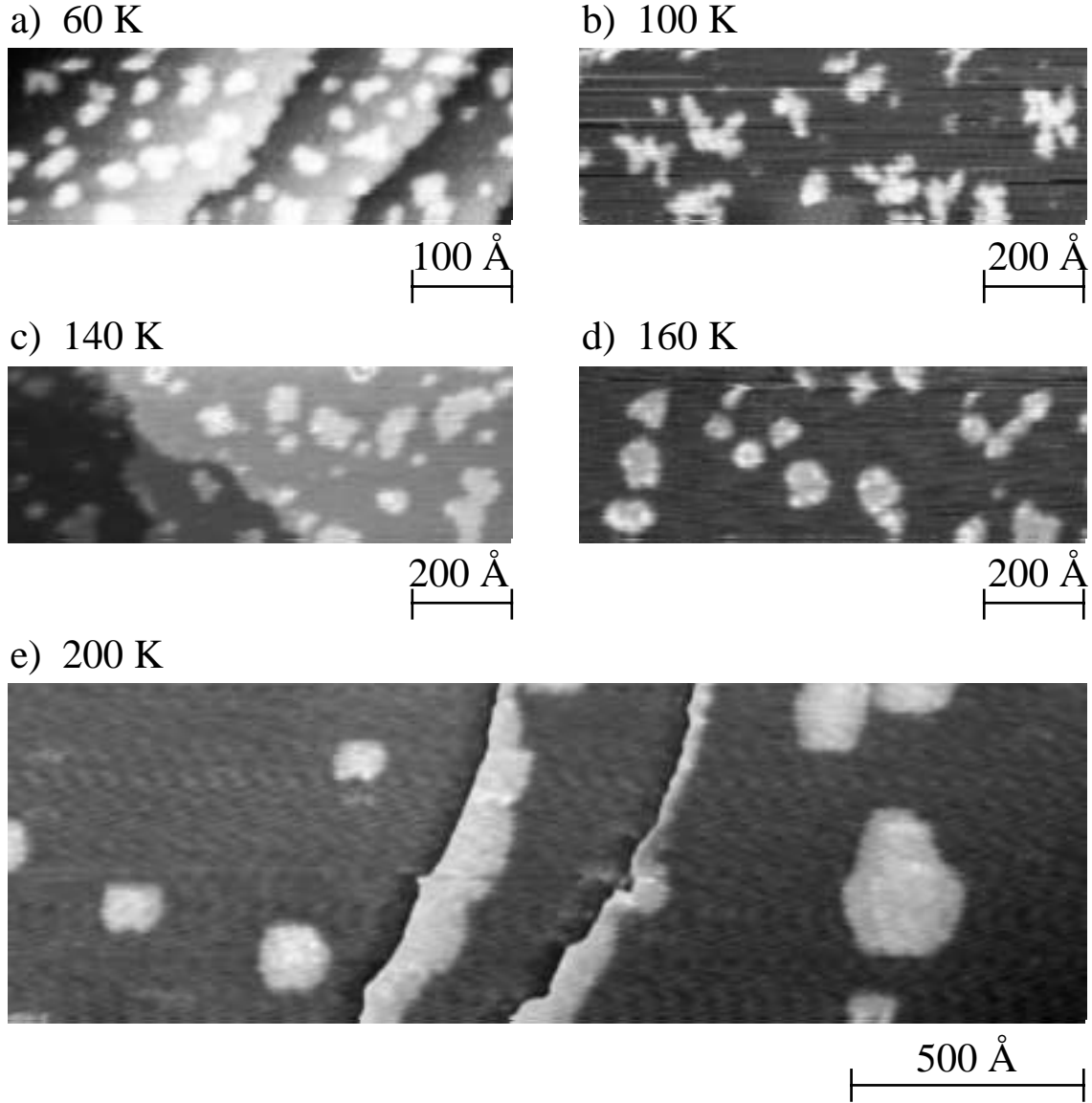


**Fig. 4.4.** STM images showing the evolution of island shapes as a function of growth temperature for Al on Al(111) ( $\theta = 0.15$  ML, flux =  $6.2 \times 10^{-4}$  ML/s). Image sizes and deposition temperatures are indicated.

100 K (Fig. 4.4b) the ramification of the islands is clearly obvious. At this temperature, the system is no longer in its thermodynamic equilibrium. The island shape is determined mainly by kinetic limitations. The islands have an average spatial extension of about 120 Å and an armwidth of  $\approx 25$  Å. At a deposition temperature of 60 K (Fig. 4.4a), islands appear compact again, however they are also very small.

### 4.3 Comparison of STM results with *ab initio* calculations

The morphology of a growing surface is governed by the microscopic adatom-surface interaction, especially at binding sites and along the pathway of the surface diffusion. If the rates for all relevant diffusion processes are known, the evolution of the surface during growth can be calculated. Using *ab-initio* DFT-LDA, Stumpf and Scheffler [50, 69], and later Ruggerone et al. [70] investigated properties of Al(111), Al(100), Al(110) and stepped Al(111) surfaces. Among others, they predicted adsorption energy and diffusion barriers for Al adatoms on these surfaces. In addition they estimated the temperature range for different modes of homoepitaxial growth on Al(111). Finally they presented a discussion of island shapes on Al(111) in thermodynamic equilibrium with respect to the deposition temperature  $T_s$ . The objective of the present section is to compare their results to the experimental data obtained for the Al/Al(111) system.

Of particular interest is the energy barrier for self-diffusion on Al(111)  $E_m$ . The experimental value of  $42 \pm 4$  meV extracted from Fig. 4.2 in section 4.2, is in excellent agreement with the calculated value obtained by Stumpf and Scheffler (40 meV). The chosen pre-factor for their calculation was  $2 \times 10^{-4} \text{ cm}^2 \text{ s}^{-1}$ , corresponding to an adatom attempt frequency of  $3 \times 10^{11} \text{ s}^{-1}$  (See Table 4.1). This value differs by more than 4 orders of magnitude from the experimental value of  $8 \times 10^{6 \pm 0.25} \text{ s}^{-1}$ . This large difference cannot only be attributed to compensation effects [71, 72]. The low value obtained for the attempt frequency will be discussed in section 5.5 in conjunction with results for similar systems. The estimated Ehrlich-Schwöbel barrier given by Equation 4.2 ( $\approx 60$  meV) is also in good agreement with the calculated values for descending both {111} and {100} steps when an exchange mechanism is assumed (80 and 60 meV, respectively) [70].

Using the calculated surface diffusion barrier and estimated prefactor, Ruggerone et al. predicted the surface morphology as a function of the deposition temperature. At room temperature simulations may not be reliable because the concept of single jump between nearest neighbor sites is no more valid. Due to the low diffusion energy (comparable to the energy of surface phonons of Al(111) [73, 74] a single phonon can furnish enough energy to an adatom for leaving its adsorption site and diffusing on the flat surface. They limited therefore the study to substrate temperatures below 250 K.

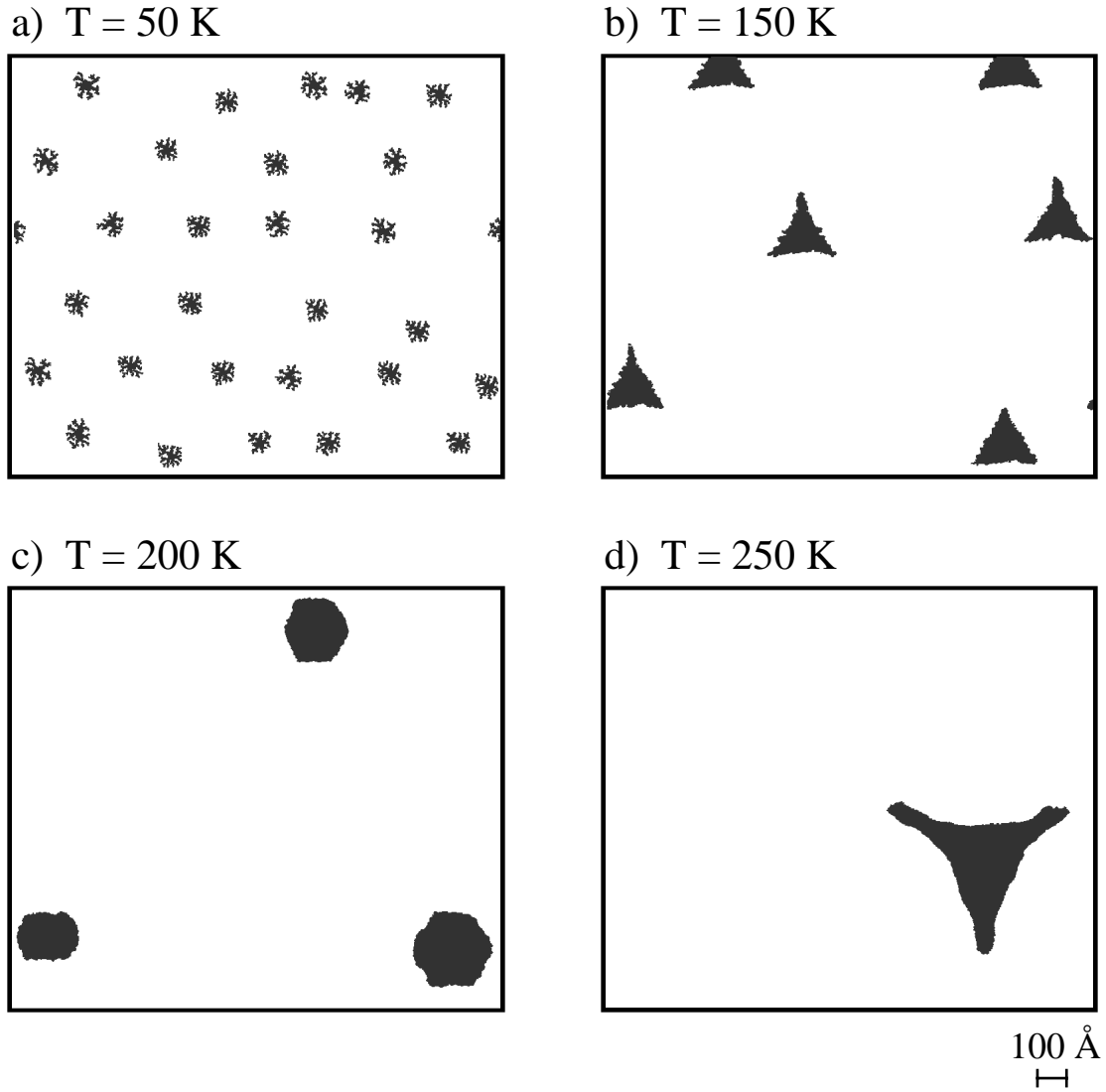


**Fig. 4.5.** Predicted island shapes at different substrate temperatures (the deposition rate was 0.08 ML/s and the coverage is  $\theta = 0.04 \text{ ML}$ ). From [70].

At 50 K Ruggerone et al. predict a fractal shape (see Fig. 4.5a), i.e. ramification takes place into random directions and the island formation could be understood in terms of a "hit and stick" mechanism [75, 76]. The calculations however, disregard the relaxation for the corner to A-step, which is known to be always active [66]. Our STM measurements performed at 60 K show compact rather than fractal islands. A possible way to decide if the compact shape observed at 60 K is the real island shape or if it is obstructed by tip convolution effects, is to extract the average area of each island from Fig. 4.2 and to calculate the island diameter

	Simulations [50, 70]	Experimental
$E_m$ (meV)	40	$42 \pm 4$
$\nu_0$ ( $s^{-1}$ )	$3 \times 10^{11}$ (estimated)	$8 \times 10^{6 \pm 0.25}$
$\Delta E_s$ (meV)	{100} – step : 60 / {111} – step : 80	$57 \pm 20$
$T_s \approx 50$ K	fractal growth	compact
$T_s \approx 100$ K	–	ramified
$T_s \approx 150$ K	triangular {100}-faceted steps	compact / $\approx$ hexagonal
$T_s \approx 200$ K	hexagonal	hexagonal
$T_s \approx 250$ K	triangular {111}-faceted steps	–

**Table 4.1.** Experimental and simulated values for the surface diffusion barrier  $E_m$ , the attempt frequency  $\nu_0$ , the additional step-edge barrier  $\Delta E_s$  and comparison between the predicted and observed islands shapes for the Al/Al(111) system.

assuming the dimensionality. If DLA is assumed the dimensionality is  $D = 1.7$  [75, 76], leading at 60 K to an island diameter of about  $65 \text{ \AA}$ , whereas for compact island ( $D = 2$ ) an diameter of about  $40 \text{ \AA}$  is expected. Even with a poor resolution of the STM images, it is thus possible to identify if growth proceeds by a DLA mechanism or not. The islands in Fig. 4.1a have a diameter of about  $40 \text{ \AA}$ , ruling out DLA islands.

At 150 K, due to the difference between the mobility along the two kinds of close-packed steps which are foreseen to dominate the periphery of islands on an fcc (111) surface [61], a triangular shape is expected with the sides of the islands being {100}- faceted steps (see Fig. 4.5b). Data taken at 140 and 160 K show, however, compact islands (Fig. 4.4c and d) closer to hexagonal than to triangular shape. The step edge diffusion remains thus activated even at these temperatures, and the values for diffusion along both kind of close-packed steps ({100} and {111} directions) are approximately equal. At 200 K, both simulations and measurements give hexagonal shapes, as demonstrated by Figs. 4.4e, 4.5c and Table 4.1. At 250 K a triangular island shape with the sides of the islands being {111}- faceted steps is predicted. Due to the finite size of terraces, no STM data of isolated islands could be obtained at this temperature and thus a comparison is impossible.

Overall, there is only poor agreement between predicted islands shapes and experimental observations. The major reason is that several atomic diffusion processes crucial for island shapes on hexagonal lattices have been disregarded by Ruggerone et



al.. Two reasons may be particularly important for the observed differences. Firstly, at very low temperature the simulations diffusion of adatoms at a corner site towards a step-edge was prohibited. As a result, classical DLA-islands with monatomic branches were predicted at 50 K. However, the assumption of corner diffusion to be frozen in is not realistic since it is known from previous studies (e.g. Ag/Pt(111) [77]) that with terrace diffusion activation, corner diffusion is also possible. Secondly, calculations with EMT indicate that diffusion around a corner site (corner crossing) has generally a slightly larger barrier than diffusion along a step-edge [78, 79]. Ruggerone et al. do not mention that this difference has been considered in their Al/Al(111) island shapes simulations. Presumably it was assumed that diffusion along a step-edge and corner crossing have the same barrier, and hence triangular islands could be obtained. At 150 K the simulation predict triangular islands terminated by A-steps, in contrast to experiment where islands exhibits both step types. The simulations by Ruggerone et al. assume two diffusivities along the two step orientations and get triangles with that step edge prevailing which has the higher diffusion constant. This picture is similar to the mechanism proposed for triangular Pt on Pt(111) islands by Michely et al. [61]. A recent study by Jacobsen et al., however, demonstrates that triangular islands require different adsorption energies for each step type [78, 79]; and that different edge diffusion barriers with the same adsorption energy at both edges, yield hexagonal compact islands. Therefore, regarding the results by Jacobsen et al., our hexagonal, compact islands observed at 140 K (200 K) are compatible with different diffusion barriers along A and B-steps also suggested from *initio* calculations [50].

## 4.4 Conclusion

Homoepitaxy of Al on the Al(111) surface has been investigated by means of variable temperature STM. The derived surface diffusion barrier for monomers of 42 meV is the lowest diffusion barrier ever measured for a metal-on-metal homoepitaxial system. Barriers of the same magnitude have only been found for the Al/Au(111) system (see chapter 5). *Ab initio* simulations performed by Stumpf et al. predicted a diffusion barrier of 40 meV, which is confirmed by our experimental value. The surprisingly low attempt frequency found in experiment ( $\approx 1 \times 10^7$ ) is about 5 orders of magnitude lower than the common pre-exponential factor. This result will be discussed in section 5.5. Due to oversimplifications the evolution of the island shape as a function of the deposition temperature simulated by Ruggerone et al. mostly disagrees with the experimental data (see Table 4.1).

## Chapter 5

# **Nucleation kinetics on a substrate with dislocations: Al/Au(111)**

### 5.1 Introduction

There is considerable interest in a fundamental understanding of the kinetics of thin film growth since metal epitaxy, and also MBE growth of semiconductors, is often governed by kinetics rather than by thermodynamic properties of the surfaces and interfaces (see e.g. [80-82]). The kinetics of epitaxy is determined by the interplay of the atomic diffusion, nucleation and dissociation processes involved. For metals such processes have been studied intensively since many years by means of Field Ion Microscopy (FIM) [42, 83, 84]. Recent STM studies established the link between the activation energies of atomic displacement processes and island densities, shapes and the film morphology [57, 59, 85-87]. Due to these experimental and various theoretical studies, our understanding of the initial stages of thin film growth considerably improved during the last few years. This is particularly true for nucleation on isotropic substrates, where the available experimental results are consistently described by nucleation theories and kinetic Monte-Carlo simulations. Also nucleation and growth on anisotropic substrates has to some extent been addressed in experiment [63, 88-90] and theory [91].

Many surfaces in nature, however, are either reconstructed in their clean state or become restructured during growth. In heteroepitaxial systems, often strain induced dislocation patterns evolve where surface stress is partially relieved. Dislocations may even play a role in homoepitaxy, where they can be induced by the chemical potential of the adatom gas on a surface under tensile stress [92]. It is important to notice that substrates with dislocations belong to a class that we call inhomogeneous, i.e., their structure and also diffusion barrier, as we will see below, vary strongly upon translation. A quantitative understanding of nucleation on inhomogeneous substrates revealing dislocations is still missing. From several observations reported in the recent literature [93-95] it can be concluded that dislocations represent considerable repulsive barriers for diffusing adatoms whereby they may entirely dominate nucleation and growth. This fact, and their frequent appearance, necessitates a quantitative study of the role of surface dislocations on adatom diffusion and nucleation kinetics.

In this chapter, we present the first systematic study of nucleation kinetics on a substrate revealing a periodic arrangement of dislocations, namely the  $(\sqrt{3} \times 22)$ -reconstructed Au(111) surface. We study Al epitaxy on this substrate as a function of temperature by means of STM. In contrast to earlier room temperature studies of nucleation of Ni [18, 96-99] and Co [100, 101] on Au(111), we observe that the dislocations are repulsive towards Al diffusion and there is no preferential nucleation at the elbows of the chevron reconstruction. A particular property of many heteroepitaxial systems is the tendency towards alloy formation. For the case of Ni on Au(111), it was demonstrated recently that intermixing is site specific giving rise to preferential island formation at reconstruction elbows [18]. In contrast to former room temperature studies, in the present experiments effects of alloying can be suppressed by variation of the deposition temperature enabling the study of pure adatom diffusion up to alloy formation. In the adatom regime there is a transition from diffusion confined to the pseudomorphic stacking areas to crossing of dislocations. This transition is identified by a drastic change in slope in the Arrhenius representation of the saturation island density indicative for a strongly repulsive barrier of dislocations. Well beyond this transition we observe the onset of intermixing which is presumably site specific and can be identified by the island size distributions. Intermixing finally induces a strong modification of the otherwise preserved chevron reconstruction to a dislocation pattern with hexagonal symmetry. This transition in surface morphology is again associated with a change in nucleation island densities. A modification of the Au(111) reconstruction upon deposition of aluminum has already been observed by Krzyzowski employing of HAS measurements [102].

In section 5.2 a brief description of the "chevron" reconstruction of Au(111) is presented. STM results and island size distributions are shown in section 5.3. Section 5.4 contains a short description of the kinetic Monte-Carlo method and the results of the simulations and finally section 5.5 compares the pair  $\{E_m, v_0\}$  for several metal on metal system studied so far.

## 5.2 The $(\sqrt{3} \times 22)$ reconstruction of the Au(111) surface

Each atom of a surface has a reduced number of nearest neighbors. As a consequence, the general trend of the surface atoms is to reduce their bond length (up to 10% shorter [103]), leaving the surface under tensile stress. This tensile stress can be the driving force for a surface reconstruction. E.g. for a fcc(111) surface the number of nearest neighbors is reduced by 3 when passing from the bulk (12) to the surface (9). Moreover at a surface, the electrons are free to rearrange their distribution in space to lower their kinetic energy. The resultant smoothing of the surface electronic charge density leaves the surface ions out of electrostatic equilibrium position with the modified asymmetrical screening distribution. The net force on the ions points primarily into the crystal and usually drives a contractive relaxation of the surface plane until equilibrium is reestablished. The in-plane structure generally retains the characteristics of the ideal surface termination. However, for some surfaces, the in-plane structure is modified. The reconstruction of the surface commonly yields geometrical structures that are much more complex than ideal surface termination.

Many systems undergo a reconstruction. The reasons that force a system to reconstruct are various: adsorbates (e.g. H/Ni(110) or O/W(100) [13, 104, 105]), presence of a highly supersaturated gas-phase (e.g. Pt/Pt(111)<sup>6</sup> [92]) or temperature variation (e.g. Ir(100) or Au(110)<sup>7</sup> [107]). At room temperature the gold (111) surface is the only (111) surface of an fcc metal that is known to be reconstructed in its ground state [11].

The Au(111) terraces exhibit a periodic pattern of pairwise-arranged parallel lines, running in the  $[11\bar{2}]$  direction (corrugation lines), as it can be seen in Fig. 5.1a.

---

<sup>6</sup> The Pt(111) surface spontaneously reconstruct if the temperature exceeds approximately 1330 K [106].

<sup>7</sup> The Ir(100) surface undergoes a reconstructive  $1 \times 1 \rightarrow 1 \times 5$  transformation at temperatures exceeding 800 K. At about 650 K, the high temperature  $1 \times 1$  structure of the Au(110) surface reversibly transforms into the  $2 \times 1$  "missing row" structure.

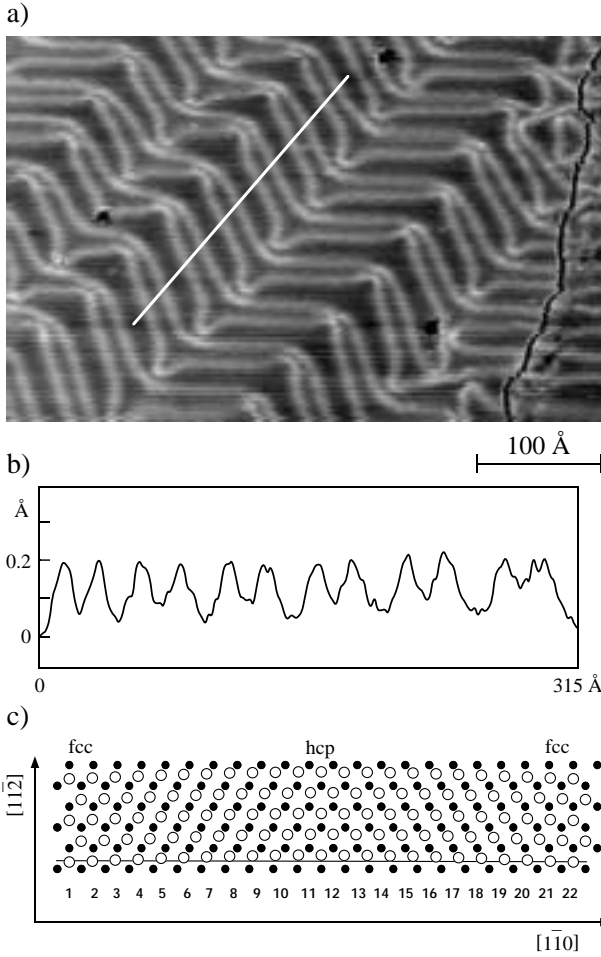


**Fig 5.1.** a) STM image of the "chevron" reconstruction of clean Au(111) recorded at room temperature. The corrugation lines run in the  $[11\bar{2}]$  direction with a periodicity of 63 Å and a corrugation of about 0.2 Å b) line scan parallel to the elbows showing the height modulation of the reconstruction. c) ball model of the uniaxial contraction along the  $[1\bar{1}0]$  close-packed directions with the fcc-hcp stacking transition. The white dots represent the atoms of the outermost layer, the black dots represent the atoms in the second layer.

These corrugation lines separate fcc stacking regions from hcp stacking regions. The distance between neighboring pairs (in  $[1\bar{1}0]$  direction) amounts to 63 Å; the individual lines within a pair are about 44 Å apart. The measured corrugation amplitude (from the line scan in Fig. 5.1b) was found to be  $0.20 \pm 0.05$  Å. The lattice vectors of the reconstruction unit cell are given by the connection between adjacent main minima, 63 Å in the  $[1\bar{1}0]$  direction, and by the connection between nearest next-neighbor  $[1\bar{1}0]$  rows of Au atoms, 4.7 Å in the  $[11\bar{2}]$  direction, respectively. This leads to a  $\begin{pmatrix} 22 & 0 \\ -1 & 2 \end{pmatrix}$  unit cell [11]. There are 23 Au surface atoms per unit cell on 22 bulk lattice sites, corresponding to an average uniaxial contraction of 4.55%. Fig. 5.1c shows a ball model of the contraction of the atomic distances. Atomic resolution data show that the contraction is not confined to the transition regions [11]. Three different rotational domains exist. On large atomic terraces the transition from one domain to another one occurs by a correlated bending of the corrugation lines by  $120^\circ$  (see Fig. 5.1a). The term "chevron" structure results from an additional long-range periodicity in the reconstructed layer: Entire sets of corrugation lines change their orientation in a zig-zag pattern by  $\pm 120^\circ$  and thus form a periodic sequence of domain boundaries. The distance between these domain boundaries amounts to about 250 Å. This periodic sequence of domain boundaries leads to a more uniform contraction on the surface, while a single uniaxial domain would lead to stress relieve only in one direction.

### 5.3 Nucleation and diffusion behaviour

A series of STM images characterizing the nucleation of 0.1 ML Al on Au(111) as a function of substrate temperature is reproduced in Fig. 5.2. First, we will concentrate on the variation of island density. There is an overall decrease in island density with increasing temperature. Closer inspection reveals that this decrease is not continuous, rather three nucleation regimes with qualitatively different behavior can be identified. Below 200 K, only small variations of the island density are induced by relatively large temperature changes. This is demonstrated in Figs. 5.2a and 5.2b which were recorded for  $T_s = 150$  K and 200 K, respectively. The island density then drops much more rapidly in the range from 200 K to 245 K, as seen by comparison of Figs. 5.2b and 5.2c (notice the change in scale by a factor of two). Above 245 K, a third nucleation regime is entered characterized by an even stronger variation of island densities with temperature. A difference in deposition temperature of merely 10 K separates the data in Fig. 5.2d from 5.2e, nevertheless inducing a reduction of the island density by more than one order of magnitude.

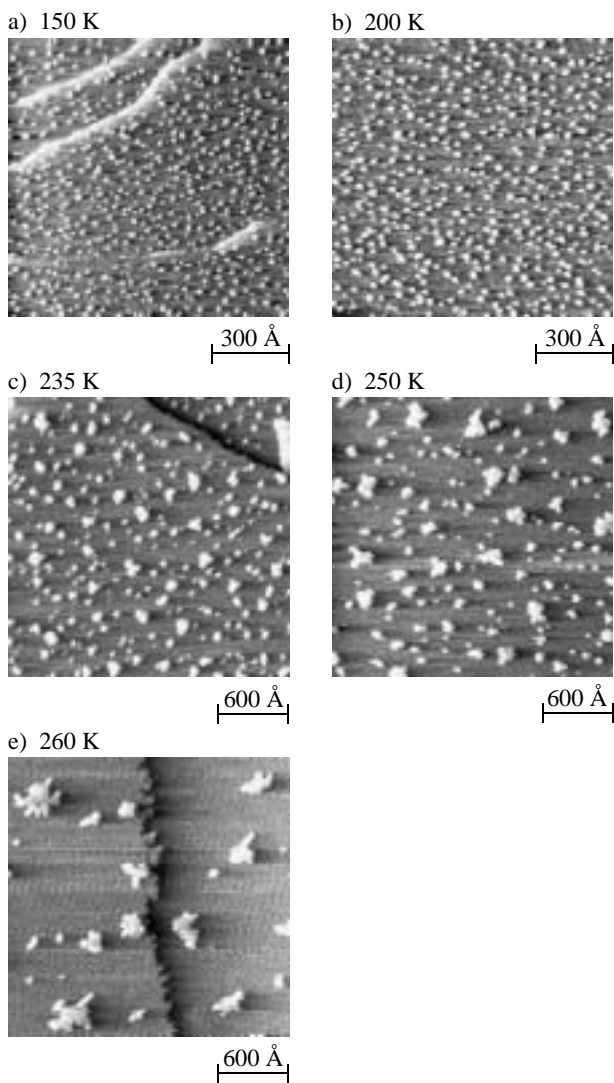


**Fig. 5.2.** STM images showing the evolution of island density, size and shape as a function of temperature for Al deposition onto Au(111) ( $\theta = 0.1$  ML, flux =  $3.2 \times 10^{-4}$  ML / s). Image sizes and deposition temperatures as indicated.

This qualitative picture is reflected quantitatively in three different slopes in the Arrhenius representation of the island densities shown in Fig. 5.3. The island densities have been obtained at coverages in the saturation regime, they therefore represent the mean free path of diffusing adatoms at the various temperatures under the applied deposition flux. It is well known from nucleation mean-field theory (see § 3.2) that slopes (and intersections with the abscissa) in the Arrhenius plot of saturation island densities are related to migration barriers (and the corresponding attempt frequencies). Therefore the drastic change in slope occurring at 200 K indicates a significant change in diffusion barrier, followed by a second, although less pronounced change at 245 K. Fig. 5.5a shows the island size distribution at a temperature of 150 K. The calculated distribution for  $i = 1$  is in good agreement with the experimental data [47, 91]. The critical nucleus size for temperatures below 200 K from the island size distributions is thus  $i = 1$ . The change of slope at 200 K in the Arrhenius representation of the saturation island density amounts to a factor 18 and consequently, cannot be rationalized with simply a change of the critical cluster size.

To understand the physical reason for the diffusivity changes we have to look closer at the substrate during nucleation. The STM image represented in Fig. 5.4a shows the surface after deposition of a very small amount of Al at 150 K. The well ordered pattern of the herringbone reconstruction characteristic for the clean surface [11] is clearly visible. (The dark spots at the elbows are vacancies attributed to tip-surface interactions which occur occasionally and were reported before [108].) This reconstruction pattern remains preserved up to deposition temperatures of about 240 K; then it is transformed into a domain pattern with quasi-hexagonal symmetry (see Fig. 5.4b obtained after Al deposition at 300 K) [109]. In agreement with this observation HAS experiments reported an unperturbed diffraction pattern of the Au(111) reconstruction for Al deposition up to 230 K, whereas at higher temperatures a symmetry change becomes detectable [110]. The Al induced reconstruction pattern displayed in Fig. 5.4b is attributed to Al-Au surface atom exchange processes and will be described in chapter 6. From the coincidence of the change in substrate structure at around 240 K with the change in slope at 245 K in Fig. 5.3, the increased diffusivity of Al atoms above 245 K is attributed to the structural transformation of the substrate (see chapter 6).

Since the reconstruction remains unperturbed below 245 K the first change in the slope at 200 K must have a different origin. From Fig. 5.4a it is obvious that most of the aluminum islands are located in the pseudomorphic stacking areas (there is



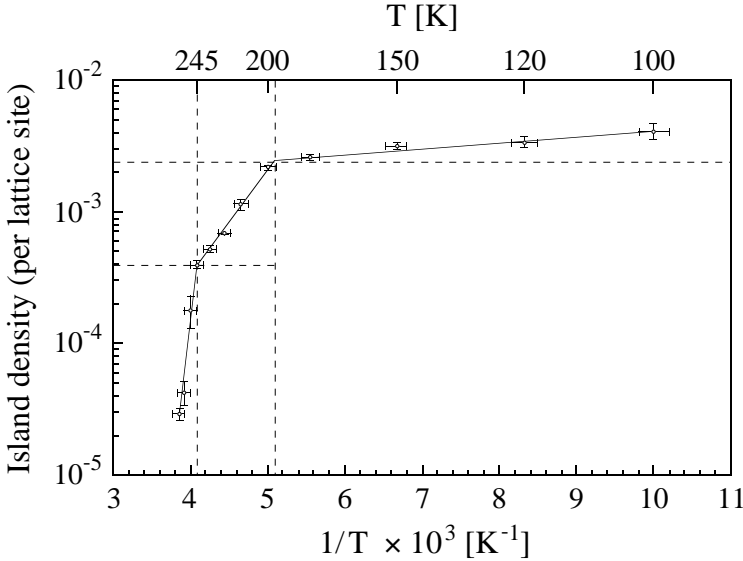


**Fig. 5.3.** Arrhenius representation of saturation island densities derived from averaging over series of STM images obtained on different substrate areas for each temperature ( $\theta = 0.1$  ML, flux =  $3.2 \times 10^{-4}$  ML / s). The island densities were corrected for lateral drift by considering drift vectors of consecutive images.

a preference for fcc areas due to their increased width). Apart from this, however, there is no preference for nucleation at any particular site of the reconstruction pattern. This is also reflected in the homogenous island distribution deduced from the STM images below 200 K (see Figs. 5.2a and b). These observations indicate that the partial dislocations of the reconstruction are repulsive barriers for diffusing Al adatoms. In addition the change in slope in Fig. 5.3 appears at a density where the mean island distance is 22 atoms (see the upper dashed horizontal line). This corresponds exactly to the periodicity of the reconstruction and thus strongly suggests that the increasing diffusivity is due to diffusion over dislocations associated with a high repulsive barrier. As already mentioned above, the change in slope at 200 K cannot be rationalized with a change in critical cluster size.

A very interesting and striking observation is the formation of large islands in coexistence with small ones for Al deposition for temperatures exceeding  $\approx 220$  K.

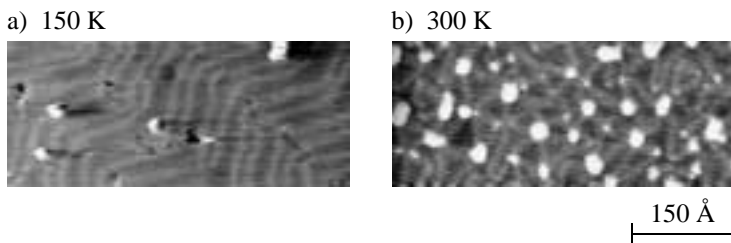


**Fig. 5.4.** a) STM image showing preferential Al nucleation in fcc domains and its absence at the elbows of the Au(111) reconstruction ( $\theta = 0.04$  ML,  $T_s = 150$  K). b) STM image showing the modification of the Au(111) surface reconstruction upon deposition of  $\theta = 0.07$  ML Al at  $T_s = 300$  K.

This effect is seen in Figs. 5.2c - e and expressed in the size distributions Figs. 5.5b and c as the appearance of a second peak at larger sizes. This behavior has not been observed so far and needs to be explained. From the observations above 245 K it is concluded that the Al/Au(111) system is unstable towards alloy formation. This involves atom exchange at the surface as a first step which may have less activation energy at certain sites, e.g., the elbows of the reconstruction [18]. One can therefore suspect that the large islands have nucleated in the very early stages of deposition, i.e., at the beginning of the "transient regime" [91] where the density of monomers linearly increases with coverage. At the beginning of this regime the total monomer density is thus very low implying a high mean free path of Al adatoms; they therefore may reach singular sites on the reconstructed surface where they can perform site exchanges. These early nuclei then grow in the course of further deposition until the monomer density has increased such that nucleation of adatom islands sets in. This rapidly diminishes the mean free path so that adatom nucleation and the growth of adatom islands dominate in the "steady state regime" of the monomer density [91]. The bimodal island size distributions obtained in this regime ( $\theta \approx 0.1$  ML) indicate two island ages, the elder, respectively larger ones originating from the early nucleation phase characterized by exchange at particular sites. In our system the energy barrier for exchange cannot be the rate limiting step, this would imply an increase in island density above a certain temperature since the number of jumps before making a place exchange increases with temperature [111]. The mobility determines whether sites for exchange are reached. This is the case in the early stage of deposition, whereas at later stages those sites are actually no more accessible due to the high density of adatom islands present on the surface. Since these adatom islands dominate by far the final island density in the

range from 200 K to 245 K, a straight line in the Arrhenius plot is observed and it is possible to treat the island densities as purely caused by adatoms.

Up to now, the following picture evolves. Below 200 K the Al adatoms are confined to the pseudomorphic stacking areas in-between the dislocations, whenever they move towards a dislocation they are reflected, however, they are free to move parallel to the dislocations. Above this temperature the island density reaches a threshold where adatoms must have diffused over dislocations leading to a change in the effective diffusion barrier. A quantitative analysis of the slopes in Fig. 5.3 obtained for adatom nucleation below and above 200 K, however, is hampered by the complicated structure of the substrate. In contrast to isotropic or anisotropic substrates, in our case, as in general for a pattern of dislocations, diffusion is inhomogeneous. The diffusion barrier therefore changes at certain sites, whereas it is constant and isotropic within the pseudomorphic areas, it increases upon approaching a dislocation. For this case there is no theoretical treatment so far. At 180 K the mean free path of an Al adatom is about 11 lattice spacings (this is half the island spacing at that temperature). Therefore the Al migration barrier on the pseudomorphic stacking areas can be calculated to a good approximation with isotropic nucleation theory (see § 3.2). From the island size distributions shown in Figures. 5.5a and b it is seen that the critical nucleus size below 200 K is  $i = 1$  [47, 91]. From the slope (and intersection) of the straight line fitted to the island densities below 200 K in Fig. 5.3 we obtain  $E_m = 30 \pm 5$  meV and  $\nu_0 = 1 \times 10^{3 \pm 1} \text{ s}^{-1}$  upon application of classical mean-field nucleation theory for complete condensation and 2D islands [112]. This value is the lowest diffusion barrier measured so far for metal diffusion on close packed metal surfaces. However, measurements for the Al(111) self-diffusion yield a similarly low value of 42 meV (See chapter 4). For comparison, a significantly higher barrier of 150 meV has recently been calculated for Au(111) self-diffusion (with density functional theory) [113].

The second slope in Fig. 5.3 characterizing the regime where the reconstruction is still unperturbed and adatoms diffuse over dislocations cannot be interpreted quantitatively in the frame work of mean-field theory. A quantitative analysis in order to extract an effective barrier for crossing of dislocations requires a kinetic Monte-Carlo simulation which is the subject of the following section.

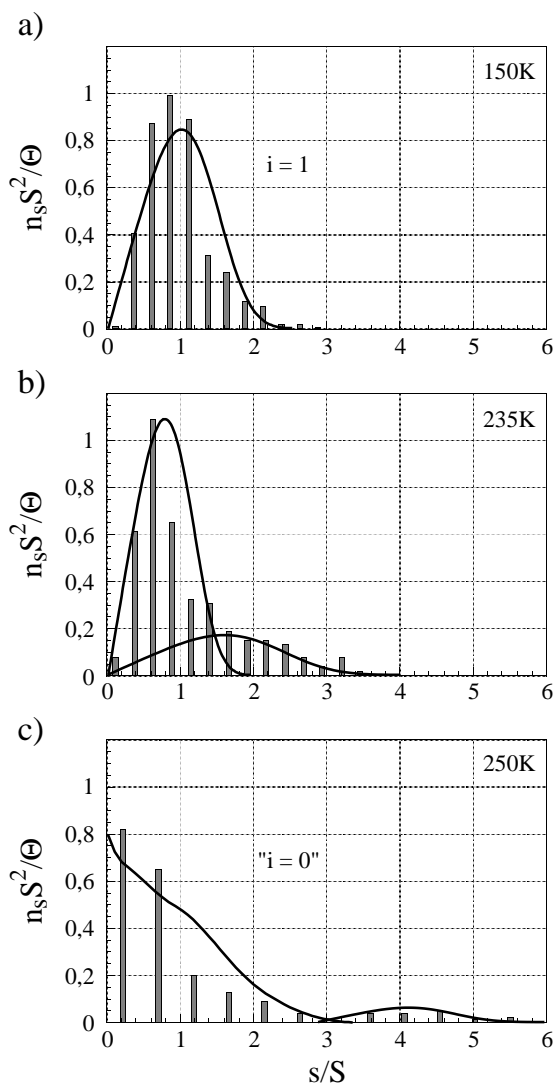


**Fig. 5.5.** Normalized island size distributions showing the transition from pure adatom nucleation with  $i = 1$  to the onset of intermixing leading to the appearance of bimodal island size distributions observable for  $T_y > 220$  K on.

## 5.4 Kinetic Monte-Carlo simulations

Dislocations can represent repulsive barriers for adatom diffusion, as seen in section 5.3. This fact is corroborated by EMT calculations performed for the Pt/Pt(111) system [114]. In these calculations the binding energy of the Pt adatom is found to decrease as it approaches a partial dislocation. The change in total energy is, however, small (half of the migration barrier). The calculations further show that the increase in potential energy of the adatom is a long range effect affecting  $\pm 4$  lattice sites adjacent to the partial dislocation. This long range effect implies that atoms have to make several successive jumps in energetically unfavorable directions to overcome a dislocation. A quantitative analysis of the two slopes (for  $T_s \leq 245$  K) in Fig. 5.3 in terms of activation energies for Al diffusion on the pseudomorphic areas and across dislocations on the Au(111) surface is not trivial, and therefore, requires realistic KMC simulations. In order to simulate the effect of the reconstruction on nucleation, we adopted a KMC code that was kindly provided by J. Jacobsen [115].

Due to the increasing importance of Kinetic Monte-Carlo (KMC), manifested by its frequent appearance in recent literature on epitaxial growth [116], a brief description of this technique is appropriate. In KMC simulations, the randomness of the spatial distribution of islands, as well as island-island interactions via the diffusion field are implicitly included. Various island shapes can also be incorporated. These simulations can therefore serve as a rather valid test for nucleation theory.

In a typical kinetic Monte-Carlo program<sup>8</sup> all displacement processes allowed for the atoms present on the surface are contained within a list. In this list, each atom can appear with several processes, e.g. with diffusion towards an island into a particular direction and regular terrace diffusion into all other directions. In the same manner an atom situated at a step can diffuse along the step into two opposite directions. On a square lattice, the third allowed movement for such an atom would be its dissociation from the edge towards the free terrace. The process list also includes the deposition of a new atom. There is a specific rate related to each type of process. These rates are jump rates,  $v_n = v_0 \exp(-E_n/kT_s)$  for diffusion, and  $v_{\text{dep}} = R \times (\text{system} - \text{size})$  for deposition of a new atom. To each process it is possible to associate a vector with a length corresponding to its rate. Now a pointer, driven by a random number generator, selects one vector among a field where all the vectors belonging to all possible processes are lined up. Thus, the probability for selecting a process is correctly made proportional to its frequency of appearance times its rate. After effecting the move of the selected

8

The description given here refers to a program written by J. Jacobsen [115], see also [117].

atom in the selected direction, the process list is updated since the coordination of the atom itself, and of its neighbors, might have been affected by the move. Again, a new random number is generated to select the next process from the list, and this procedure is repeated many times. Typically parameter files for  $T_s$ ,  $R$ ,  $v_0$  and  $E_n$  as well as the system size, which is periodically repeated are used. In principle, this is a simple program capturing the physical situation very well. However, a few drawbacks cannot be excluded: random number generators, which can be of poor quality [118], or finite size effects due to the limited system size [116] are reasons that may falsify the simulations results.

In the modified KMC code a diffusing adatom may feel different barriers, depending on the adatom position and the jump direction. Fig. 5.6a shows the model used for the simulations. The dark spheres are the pseudomorphic regions (fcc and hcp stacking). The dislocation lines are represented by the bright spheres. According to the EMT results for Pt/Pt(111) [114], these barriers are selected within a certain range around the dislocation ( $\pm 4$  atomic distances). In this range a diffusing adatom can feel three different barriers according to the diffusion direction (see Fig. 5.6c). Moving up and down a dislocation involves a diffusion barrier  $E_{dl\uparrow}$  and  $E_{dl\downarrow}$  respectively, terrace diffusion involves a diffusion barrier  $E_m$ . Different attempt frequencies  $v_0$  can be associated with each diffusion process. Reflecting the repulsive character of dislocations, the barriers for moving up dislocations were chosen larger than those for descending from the dislocations (cf. Fig. 5.6b). The barrier for diffusion within the pseudomorphic stacking areas enters as a third parameter. In order to elucidate the observed island densities, a systematic search with varying parameters was performed. The results from these extensive simulations permit to highlight the role of each parameter on the simulation.

- The general trend is a competition between the diffusion barriers and the attempt frequencies: Increasing the upward and downward diffusion barriers, keeping the attempt frequencies constant, leads to a change of slope at higher temperatures. Increasing the attempt frequencies, keeping the diffusion barriers constant, leads to a change of slope at lower temperatures.

- The slope for the high temperature regime ( $170 < T_s < 200$  K) is given by the total energy difference  $\Delta E$ .

As a result, it was found that the behaviour of the island densities in the entire regime below 245 K can be well reproduced for the following set of parameters (see Table 5.1.):

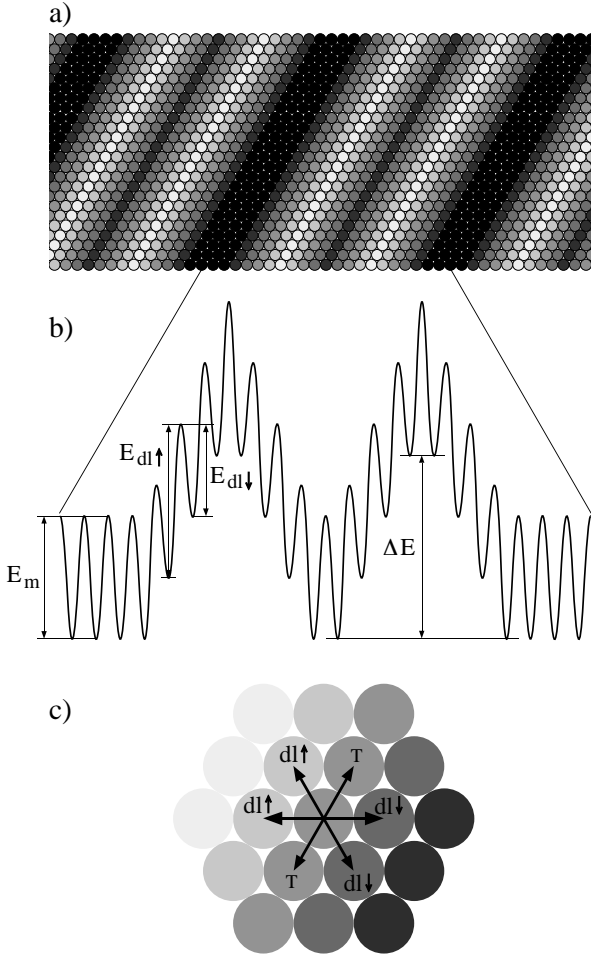


**Fig 5.6.** a) Ball model of the surface used for the Monte-Carlo simulations. Black spheres are in the pseudomorphic areas, the bright spheres represent the dislocation lines. b) Schematic picture of the potential energy surface characterised by three diffusion barriers.  $E_{dl\uparrow}$  is the barrier for upward diffusion when approaching a dislocation,  $E_{dl\downarrow}$  is the barrier for downward diffusion from a dislocation and  $E_m$  is the terrace diffusion barrier.  $\Delta E$  is the effective barrier for crossing the dislocations. c) Schematic picture of the three possible diffusion mechanisms for an atom situated close to a dislocation.

	Upward diffusion	Downward diffusion	Terrace diffusion
$E_{diff}$ (meV)	350	210	30
$\nu_0$ (s <sup>-1</sup> )	$2 \times 10^{13}$	$2 \times 10^{11}$	$2.4 \times 10^3$

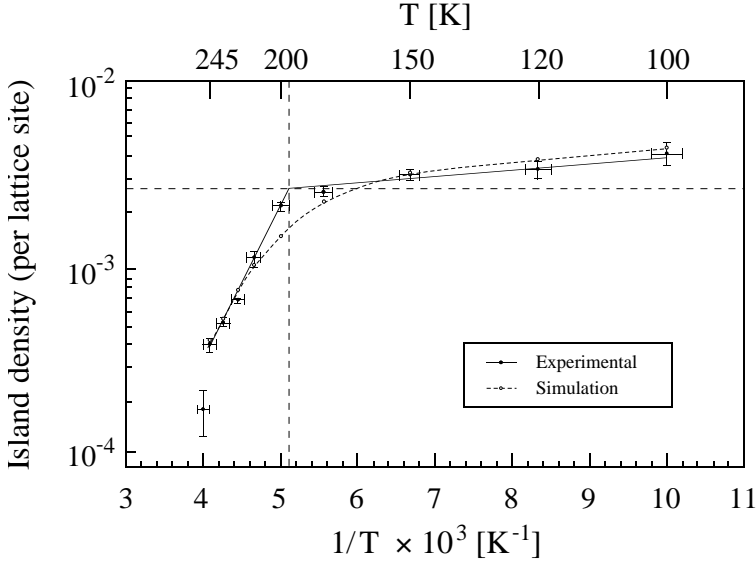
**Table 5.1.** Set of parameters used for the KMC simulations.  $E_{diff}$  is the diffusion barrier associated to each kind of diffusion processes.  $\nu_0$  is the attempt frequency associated to each diffusion process.

Fig. 5.7 shows in an Arrhenius representation both the experimental and the simulated values of the saturation island densities for  $T_s \leq 245$  K. In the low temperature regime, where deposited adatoms are confined in the pseudomorphic regions, and thus terrace diffusion determines the island density, the best fit is obtained with  $E_m = 30$  meV and  $\nu_0 = 2.4 \times 10^3$  s<sup>-1</sup>. Identical values for the migration barrier and attempt frequency are extracted from the slope for  $T_s < 200$  K upon application of mean-field theory for isotropic diffusion (see § 3.2). This indicates that in this regime the dislocations have only minor influence and isotropic nucleation theory is applicable.

At temperatures  $T_s > 170$  K, deposited adatoms can overcome the dislocation lines. In this regime upward and downward diffusion become the most important processes, and the best fit is obtained with an upward diffusion barrier of  $E_{dl\uparrow} = 350$  meV (attempt frequency  $\nu_{dl\uparrow} = 2 \times 10^{13}$  s<sup>-1</sup>) and a downward diffusion barrier of  $E_{dl\downarrow} = 210$  meV (attempt frequency  $\nu_{dl\downarrow} = 2 \times 10^{11}$  s<sup>-1</sup>). This set of diffusion barriers yields a total energy difference of 560 meV for an Al atom on-top of a dislocation compared to one in the pseudomorphic areas.

As can be seen in Table 5.1 attempt frequencies are associated with each diffusion barrier, which may differ one from another by many orders of magnitude. If the attempt frequencies for each diffusion process were equal ( $\nu_{dl\uparrow} = \nu_{dl\downarrow} = \nu_0$ ), adatoms could never cross the dislocation lines with the upward diffusion barrier being much larger than terrace diffusion barrier ( $E_{dl\uparrow} \gg E_m$ ). To reproduce the experimental data, one has thus to tune  $\nu_{dl\uparrow}$  so that at a certain point ( $\approx 200$  K)  $D_{dl\uparrow} > D_{terrace}$  and the adatoms prefer upward diffusion to terrace diffusion.





**Fig. 5.7.** Arrhenius representation of both experimental and simulated saturation island densities for  $T_s \leq 245$  K (experimental and simulation conditions:  $\theta = 0.1$  ML, flux =  $3.2 \times 10^{-4}$  ML/s).

Fig. 5.8 shows the diffusion constant  $D = (v_0/4) \exp\{-E_{diff}/kT_s\}$  for upward, downward and terrace diffusion in an Arrhenius representation. The intercept with the abscissa gives the preexponential factor  $v_0$ . This plot illustrates the changing predominant diffusion and rate limiting mechanisms as a function of the temperature:

For  $115 \leq T_s \leq 163$  K, the downward diffusivity is larger than terrace diffusivity ( $D_{dl\downarrow} > D_{terrace}$ ), which is important since otherwise an atom that falls on-top of a dislocation would be able to nucleate with a second atom on-top of a dislocation. Such a behaviour is not observed for  $T_s < 200$  K. An adatom can only cross a dislocation if both the upward and downward diffusion rate are sufficiently high. In this temperature range  $D_{terrace} \gg D_{dl\uparrow}$  and thus the rate limiting process is terrace diffusion (see the bold line in Fig. 5.8).

For  $163 \leq T_s \leq 370$  K upward diffusion is rate limiting and the total energy difference  $\Delta E$  determines the slope fitted to the high temperature regime in Fig. 5.7. For temperatures exceeding 163 K, the rate limiting mechanism for dislocations crossing is

the lower value of the upward or the downward diffusion. As an example, at 200 K, where the change in slope occurs, the predominant diffusion mechanism is downward diffusion, although the upward diffusion is the limiting mechanism.

To reproduce the slope transition in the island density by simulations for the entire regime below 245 K, the choice of parameters is not free:

- The attempt frequency and diffusion barrier ( $\nu_0, E_m$ ) on terraces are pinned down by the slope and absolute values of the island saturation density  $n_x$  for temperatures below 200 K.
- $\Delta E$  is given by the slope for the high temperature range ( $200 \leq T_s \leq 245$  K).
- $\nu_{dl\uparrow}$  is determined by the temperature at which the change of predominant diffusion mechanism occur ( $\approx 200$  K in our case).
- $\nu_{dl\downarrow}$  is determined by the fact that no island nucleate on top of dislocations for temperatures in the 100-245 K range.

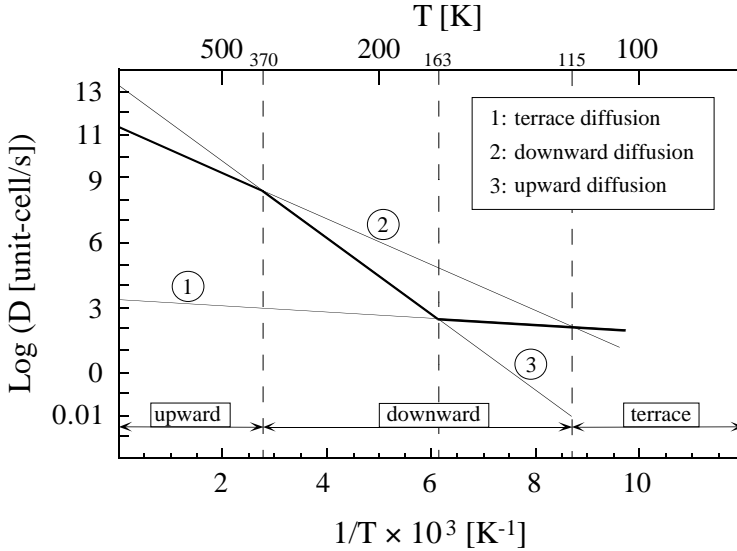


**Fig. 5.8.** Arrhenius representation of the diffusion constant  $D = (\nu_0/4) \exp\{-E_{\text{diff}}/kT_s\}$  for the sets of parameters listed in Table 5.1. The fastest diffusion mechanism is indicated at the bottom for the three temperatures ranges. The bold line represents the rate limiting mechanism for each regime.

## 5.5 Comparison of the $\{E_m, \nu_0\}$ pair for several metal on metal systems.

The parameters characterizing the diffusion of a metal adatom on a metal surface are the activation energy  $E_m$  and the attempt frequency  $\nu_0$ . These parameters can be experimentally determined by several methods. E.g. 1) field emission microscopy [119], 2) measurements of the temperature dependence of the mean square displacement of adatoms by field ion microscopy (FIM) [84, 120] and 3) analysis of the temperature dependence of the island saturation density (see chapter 3) [85]. This section contains a summary of experimental results found in literature for the activation energy and attempt frequency for the diffusion of metal atoms on close packed surfaces. Most results presented here come from variable temperature STM experiments (see chapter 4, 5 and refs. [87, 94, 109, 121] or from FIM measurements [122, 123].

Up to now diffusion barriers obtained from such experiments were all above 100 meV and the corresponding attempt frequencies were close to the "universal" value, i.e. the range of typical phonon frequencies ( $1 \times 10^{12} - 1 \times 10^{13} \text{ s}^{-1}$ ). However, it has been reported recently that for systems with very low diffusion barrier the

	$E_m$ (meV)	$\nu_0$ (s <sup>-1</sup> )	Reference
Al/Au(111)	$30 \pm 5$	$1 \times 10^{3 \pm 1}$	Chapter 5
Al/Al(111)	$42 \pm 4$	$8 \times 10^{6 \pm 0.25}$	Chapter 4
Ag/1MLAg/Pt(111)	$60 \pm 10$	$1 \times 10^{9 \pm 0.6}$	[94]
Ag/Ag(111)	$97 \pm 10$	$2 \times 10^{11 \pm 0.5}$	[94]
Rh/Rh(111)	$160 \pm 20$	$3 \times 10^{11 \pm 1}$	[122]
Ag/Pt(111)	$168 \pm 5$	$3 \times 10^{13 \pm 0.75}$	[121]
Ir/Ir(111)	$267 \pm 4$	$2 \times 10^{11 \pm 0.15}$	[124]
Pt/Pt(111)	$260 \pm 10$	$5 \times 10^{12 \pm 0.5}$	[87]

**Table 5.2.** Diffusion barriers  $E_m$  and attempt frequencies  $\nu_0$  for metal adatoms deposited on fcc close packed surfaces.

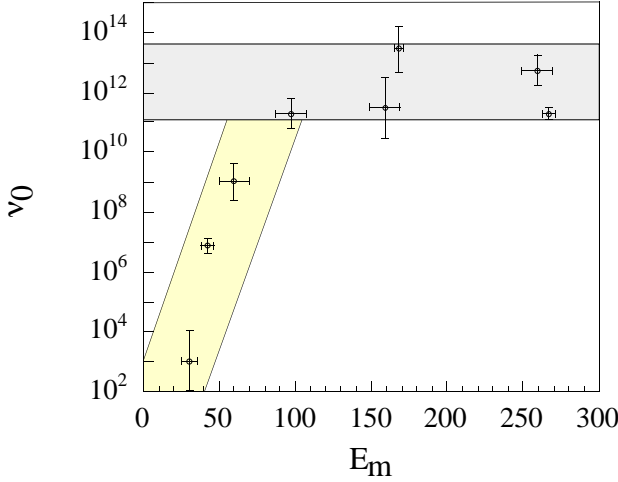


**Fig. 5.9.** Evolution of the attempt frequency  $\nu_0$  versus the diffusion barrier  $E_m$  for the values listed in Table 5.2. For  $E_m < 100$  meV, the attempt frequencies are drastically lowered.

attempt frequency may differ by many orders of magnitude from this universal value. E.g. Brune et al. measured for the diffusion of Ag atoms on a pseudomorphic Ag monolayer on Pt(111) a diffusion barrier of  $60 \pm 10$  meV and an attempt frequency of  $1 \times 10^{9 \pm 0.6} s^{-1}$  [94]. In chapter 4 a diffusion barrier of  $42 \pm 4$  meV and an attempt frequency of  $8 \times 10^{6 \pm 0.25} s^{-1}$  was found for the Al/Al(111) system. In the case of Al in the pseudomorphic areas of the Au(111) reconstructed surface, these values are even lower (see § 5.3). Upon compiling the results for diffusion of metal atoms on close-packed metal surfaces, it turns out that for systems with diffusion barriers below 100 meV, the prefactors systematically decrease with decreasing  $E_m$  (see Table 5.2). The plot in Fig. 5.9 demonstrates this in a clear fashion. So far this surprising behaviour has not been rationalized.

The experimentally observed extremely low attempt frequencies are orders of magnitude lower than the "universal" value and can not be attributed to compensation effects [71, 72]. From theoretical studies using molecular dynamics (MD) another explanation for this behaviour emerges. We have tacitly assumed that diffusion is well described by transition state theory (TST) in terms of jumps over a distance of only one lattice site and with atoms being most of the time at their binding sites giving them

enough time for thermal equilibration with the substrate. However, these assumptions are only valid at temperatures small compared to  $3E_m/k$  [125]. The nucleation experiments are usually carried out at temperatures below 200 K  $\approx 18$  meV and thus should still be described by TST. Nevertheless it is not excluded that the effects predicted by these MD studies set in earlier in reality and that systems with very low diffusion barriers cannot be described within the traditional picture. An alternative explanation is based on repulsive impurities. Repulsive defects, if present on the surface, (e.g. surfactants) may modify the mean free path of diffusing adatoms and thereby lead to a wrong attempt frequency if nucleation theory is applied. However, this effect cannot explain a change in attempt frequency by nearly ten orders of magnitude. This has been confirmed by KMC simulations performed by Liu et al. [126]. In addition for the case of Al/Au(111), the substrate is known to be particularly inert against contaminations.

Recently a theoretical study addressed possible uncertainties in the nucleation mean-field theory. In the following we discuss on the reliability of applying mean-field nucleation theory (see Equation 3.3) to extract parameters for adatom diffusion from nucleation island densities. For this purpose the case of  $i = 1$  (i.e.  $E_i = 0$ ) will be considered, where Equation 3.3 reduces to:

$$n_x \cong \eta(\theta, i) \left( \frac{D}{R} \right)^{-\chi} \quad (5.1)$$

$$\frac{d \log(n_x)}{d(1/T_s)} = -\chi \frac{1}{\ln(10)} \frac{E_m}{k} \quad (5.2)$$

$$\log(n_x(T_s = \infty)) = \log \eta - \chi \log \left( \frac{v_0}{4R} \right) \quad (5.3)$$

Intrinsic uncertainties in Equation 5.1 originate from the exponent  $\chi$  and from the dimensionless factor  $\eta$ . The exponent  $\chi$  is related to the adatom diffusion barrier  $E_m$  by Equation 5.2. In order to get an estimation on the precision of  $\chi$  we consider the example of Pt/Pt(111). For that system the diffusion barrier  $E_m$  has been determined by three different experimental methods, two of which are not based on the nucleation theory. Measurements with FIM yield  $E_m = 0.26 \pm 0.02$  eV [127] and experiments applying KMC to analyze a nucleation curve yield  $E_m = 0.26 \pm 0.01$  eV [87]. Upon analyzing the saturation island densities obtained in ref. [87] by means of Equation 5.1 with  $\chi = 1/3$  one obtains  $E_m = 0.26$  eV, thus proving that  $\chi$  is precise within  $\pm 4\%$  [128].

Uncertainties in  $\eta$  enter into the attempt frequency  $\nu_0$  by Equation 5.3. This factor has been determined by KMC and mean-field rate equations studies. For substrates with square symmetry  $\eta$  was found to be equal to  $\approx 0.25$  for both compact and ramified islands [129]. KMC simulations on hexagonal surfaces, yield  $\eta = 0.25 \pm 0.02$  for coverages  $0.1 < \theta < 0.2$  ML [128]. This value was obtained independent from the detailed island shape, i.e. for dendritic islands as well as for classical DLA-islands with monatomic branches. Finally classical rate theory predicted a value for  $\eta = 0.25 \pm 0.05$  for coverages  $0.1 < \theta < 0.2$  ML (for  $i = 1$ , 2D islands and complete condensation) [112]. Therefore the value  $\eta \approx 0.25$  appears to be reliable within  $\pm 20\%$ . This uncertainty of  $\eta$  translates into an uncertainty for  $\nu_0$  of  $\pm 60\%$ . This consideration implies that the prefactors discussed in this section (see Table 5.1) are reliable to within a factor of two. The observed deviation to smaller prefactors for systems with low diffusion barriers is by orders of magnitudes larger than systematic errors from the analysis.

To summarize, the large difference of the attempt frequency with respect to the "universal" value observed for some metal on metal systems cannot be understood in terms of previously suggested explanations. It has been reported for the Al(111) surface that surface phonons have energies up to 20 meV [74], and thus are comparable to the diffusion barrier. In addition, as the measurements are carried out at temperatures close to the diffusion barrier, it is possible that adatoms are no longer well located and diffuse almost freely on the surface. A description within diffusion theory of liquids is possibly the adequate approach for an appropriate description of such systems. More detailed theoretical considerations are thus in demand for a complete understanding of these low prefactors.

## 5.6 Conclusion

The initial stages of Al epitaxy on the ( $\sqrt{3} \times \sqrt{3}$ ) reconstructed Au(111) surface were studied by variable-temperature STM, serving as model system for the nucleation kinetics on a substrate with a periodic arrangement of dislocations. A detailed analysis of the island densities and sizes as a function of temperature reveals three distinct nucleation regimes. Below 200 K Al adatoms are confined to the pseudomorphic stacking areas. Above 200 K they diffuse over dislocations which constitute considerable repulsive barriers. Intermixing sets in for  $T_s > 220$  K. It is distinguished from pure adatom nucleation by the appearance of a second island size in the scaled island size distribution. Intermixing induces finally a transition from the chevron

reconstruction to a hexagonal domain pattern above 245 K, which is associated with a third nucleation regime (see chapter 6).

In the pseudomorphic stacking areas (terraces) nucleation mean-field theory for isotropic diffusion permits to extract a diffusion barrier of  $E_m = 30 \pm 5$  meV and an attempt frequency of  $\nu_0 = 1 \times 10^{3 \pm 1} \text{ s}^{-1}$ . These values have been confirmed by kinetic Monte-Carlo simulations. The diffusion barriers for crossing the dislocation lines have been estimated by means of simulations that were adopted to the particular symmetry of the Au(111) substrate reconstruction. Barriers of 350 meV for upward diffusion and 210 meV for downward diffusion with corresponding attempt frequencies, resulting in an effective barrier for crossing the reconstruction domain wall of 560 meV were found.

## Chapter 6

# Growth and surface alloying of Al on Au(111) at room temperature

### 6.1 Introduction

STM measurements provide crucial information on the atomic scale properties of the film structure and the growth kinetics. Local information is of particular importance when reconstructed substrates are studied, whose inherent defects can determine nucleation and growth of adlayers. This was demonstrated for instance for the growth of Ni and Co on Au(111), where the Au(111) surface reconstruction [11, 78, 130, 131] stabilizes regular island patterns in the initial stages of thin film growth [96, 100]. On the other hand it has been demonstrated that a substrate reconstruction itself can be modified due to the activity of adsorbed metal atoms, which can drive both reconstruction phase transformations [132] or surface intermixing [133, 134]. In a number of cases it has been shown that elements intermix at the surface although they are immiscible in the bulk [15, 16]. The driving force for the so called surface alloying is the reduction of the strain energy related to the atomic size mismatch of the two constituents [17]. Moreover, in systems which are known to form stable bulk alloys, the kinetics of surface mixing turned out to be important, as the nucleation kinetics in the initial stages of growth is substantially altered with respect to systems growing phase separated [18].



In this chapter we present an STM study of the growth and alloying of Al on Au(111) at 300 K. These metals are known to be miscible in the bulk. While the bulk lattice parameters of the two fcc metals are almost identical (4.08 Å and 4.04 Å for Au and Al, respectively), the surface free energy of Al ( $\approx 1200 \text{ mJ/m}^2$ ) is significantly lower than that of Au ( $\approx 1550 \text{ mJ/m}^2$ ) [135, 136]. Based on the small lattice mismatch and the negative surface energy balance, pseudomorphic layer-by-layer growth might be expected from simple thermodynamics [36]. However, the Au(111) surface layer is uniaxially contracted along the close-packed lattice directions corresponding to a reduction of the surface lattice parameter of 4 % along the contraction directions. Recently, it has been shown, that epitaxial growth can be sensitively influenced by the strain field present in the surface layer of the substrate [137]. Indeed, helium diffraction measurements for the Al/Au(111) system revealed a complex temperature dependent growth behavior [102]. In addition, a symmetry change of the Au(111) reconstruction diffraction pattern was observed for Al deposition at temperatures exceeding 230 K, which was interpreted as an Al induced Au reconstruction [102]. It will be demonstrated here that the complex nucleation and growth behavior above 230 K is related to Al intermixing into the topmost Au layer. Already minute quantities of incorporated Al strongly perturb the chevron reconstruction of the clean surface. The intermixing substantially affects the nucleation kinetics in the submonolayer coverage range resulting in an unusual bimodal island size distribution.

## 6.2 Island and thin film morphology

The gross features of the initial stages of epitaxial growth of Al on the Au(111) surface at 310 K are illustrated by the STM data reproduced in Fig. 6.1. At  $\theta_{\text{Al}} \approx 0.1 \text{ ML}$  (Fig. 6.1a) large islands with monolayer height (2.4 Å) and dendritic shape are found in the large terraces. The shape of the islands is related to a kinetic effect associated with anisotropic diffusion around island corners. As revealed in detail for dendritic growth of Ag islands on various fcc(111) substrates [66] atoms arriving at one-fold coordinated corner sites preferentially diffuse towards  $\{100\}$  steps thus promoting trigonal growth in the  $[\bar{1}\bar{1}2]$  directions. The distances in between the islands are of the order of 1000 Å; hence the atoms built in the islands must have diffused over several hundred Ångströms on the surface in the process of island formation. Dendritic growth of fingerlike islands is similarly observed along the step edges of the Au

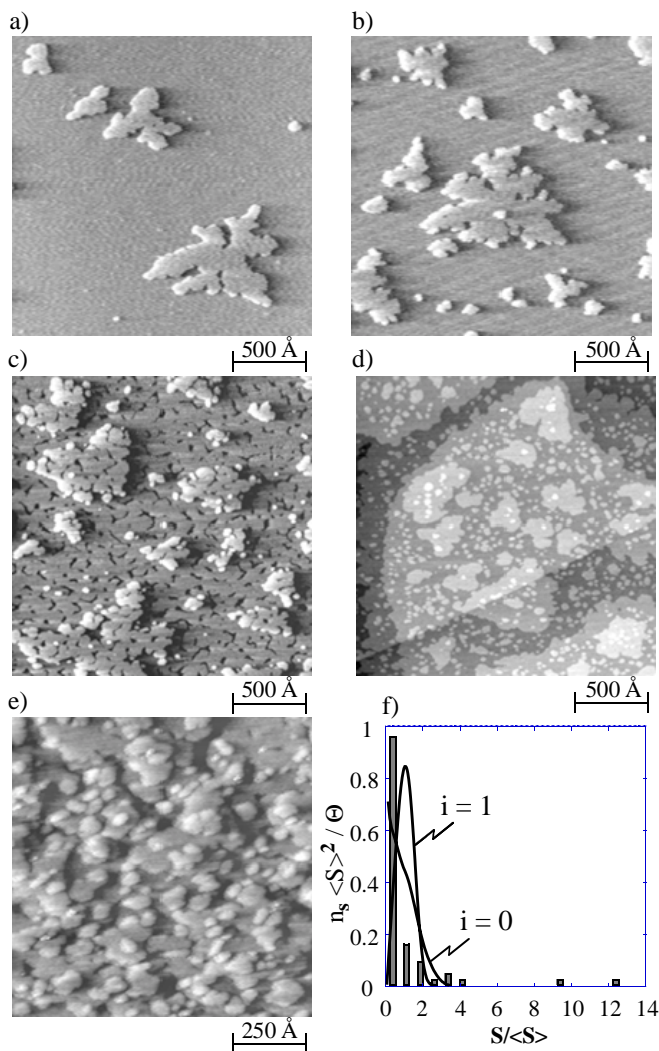


**Fig. 6.1.** Morphology of the Au(111) surface with Al deposited at 310 K (Al flux 0.05 ML/min): (a)  $\theta_{Al} \approx 0.1$  ML; (b)  $\theta_{Al} \approx 0.2$  ML; (c)  $\theta_{Al} \approx 1.2$  ML; (d)  $\theta_{Al} \approx 1.6$  ML; (e)  $\theta_{Al} \approx 4.8$  ML; (f) bimodal island size distribution at  $\approx 0.2$  ML coverage ( $S$  ( $\langle S \rangle$ ) island (mean island) size;  $n_s$ : island density,  $\theta$ : coverage).

substrate. With increasing coverages a bimodal island size distribution evolves. This is demonstrated by the plot in Fig. 6.1f, where a statistical analysis of the island size distribution at about quarter monolayer coverage is reproduced. For this analysis a series of STM images ( $5000 \times 5000 \text{ \AA}^2$  in size) have been evaluated quantitatively, revealing that a small number of very large islands coexist with many small islands. In contrast to a regular nucleation and growth scenario on a homogenous surface, where a distribution for the scaled island density with a pronounced single maximum is expected [47, 48, 138], for the present system there is a clear deviation from this behavior. For comparison, calculated scaled island size distributions using the analytical expressions from ref. [47] for a critical island size  $i = 0$  and  $i = 1$  are included in the plot in Fig. 6.1f (note that the curves for  $i = 2$  and  $i = 3$  are similar to  $i = 1$ ; for clarity they are not shown).

For the present system three distinct regimes in the scaled island size distribution exist: for  $S/\langle S \rangle < 4$ , the scaled island size distribution resembles to the curve expected for the model case  $i = 0$ . For intermediate and very large values, both calculated and experimental probabilities in the scaled island size distributions are zero. However, in sharp contrast to usual nucleation models, where the probability remains zero for all sizes with  $S/\langle S \rangle$  exceeding 4, a second class of islands is clearly discernible in the experimental data for  $S/\langle S \rangle$  between 9 and 12. The coexistence of these two classes of island sizes, i.e., the bimodal nature of the island size distribution, is understood as the result of a nontrivial growth mode prevailing for growth of Al on Au(111). The course of the scaled island size distributions of small islands signals that nucleation with a critical cluster size of 0 is of importance for the present system. This indicates the possibility of nucleation due to exchange processes between adsorbate and substrate atoms, similar to findings for the Fe/Cu(001) system [139].

Small second layer islands are formed already at  $\theta_{\text{Al}} \approx 0.3 \text{ ML}$  on the largest islands of the first layer. For  $\theta_{\text{Al}} \approx 1.0 \text{ ML}$  percolation of the first layer islands and formation of larger second layer islands is observed. With increasing Al coverage the completion of the first layer proceeds while on the largest second layer islands already the occupation of the third layer sets in (Fig. 6.1c for  $\theta_{\text{Al}} \approx 1.2 \text{ ML}$ ). Once the first monolayer is completed, a density of second layer islands much higher than that of the first layer is observed, as obvious from the tunneling image in Fig. 6.1d. This indicates that the mobility of the atoms on the first layer is much smaller than that on the clean substrate surface. For higher coverages the density of islands on the surface shrinks again and films with simultaneous occupation of several Al layers are formed, as

demonstrated by the STM image in Fig. 6.1e, where the surface morphology of an 4.8 ML Al film is reproduced.

The data reproduced in Fig. 6.1 demonstrate, that the defects of the Au(111) chevron reconstruction do not simply act as nucleation centers for the deposited Al atoms, in which case regular island arrays would be formed. The unusual bimodal island distribution also indicates that the growth scenario for Al/Au(111) is dissimilar from heteroepitaxial growth on an unreconstructed metal substrate with trigonal symmetry.

### 6.3 Al–Au surface alloy formation

STM data on a smaller scale and with higher resolution demonstrate accordingly that the system is more complex and that the Au(111) substrate reconstruction reacts sensitively upon Al deposition. For coverages as low as a few percent (deposited at  $T_s = 300 - 350$  K), the Au(111) chevron structure is lifted and a highly distorted reconstruction domain pattern evolves. This is demonstrated by the tunneling image in Fig. 6.2 for  $\theta_{\text{Al}} \approx 0.04$  ML. In the terraces small islands are resolved (corrugation amplitude  $\approx 2.4$  Å, corresponding to the Au(111) monostep height). The reconstruction deformation induced by the deposited Al on the substrate resembles patterns found on the clean surface in the vicinity of defects [11, 108]. The basic features of the  $(\sqrt{3} \times 22)$  domain structure are preserved: the light, pairwise corrugation lines (amplitude  $\approx 0.2$  Å) correspond to areas where surface atoms reside on bridge positions of the second layer, separating fcc and hcp stacking type domains. The fcc domains correspond to the wider areas between parallel running stripes [11]. It should be noted that the atoms in these areas do not reside on ideal fcc or hcp stacking type positions, as observed both for Au(111) [11] and isostructural features of the metastable Pt(111) reconstruction [140]. Rather, the surface layer is uniformly contracted along the close-packed directions and thus the observed fcc-hcp transitions are not to be understood in a strictly crystallographic sense. For coverages exceeding  $\approx 0.1$  ML, the number of islands increases and a new poorly ordered surface reconstruction with hexagonal symmetry is formed. Upon Al adsorption at 300 K this new reconstruction evolves exclusively in the terraces, whereas the islands exhibit a high defect density. For deposition at higher temperatures or upon gently annealing, however, the entire surface, including the islands, exhibits this reconstruction pattern, as illustrated by the STM image in Fig. 6.3. (Note, that the islands formed upon annealing to 450 K are more compact than those in the data of islands formed at 300 K in Fig. 6.1, due to the increased surface atom mobilities at higher temperature. Because of the larger scales

and the lower resolution of the low coverage STM data in Fig. 6.1, the existing reconstruction patterns are not resolved there.) This reconstruction closely

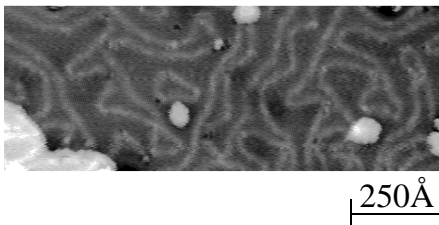


**Fig. 6.2.** Strongly perturbed Au(111) reconstruction pattern formed upon deposition of 0.04 ML Al at 300 K

resembles the Na induced distorted hexagonal (DHEX) phase on Au(111) [132], which again is believed to be isostructural with the high temperature phase of the Au reconstruction [130]. Thus the explanation originally proposed for this phase is expected to be applicable also in the present case. The pattern formed is rationalized as a domain structure: the dark triangular areas are associated with fcc and hcp stacking domains and the light corrugation stripes with transition regions, where surface atoms reside on bridge type positions on the second layer and consequently are imaged higher (see inset in Fig. 6.3). A schematic ball model illustrating the situation is reproduced in Fig. 6.4 In the spots, where six stripes meet, surface atoms reside on or near top positions of the second layer and accordingly are imaged in the STM topographs with an increased corrugation amplitude [132, 140]. As with the clean surface, the assignment of the stacking domains is qualitative, and it is likely, that the contraction of the surface layer is rather uniform and not strictly localized in the corrugation lines.

The fact that the structural transformation exists on the entire surface rules out the possibility of an Al-induced Au reconstruction for the hexagonal pattern, for which pure Al islands with different structural features were expected. A phase separation of Al and Au within the surface layer corresponding to the observed features can be ruled out because of the wide Al coverage range for which the same hexagonal structure is

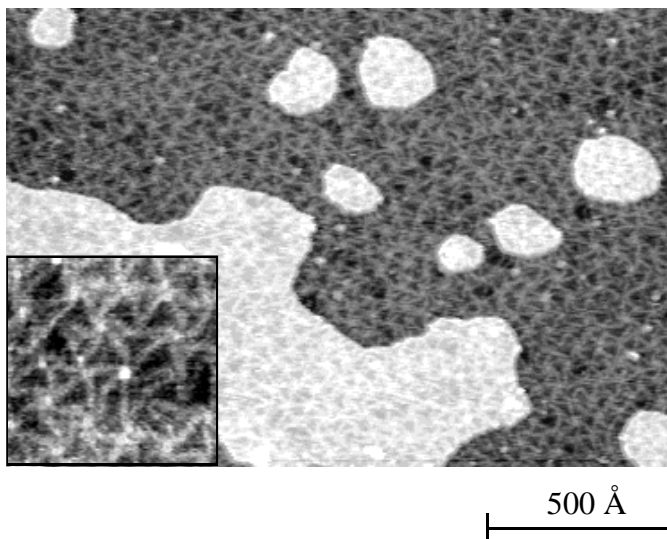


**Fig. 6.3.** Distorted hexagonal reconstruction pattern of an intermixed Al–Au surface layer in terraces and on islands, formed upon deposition of 0.2 ML Al on Au(111) at 350 K and annealing to 450 K. Inset:  $300 \times 300 \text{ Å}^2$  blow-up of the reconstruction pattern.

observed [102] and the strong tendency towards alloy formation of the two metals. Consequently the surface must consist of an intermixed Al–Au surface layer which relaxes in the observed domain structure. For the Al–Au system a rich variety of binary alloy phases exist [141–143] and thus the formation of a surface Al–Au alloy layer is not surprising. We could not obtain atomic resolution images, which would allow for an analysis of the atomic structure of the surface. However, with regard of the fact, that Al and Au intermix easily for many stoichiometries in the bulk alloys, a homogeneous intermixing of Al and Au in the surface layer can be expected. This is in accordance with STM observations of Ag–Cu alloy thin films on Ru(0001), where a strain stabilized two dimensional alloy with a related domain structure was observed [144].

In accordance with the He diffraction results [102], we found that the Au(111) chevron reconstruction is preserved for deposition temperatures below 230 K (See chapter 5.3). The Al–Au DHEX evolves for  $T_s > 230 \text{ K}$  indicating that exchange of Al and Au atoms in the surface layer are possible well below room temperature. This finding is in agreement with results for the Pd on Au(111) system, where the onset of

surface alloy formation was observed at temperatures exceeding 240 K [145], very similar to the present system. For the Na/Au(111) system an even lower threshold temperature of  $\approx 200$  K for the formation of intermixed Na-Au surface layers was observed [134].

The Al-Au surface atom exchange processes are understood as the reason for the unusual bimodal island size distribution observed for submonolayer coverages upon Al deposition at 310 K. While our data do not allow for a quantitative analysis of the island formation process, its main features can be rationalized as follows: The coexistence of many small and few large islands indicate distinct processes for island nucleation with coverage or time dependent efficacy. Low temperature STM experiments revealed that the bimodal distribution occurs only for temperatures exceeding the critical temperature for surface atom exchange (See chapter 5.3). Hence the large islands, which according to their size are formed initially, are associated with nucleation at sites where atom exchange can occur. STM experiments employing other deposits on Au(111) indicate, that nucleation is initiated indeed by replacement of Au atoms at defect sites of the reconstruction [18]. We believe that such a mechanism is effective also in the present system and that the large islands nucleate in the early stages of deposition, where the density of monomers increases linearly with coverage ('transient regime' [91]). In the beginning of this regime, the mean free path of the atoms is large, which allows for rapid growth of these islands. However, with continuing deposition on the one hand the monomer density increases implying a higher probability for adatom nucleation in the terraces without exchange processes. On the other hand, the chevron reconstruction is heavily distorted once a small Al coverage has built up, which also might lead to a significant reduction of the mean free path of the atoms or an increased density of nucleation sites on the surface due to restructuring. The resemblance of the island distribution in Fig. 6.1f to the curve expected for  $i = 0$  suggests that due to the reconstruction changes surface atom exchange processes leading to island nucleation might be facilitated [139] (for a comprehensive analysis of the temperature dependent growth behavior of Al on Au(111) see chapter 5).

The periodicity of the Al-Au DHEX phase is  $55 - 60 \text{ \AA}$  for an Al coverage of 0.1 to 0.2 ML, which is in good agreement with that derived from He diffraction data ( $52 \text{ \AA}$  for Al coverages of 0.1 - 0.5 ML deposited at 300 K [110]). From this periodicity a contraction of the surface layer of 10 % is inferred, i.e., the surface atom density amounts to 1.10 ML. This estimate is based on the model shown above

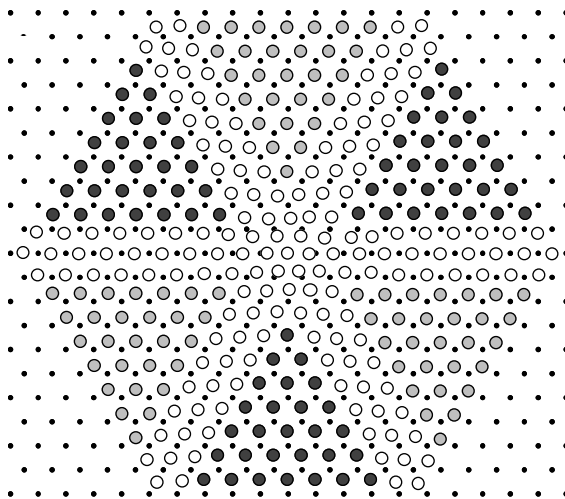


**Fig. 6.4.** Ball model for the Al–Au surface alloy domain structure. White (grey, dark): surface Al or Au atoms close to bridge–top (hcp, fcc) type stacking positions. Black spots symbolize Au atoms of the second layer.

(Fig. 6.4), where the surface atom density is given by the simple expression:  $[(1/a + 1)/(l/a)]^2$  ( $a$  is the lattice parameter of a (111) Au bulk plane: 2.885 Å, and  $l$  corresponds to the periodicity of the DHEX phase). The He diffraction data demonstrate, that for Al coverages exceeding 0.5 ML the surface periodicity of the Au–Al DHEX further shrinks to reach a value as low as 30 Å close to monolayer coverage [110], which corresponds to an even higher surface atom density of  $\approx 1.20$  ML. The surface atom density of this phase is thus significantly higher than that of the Na-induced DHEX (1.06 - 1.09 ML [132]) or that of the isostructural Au(111) high temperature phase (1.07 ML [130]). The formation of the latter structures was associated with a reduced coupling of the surface to the second Au layer which allows for a more uniform contraction of the surface Au layer [132]. The contraction of the Al–Au DHEX layer is thus unexpectedly large in view of the similar atomic radii of Al and Au. However, for Al–Au bulk binary alloys (and other binary alloys of Al with transition metals) it is well known that large negative deviations from the additivity of the atomic volumes exist, i.e., the Al atomic volume in certain alloys is considerably smaller than that in the fcc Al crystal [146, 147]. The observed high contraction of the Al–Au surface alloy layer is thus rationalized as the



two-dimensional analogue of the Al atom contraction in such binary bulk alloys. If we assume that the atomic radius of the Au atoms in the intermixed layer corresponds to that of the high temperature DHEX reconstruction phase, they occupy a surface area of  $0.806 \text{ \AA}^2/\text{atom}$  [130]. With this value and the known contraction of the Al-Au surface layer, the average surface area occupied by the Al atoms for a coverage of 0.2 ML is estimated to  $0.711 \text{ \AA}^2/\text{atom}$ , which is only 84 % of the area of Al atoms in the (111) Al bulk plane, corresponding to a reduction of the Al atomic radii by  $\approx 8 \%$ . For intermetallic fcc type Al Au compounds, the Al atomic volume contraction amounts up to 10 % (corresponding to a 3 % radial contraction), indicating that the contractions in surface alloy formation can be stronger than those in the bulk. The driving force for the formation of the Al-Au DHEX structure is thus understood as a combination of (1) surface strain, (2) energy gain by surface alloy formation, and (3) reduction of the Al atomic diameter. The results demonstrate in particular, that changes of atom diameters must be considered, when surface alloys of transition metals with Al (and presumably other free electron metals) are formed. Similar surface alloy domain structures are thus expected for Al/Ni, Al/Pd, Al/Pt and other systems, where also large metallurgical compressions for the respective bulk alloys exist [146, 147]. The contraction of the Al atoms is associated with the fact that Al is a nearly free electron metal, which allows for effective charge transfer of aluminium atoms in the Au lattice. Analogous atom contractions are typical for bulk alloy formation of the free electron alkali metals with Au and were observed in surface alloy formation of Na on Au(111) [134].

## 6.4 Conclusion

With the above findings of reconstruction changes and surface intermixing the growth of Al on Au(111) at  $T_s = 300 - 350 \text{ K}$ , whose gross features are presented in Fig. 6.1, can be described as follows: Initially, for Al coverages of the order of a few percent, the chevron reconstruction of clean Au(111) is heavily distorted and small islands are formed. For Al coverages exceeding  $\approx 0.1 \text{ ML}$ , intermixing of Al and Au at the surface definitely exists. Islands are formed in the terraces which must consist of both adsorbed Al atoms and Au atoms released in exchange processes in the terraces. Surface atom exchange processes also lead to an unusual bimodal island size distribution. The surface intermixing finally drives a phase transformation of the Au(111) chevron reconstruction to a poorly ordered surface alloy domain structure, which is of a similar type as the Na-induced or high temperature DHEX phase of the

Au(111) reconstruction. The surface layer of this phase is even stronger contracted than that of the respective Au reconstructions, which is understood as a result of Al atom contraction in the surface alloy layer. The intermixing proceeds with increasing Al coverages until monolayer coverage is reached. For even higher coverages the growth mode changes and a high density of islands is found (cf. Fig. 6.1d). The formation of these islands is associated with the termination of surface alloy formation and Al island nucleation at the defects of the Al-Au DHEX surface. For even thicker films accordingly a reduced density of islands and growth of defect free (111) Al films is observed, where several surface Al layers are occupied simultaneously.



## Chapter 7

# Strain relief in submonolayer islands of Cu on Ni(100)

### 7.1 Introduction

In heteroepitaxial growth, strain due to the misfit between substrate and adlayer is of fundamental importance [82]. The minimization of the associated strain energy can result in defect structures of the adlayer which are very stable and might even appear at submonolayer coverages. In this chapter we discuss the effects of strain in the very initial phase of thin film formation for the particular case of Cu on Ni(100). This system exhibits a positive lattice misfit of 2.6% (compressive strain, Cu lattice constant: 3.61 Å, Ni lattice constant: 3.52 Å). Both metals crystalize in the fcc structure and no reconstruction is observed on the Ni(100) surface. Cu grows on Ni(100) in the layer by layer mode and no intermixing is observed for temperatures below 400 K.

It will be shown that the effect of strain in the present system drives an island shape transition: ramification of initially compact shape sets in as soon as their size exceeds a critical value of about 480 atoms. Island ramification on a close-packed fcc substrate is possible and well understood since kinetic limitations can prevent the realization of the compact equilibrium shape. The symmetry of the fcc(111) surface plays a crucial rôle in this process, since it provides the possibility to reach sites with higher coordination by a single atom movement from a corner site to an edge. The anisotropy of this movement with respect to the two different types of atomic steps may result in distinct growth directions (see Fig. 7.1). The situation is quite different for the quadratic symmetry of the fcc(100) surface, as illustrated by the model in Fig. 7.1. Due

to the substrate geometry there is no direct next-neighbor lateral binding at the island corner site and in addition, atoms arriving there face an equal choice for two diffusion processes towards similar island edges. Furthermore, once the atom is bound to the island edge, its only chance to find an energetically favorable site with higher coordination is diffusion to a kink site. Energetically favorable sites can usually not be reached by a single atom hop. From this it was inferred that in epitaxial growth on an fcc(100) square substrate a sharp transition between two growth regimes should prevail [148]: (i) at the lowest temperatures, where edge mobilities are possibly suppressed, fractal islands might form; (ii) if the temperature is high enough to allow for motions along the edge, compact islands should immediately evolve, since atoms at the edges remain mobile until the more stable kink sites are reached. So far these ideas seem to agree with experimental evidence and exclusively compact islands have

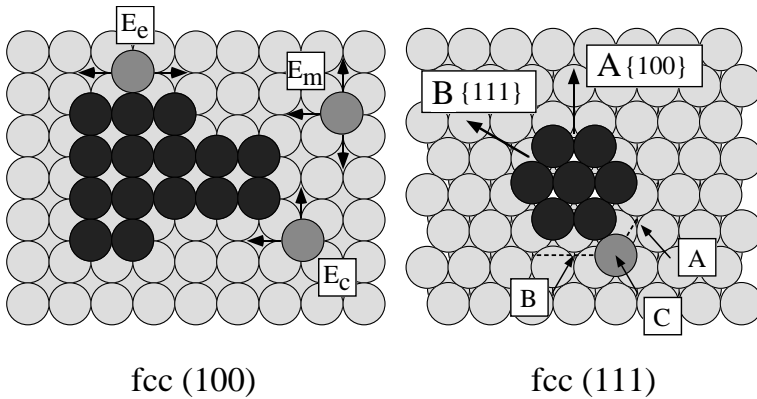


**Fig. 7.1.** Ball models for fcc (100) and (111) surfaces. On the fcc(100) surface the only chance for an edge diffusing atom to find an energetically favorable site with higher coordination is diffusion to a kink site. Such a site can usually not be reached by a single atom hop. The fcc(111) surface provides the possibility to reach sites with higher coordination by a single atom movement from a corner site to an edge. Note that on this surface diffusion towards A-step or B-step are not equivalent. The diffusion processes with the lowest barriers are that from a corner (C) via the hcp-site next to it to an A-step.

been observed in metal epitaxial growth on square substrates (e.g., [62, 149, 150]). In more recent publications it was even pointed out that on square lattices, the barrier for

edge diffusion is usually comparable or lower than for terrace diffusion and the fabrication of dendritic and fractal islands is thus completely inhibited [151, 152]. Hence, lattices with a square symmetry are particularly suitable for the study of strain effects on island shapes since strained epitaxial islands are expected to be unstable against shape changes [153-155]. Analyzing the relation between strain energy and island shape in heteroepitaxial growth, Tersoff and Tromp [156] predicted a spontaneous shape transition during growth for coherently strained islands. These shape changes were considered to be a major mechanism of strain relief. But up to now, experimental evidence for strain-induced island shape transitions is rather scarce. Here, we present the first experimental verification of such a shape transition in growth of monolayer-high islands. Submonolayer growth experiments performed between 250 and 370 K reveal that small islands exhibit the expected compact shape, whereas larger islands (exceeding a critical size of  $\approx 480$  atoms) become ramified. This island size dependent shape transition is quantitatively treated in this chapter.

With increasing coverage, i.e. with increasing strain at large islands, a second strain relief mechanism dominates over island ramification as the latter is no longer sufficient [157, 158]. In the submonolayer range for coverages exceeding about 0.25 ML (as soon as the compact part of the islands reaches a critical size of 1200 atoms), long protruding stripes traversing entire islands appear with a typical length of 60–80 Å, an imaging height of about 0.6 Å, and a width of  $\approx 6$  Å, which is the typical STM-imaging width of single atoms [159]. At a coverage of about 1 ML (see Fig. 7.2) the entire surface is covered by a network of stripes. The stripes have identical widths and are all running along  $\langle 110 \rangle$  directions with an equal probability for the two orthogonal domains. This pattern is maintained up to coverages of about 20 ML. Only the width of the stripes grows linearly with the coverage, whereas their density and average length remain constant. The stripes do not cross each other or coalesce. The internal  $\langle 111 \rangle$  faceting is a simple model which accounts for the experimental observations (Fig. 7.2). It is motivated by the fact that the compressive strain at the fcc (100) surface is maximal in the close-packed  $\langle 110 \rangle$  direction.

Therefore, intuitively it could be expected that chains of atoms are squeezed out from the adlayer and create protruding stripes. Due to the square symmetry, these stripes are expected with equal probability in both  $\langle 110 \rangle$  directions, perpendicular and parallel to the substrate step edges. The simplest way to generate such stripes is to shift

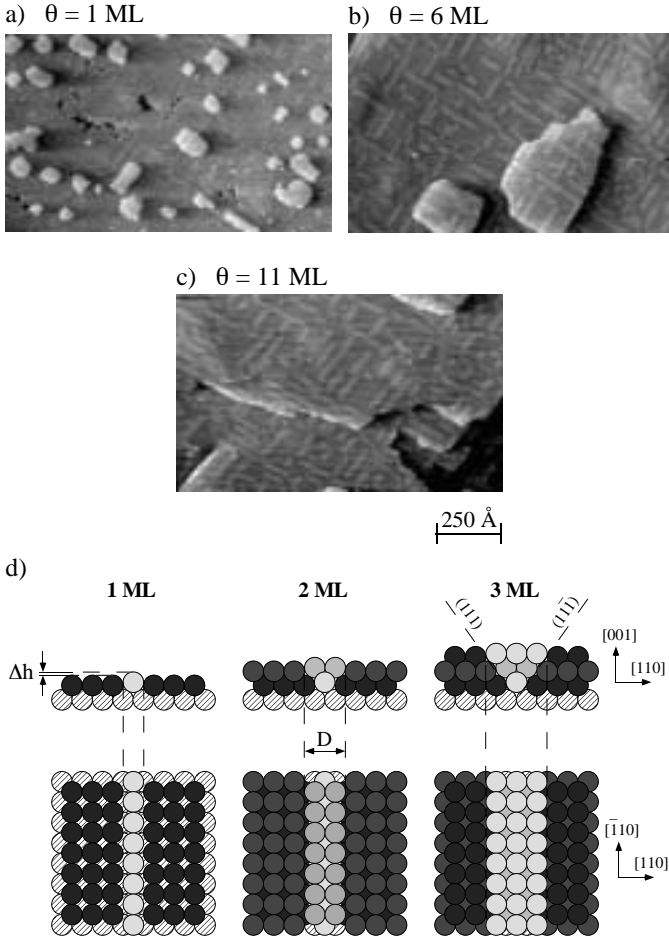


**Fig. 7.2.** STM images of copper islands on Ni(100) for 1, 6 and 11 ML; a), b) and c) grown at 350 K with a rate of  $1.5 \times 10^{-4}$  ML/s. d) Internal faceting model describing the appearance of the protruding stripes. The figure shows the side view and the top view for coverages of 1, 2 and 3 ML. The shaded circles represent the substrate atom (nickel). The dark circles (copper) are placed at the 4-fold hollow sites in the pseudomorphic geometry. The light circles (copper) form the stripes and are placed at the 2-fold bridge sites in the first layer. As indicated for 3 ML coverage, (111) facets are formed along the stripes.

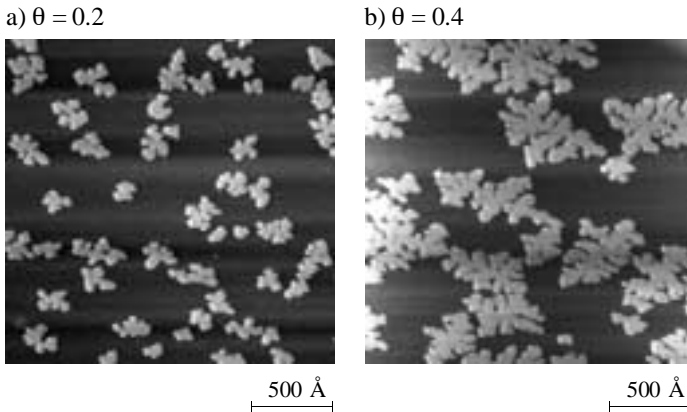
Cu atoms from their fourfold hollow site to the twofold bridge site. Such a bridge-site atom has a reduced number of nearest neighbors to the substrate but increases the binding energy in the adlayer. There are two nearest neighbors below and, in addition, four lateral neighbors with a binding length which is increased only about 10% (neglecting relaxations). More important, the protruding atoms gain the lateral freedom to expand and the film can partially relieve its strain, which is the driving force for stripe formation. Obviously, this lateral freedom of expansion overbalances the lowered binding energy. The stripes only disappear if the sample is annealed above 550 K. We have observed both a reduction in stripe width as well as a reduction in stripe density, before they finally disappear, due to surface alloy formation. This Cu–Ni intermixing is thus another efficient way for the system to relieve its strain.

Recent X-rays scattering measurements substantiate the internal facetting model [160]. They reveal, in addition, a surprising strain distribution inside the (111) facets. At the bottom of the facet there is a significant lateral relaxation (7%) perpendicular to the stripe orientation using almost the entire extra space made available by the out of plane displacement of the facet. With increasing distances from the interface the relaxation decreases and for a coverage approaching 20 ML the lateral lattice parameter of the topmost layer is close to that of bulk Ni both parallel and perpendicular to the stripe orientation. For low coverages it is thus energetically favorable for the system to create internal facets to relieve its strain, however, with increasing coverages the initially gained strain relief is lost. This provokes an abrupt change of growth morphology, which is expected at approximately 20 ML coverage [160]. This is in agreement with our STM observations which reveal the formation of a dislocation network at coverages exceeding 20 ML.

## 7.2 Characterization of the island shape transition

For the quantitative analysis of the island shapes we have only used images, where the thermal drift was negligible. Drift correction was therefore not necessary. The influence of structural defects such as substrate steps has been excluded by depicting areas far away from such defects. We can definitely exclude that the observed shape transition is due to coalescence but there may be very few large islands, especially grown at low substrate temperatures (high island densities) which may be affected by coalescence. Copper forms two-dimensional islands of monolayer-height on Ni(100)

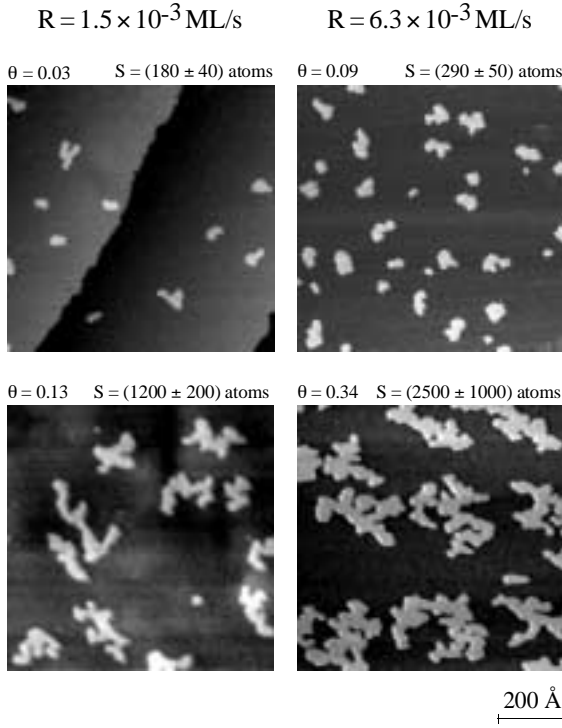




[48]. Examples of monatomic-high islands which clearly show an

**Fig. 7.3.** Ramified island growth in submonolayer heteroepitaxy for Cu/Ni(100). The substrate temperature of 350 K and the deposition rate of  $1.5 \times 10^{-4}$  ML/s indicate that the island shape is not determined by the growth kinetics

irregular shape are shown in Fig. 7.3. As already pointed out in the introduction, it is surprising to find ramified islands on a square lattice. At the employed growth conditions (substrate temperatures between 250 and 350 K!) the adsorbed copper atoms are very mobile on terraces and at step edges (quantitative data see below). This temperature range even includes a transition in critical nucleus from  $i = 1$  to  $i = 3$  (see Fig. 7.12) [48] associated with dimer bond breaking. It can be thus assumed that the ramified copper islands on Ni(100) are not of kinetic origin. In order to confirm this assumption, we have systematically varied the substrate temperature and the deposition rate. A qualitative comparison for different growth conditions is given in Figures 7.4 and 7.5. The images on the left hand side are obtained at high substrate temperature/low growth rate and exhibit therefore a low island density, whereas the images on the right which are obtained at low temperature/high growth rate show a higher island density. The island shapes, however, depend only on the average island size and are not affected by the growth conditions. Small islands are always compact, whereas islands larger than the critical island size of about 500 atoms are ramified and, very large islands even exhibit a preferential arm width of about 20 atoms. The step edges of the islands are



preferentially oriented parallel or perpendicular to the substrate steps in the close-packed  $\langle 110 \rangle$  directions.

**Fig. 7.4.** The transition from compact to ramified island shapes at two different deposition rates ( $1.5$  and  $6.3 \times 10^{-3} \text{ ML/s}$ ) and a fixed substrate temperature of  $345 \text{ K}$ . The coverages and the mean island sizes are indicated in respective figures.

The proposed mechanism of relaxation driven island shape transition is substantiated by additional STM observations, where the surface was annealed above the critical temperature for surface alloy formation ( $T_s$  exceeding approximately  $400 \text{ K}$ ). The data presented in Fig. 7.6 demonstrate that upon intermixing of substrate and adislands previously ramified structures are transformed to compact islands (For this experiment a temperature was chosen, where the islands are not yet dissolved, but

exchange processes between Cu islands and the Ni substrate occur). The effect of

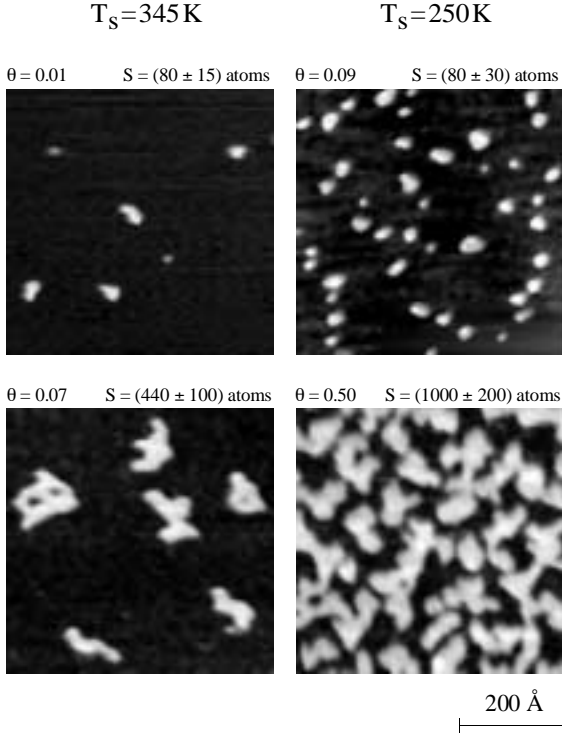


**Fig. 7.5.** The transition from compact to ramified island shapes at two different substrate temperatures (250 and 345 K) and a fixed deposition rate ( $1.5 \times 10^{-3} \text{ ML/s}$ ). The coverages and the mean island sizes are indicated.

intermixing can be seen most easily at the step edges, which are straightened and whose rims are imaged higher and spotted. The rims are not well separated from the Ni substrate and a rather irregular interface is formed. The islands are imaged with the same height and exhibit a similar spotted surface and hence consist also of randomly mixed Ni and Cu. Since the incorporated Ni atoms are smaller, the strain energy of the islands is significantly reduced [161] and consequently compact islands form (comprising up to  $\approx 1000$  atoms in the data shown).

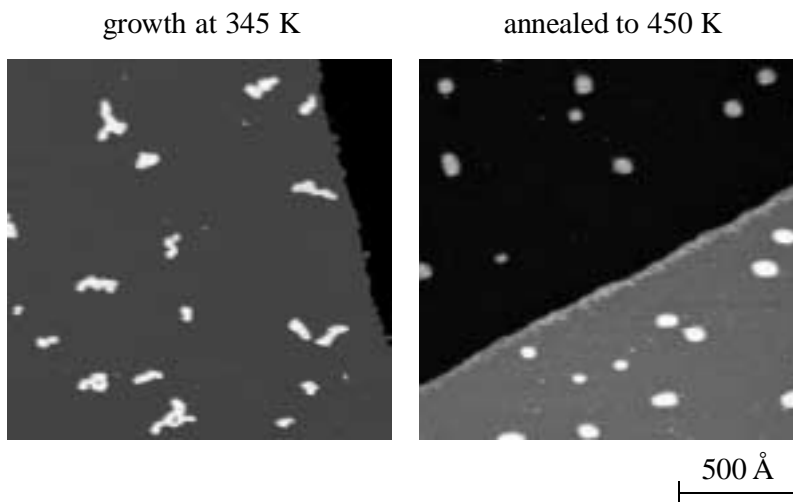


**Fig. 7.6.** STM images of copper islands on Ni(100) before and after annealing to 450 K, demonstrating the effect of surface alloying on the island and step shape. (growth temperature 345 K, deposition rate  $6.3 \times 10^{-4}$  ML/s, coverage 0.04 ML).

### 7.3 Quantitative analysis of the island shape transition

The independence of the island shape from the growth conditions is confirmed by the quantitative analysis of the topography of more than 3000 islands grown at very different substrate temperatures (250 - 350 K) and deposition rates ( $6 \times 10^{-5}$  -  $3 \times 10^{-2}$  ML/s). Indeed, all data collapse into one curve if one determines, e. g. the islands' radius of gyration vs. island size (see Fig. 7.7) or the island perimeter vs. island size (see Fig. 7.8). The evaluation of the radius of gyration vs. island size, varied over four orders of magnitude, reveals a fractal dimension close to 2 ( $D = 1.9$ ). This rather compact structure of the islands can be qualitatively recognized in the images of Fig. 7.3 - even for very large islands, the arms are only separated by narrow channels. This substantiates the previous statement that the island ramification cannot be understood in terms of a fractal growth mode of kinetic origin.

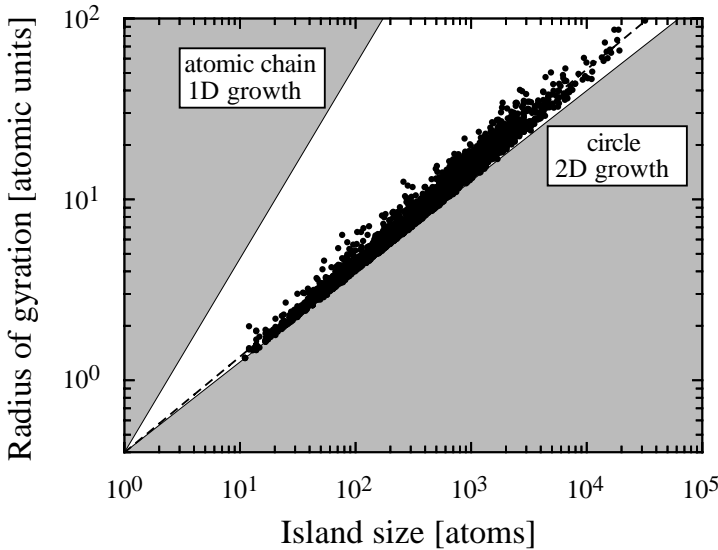
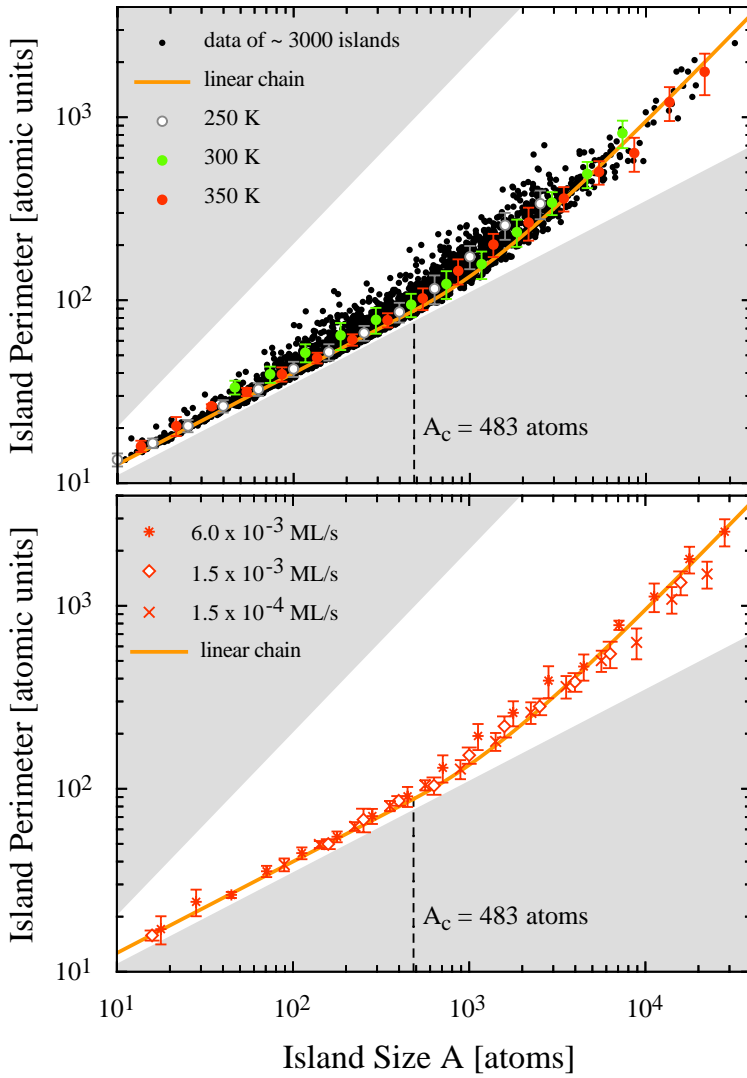


**Fig. 7.7.** Double logarithmic plot of the islands' radius of gyration versus island size. Each dot represents one island. The forbidden regions are gray colored; the upper limit is given by a one atom wide chain; the lower limit is an island of circular shape.

The evaluation of the island perimeter ( $p$ ) as a function of island size ( $A$ ) is more helpful to gain insight into the physics behind the island shape transition. Figure 7.8a shows as double logarithmic plot the complete experimental data set as well as its classification for three different temperatures. It is obvious that independent of the temperature the data collapse in one curve. In the lower part of the Fig. 7.8b

**Fig. 7.8.** (next page) Island perimeter  $p$  vs. island size  $A$  for submonolayer copper islands on Ni(100) demonstrating the coincidence of data obtained at different growth conditions: (a) for three temperatures. The gray shaded areas are the forbidden regions for the ratios, its upper limit corresponds to that of circular islands and the lower limit to that of a one atom wide chain. (b) for three fluxes. The data are compared with the linear chain model, where  $p = 2A/22 + 2.22$  (solid line).



the flux independence of the island shape transition is demonstrated. Islands which contain less than 300 atoms always exhibit a compact shape. Their perimeter scales with the square root of the island size. Finally for larger islands a deviation from this behavior is observed, and the dependence cannot be described in simple analytical terms. For island sizes exceeding  $\approx 3000$  atoms the island perimeter is found to be directly proportional to the island size.

This behavior can be modeled by the growth of a linear chain with a certain armwidth  $w$ . In this model, where the area associated with an adatom corresponds to the unit cell of the square substrate lattice, the relation between perimeter  $p$  and size  $A$  is:  $p = 2A/w + 2w$ . Using this model, the armwidth is obtained by fitting the data for the islands which exceed the critical island size to  $p = 2A/w + 2w$ . Since  $p(A)$  is given by the experimental data, the armwidth  $w$  is the only fit parameter. Several fits for island sizes above the critical value were performed and give almost identical results. Using the data of the island sizes above 1000 atoms, one obtains  $w = (21.98 \pm 0.25)$  atoms whereas for island sizes above 400 atoms,  $w = (21.87 \pm 0.18)$  atoms. The armwidth  $w = (22 \pm 1)$  is thus almost independent of the starting point. The critical island size, extracted with the linear chain model, is determined to  $A_c = w^2 = (480 \pm 20)$  atoms.

## 7.4 Thermodynamics of coherently strained islands

Tersoff and Tromp [156] have derived an expression for the energy of coherently strained (i.e. dislocation-free) epitaxial islands. They have considered three-dimensional, pyramid-shaped islands of width  $s$ , length  $t$ , and height  $h$  on a square substrate. Minimizing the total energy, including the excess surface and strain energy, they have found a spontaneous shape transition with increasing island size. Small islands have a compact, symmetric shape while above a critical island size they become elongated allowing for a better strain relaxation. While only the simple rectangular shape was studied, the basic result should be applicable equally well to the ramified shape of the monolayer high islands, particularly if the armlength substantially exceeds its width. With respect to a rectangular shaped island with width  $s$ , the branching of the ramified islands with armwidth  $w$  does not affect the perimeter for a given island size.

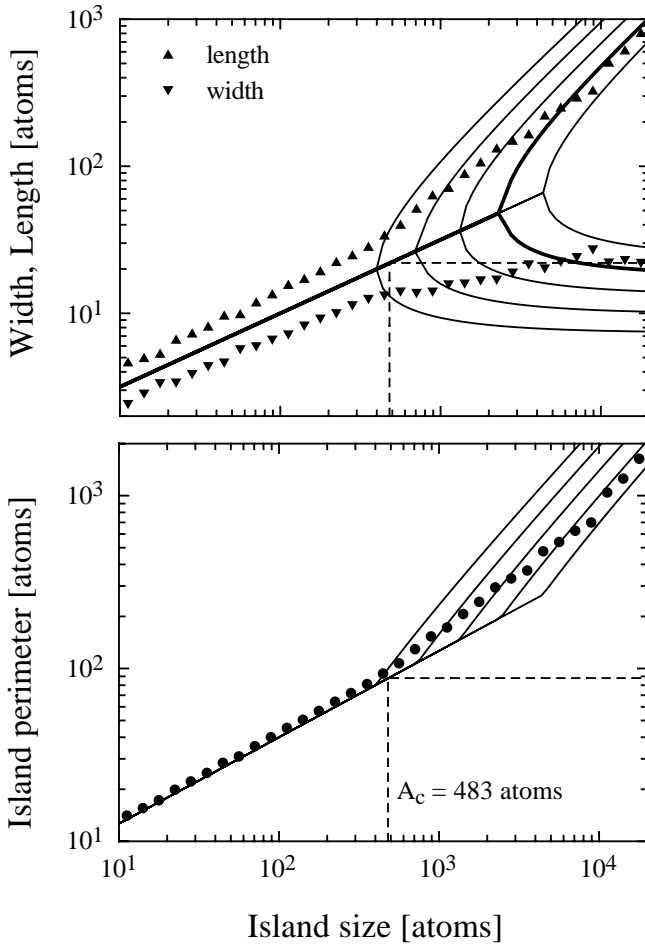


**Fig. 7.9.** The comparison between the model of Tersoff and Tromp [156] with  $b = 1.0, 1.3, 1.6, 1.9$ , and  $2.2$  and the experimental data. An increase of  $b$  shifts the shape transition to larger island sizes. In (a) width  $s$  and length  $t$  are derived from perimeter  $p$  and island size  $A$  assuming a rectangular island shape and compared with the prediction from the model. In (b) the island size–island perimeter relation in the model is compared to the averaged experimental data.



The model of Tersoff and Tromp [156] is based on different assumptions. (1) Corner effects are neglected. (Kink sites are energetically unfavorable and occur, therefore, infrequently.) (2) The surface energies of the substrate and of the islands are assumed to be equal, and (3) the strain does not change perpendicular to substrate surface. These assumptions are not severe limitations for the application to the present system. (1) We have found a preferential orientation of the island step edges in the close-packed directions, consequently corner effects are small. (2) The surface energies of substrate and adlayer are comparable (Cu:  $\approx 1850 \text{ mJ/m}^2$ , Ni:  $\approx 2450 \text{ mJ/m}^2$ ) [40]. (3) Perpendicular strain cannot change for monatomic-high islands. Hence, the approximate formula derived from Tersoff and Tromp should describe the system Cu/Ni(100) much better than previously examined examples for spontaneous shape transitions. Cu/Ni(100) is a suitable candidate to check the predictions of this theory in a quantitative manner.

In the model, the excess surface and strain energy is given by (Eq. (5) in Ref. [156]):

$$E = b \cdot (s + t) - s \cdot \ln(t) - t \cdot \ln(s) \quad (7.1)$$

Here, E is the normalized energy accounting for the extra surface energy and the energy change due to elastic relaxation, b is supposed to be a constant consisting of elastic constants, s and t are the island width and length, respectively. Since the island size  $A = st$ , one finds

$$E = b \cdot (s + \frac{A}{s}) - s \cdot \ln(\frac{A}{s}) - \frac{A}{s} \cdot \ln(s). \quad (7.2)$$

Minimizing E with respect to s, one obtains two identical solutions up to the critical island size  $A_c = \exp(2b+4)$  and two different solutions for the islands larger than  $A_c$ . Above  $A_c$  the width s shrinks from  $s_c = \exp(b+2)$  to  $s_\infty = \exp(b+1)$ . This behavior is shown in Fig. 7.9. Since width s and length t are ill defined due to the ramified morphology of the islands, we have derived these values from island perimeter and island size assuming a rectangular island shape. Up to the critical island size both s and t grow with the square root of island size as expected for compact islands. Above  $A_c$  they show the predicted splitting, whereas the width does not shrink but reaches a constant value. This discrepancy between model and experimental data is due to the particular, ramified shape of the two-dimensional islands. The model, a quasi one-dimensional

description, does not account for the growth in two equivalent directions and for finite size effects at the ends of the arms.

The width  $s$  in Equation 7.2 can be replaced by the perimeter, and, then one obtains the dependence between  $p$  and  $A$  within this model. This result is compared with the experimental data in Fig. 7.9. It is obviously impossible to find a specific value of  $b$  which describes the whole curve due to the discussed size limitation. Even if we take into consideration very large islands of  $10^4$  atoms, the width of about 22 atoms dominates  $p(A)$ . Accordingly, we have detected for such large islands an armwidth of 22 atoms corresponding to the critical armwidth and not the asymptotic armwidth of 8 atoms for very large islands. This is understood as the reason for the rather continuous transition between two-dimensional and one-dimensional growth whereas the model predicts a sharp transition at  $A_c$ . The equilibrium theory in the present status does not include these important effects and, therefore, fails in the quantitative description of our data. Nevertheless, the theory correctly predicts the spontaneous shape transition between two-dimensional and one-dimensional growth of monolayer-high copper islands on Ni(100) due to lattice strain and our experiments are considered as the first direct verification of the theoretical predictions of Tersoff and Tromp.

## 7.5 Relaxation of edge atoms at the island perimeter

The driving force for the observed preferential armwidth and thus for the ramification of the copper islands on Ni(100) is associated with the positive lattice mismatch of the two materials. The effect of compressive strain forces the copper atoms to shift outwards from the island's center. This behavior is especially important for the step edges, since the step edge atoms are only bound to one side and, therefore, free to relax outwards. They follow their natural lattice spacing which is larger than that of the substrate material. On the other hand, the lower coordination of the edge atoms favors (size dependent) inward relaxation [162] since less coordination tends to shrink bond lengths. In general, these two effects compete and it is *a priori* difficult to determine the dominant term. For the particular case of Cu/Ni(100) we have performed calculations using effective medium theory (EMT) [152] which reveal indeed a significant outward relaxation of the edge atoms, confirming the dominance of strain effects. The result for a relatively small rectangular island is shown by a hard sphere model in Fig. 7.10.

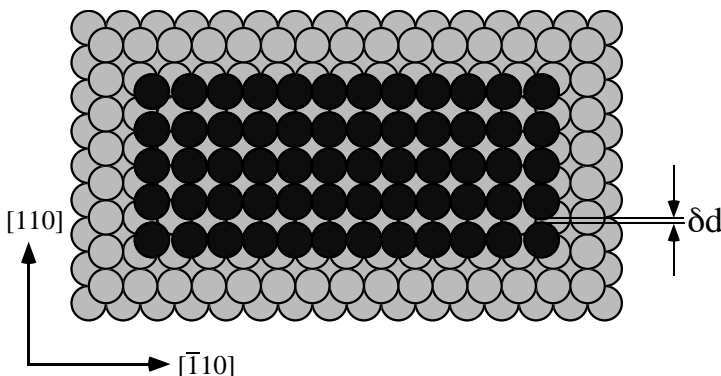


**Fig. 7.10.** Hard sphere model of a copper island on Ni(100) illustrating, with an exaggeration by a factor 30, edge atom relaxation of compressively strained heteroepitaxial island. The values for the outward relaxation are obtained from effective medium theory calculations.

The observation that the ramification of the islands involves preferential growth along the close-packed directions, indicates that there is high mobility along the edges and kink sites are energetically unfavorable. Both indications are corroborated by the EMT results. As for other square lattices the barrier for edge diffusion (285 meV) is found to be lower than for terrace diffusion (469 meV) and the barrier for corner diffusion (530 meV) is only slightly larger. Kink sites are energetically costly since they reduce coordination while leaving the number of edge atoms constant. Corner sites, however, are not very stable because these atoms are relaxed outwards with respect to both close-packed directions, giving rise to rounded corners. The formation of a constant armwidth also implies that the island growth becomes anisotropic and atoms attaching sideways diffuse towards a tip.

Experimental evidence for the relaxation of step edge atoms of monatomic-high copper islands on Ni(100) is provided by high-resolution low-energy electron diffraction (SPA-LEED) data. The intensity of the specular beam has been recorded at different substrate temperatures and at a scattering condition close to out-of-phase where the electrons scattered at adjacent terraces interfere destructively so that the experiment has maximum sensitivity for monatomic steps.

During the initial growth at high substrate temperatures (350 K), we have found the well-known behavior that the intensity decreases immediately after opening the

shutter due to the formation of islands leading to an increasing destructive interference of the specular beam. (cf. Fig. 7.11) At low substrate temperatures, e.g. at 130 K, (cf. Fig. 7.11), we observe a considerable intensity overshoot which has to be explained. Up to now such phenomena have been attributed to the smoothening of the substrate by the diffusing adatoms which nucleate at residual defects. Here, however, the temperature behavior contradicts this explanation since we observe the increasing intensity for low substrate temperature. Therefore, we conclude that this phenomenon is due to a difference in scattering behavior between the copper atoms at step edges (or in small islands) and on terraces. The island density differs for the two substrate temperatures by two orders of magnitude (see Fig. 7.12). That means, the only difference for the two growth conditions during the very early stages of growth is the relative number of step edge atoms which is much larger at the low growth temperature. Hence, for the present system the step edge atoms must have an enhanced reflectivity with respect to the terrace atoms. Forthcoming SPA-LEED experiments should provide quantitative support. Beside this effect one observes that the intensity minimum is not exactly located at a coverage of 0.5 ML but significantly shifted to higher values. It has been demonstrated in previous papers [163, 164] that this shift can be caused by the different scattering amplitude of (terrace) substrate atoms and (terrace) island adatoms neglecting form factor effects of the step edge atoms. For Cu/Ni(100), however, we have already shown in a previous study [165] depositing multilayer films at high substrate temperatures in the step flow mode, that the difference in scattering amplitude is small. Hence, the shift of the intensity minimum can only be explained by a significant amount of step edge atoms at half monolayer coverage showing a higher reflectivity. For coverages between 0.7 and 1 ML, the density of edge atoms is not very different for the different growth temperatures due to coalescence (in the low temperature regime) and ramified island growth (in the high temperature regime), consistent with the occurrence of the well pronounced minimum. At monolayer coverage, however, the island density is again higher for the low temperature regime and, therefore, we find a shift of the maximum to a coverage higher than 1 ML.

The intensity oscillations during the submonolayer growth of copper on Ni(100) can only be explained by a different scattering behavior of copper atoms at terraces and step edges which may be caused by the outward displacement of the step edge atoms from the ideal hollow site.

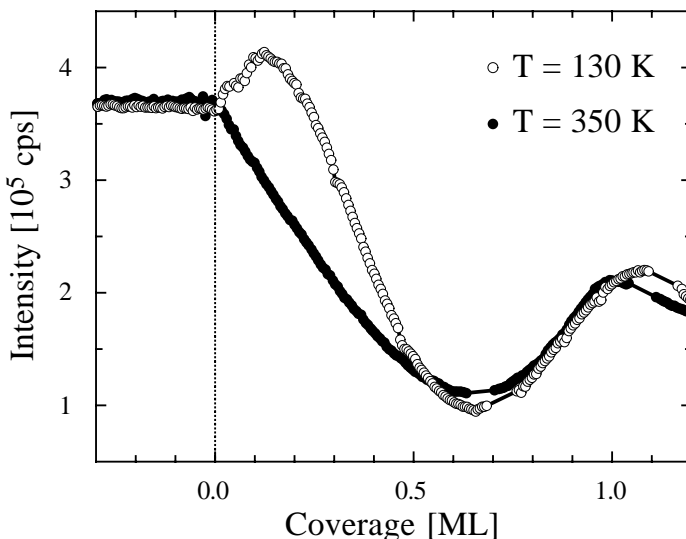


**Fig. 7.11.** The peak intensity of the specular beam during the initial stages of epitaxial growth of Cu/Ni(100) illustrating the different scattering behavior of step edge and terrace atoms. The scattering condition are  $E = 90$  eV, angle of incidence  $56^\circ$  and the azimuth  $18^\circ$  in the  $[110]$  direction.

Both strain relief mechanisms - island ramification and stripe formation - have in common that they involve displacements of atoms from the ideal pseudomorphic hollow site. For very small islands the strain can be relieved at the step edges even if they have a compact shape. Larger islands become ramified to optimize the ratio between perimeter and island size. Finally, the stripes appear when the strain relief at the island edges is no longer sufficient to minimize the total energy of the coherently strained islands.

The conclusion that ramification of islands is caused by the outward edge relaxation of copper atoms on Ni(100) due to the compressive strain is supported by the fact that copper forms ramified islands on Ni(100) but not on Pd(100) [62], although both substrate materials are very similar. The copper islands are compressively strained on Ni(100) and exhibit tensile strain on Pd(100) due to the positive and negative misfit, respectively.

## 7.6 Determination of strain energy from island shape

The island shape is understood as a result of the energy balance of the atomic bond energy within the islands and the strain energy due to the lattice mismatch with the substrate. Therefore, one can estimate the strain energy by the determination of the bond energy difference between the observed ramified islands and square islands of identical size. On the one hand, the islands try to attain compact shapes to optimize their binding energy. On the other hand, the strain energy associated with the island relaxation favors ramification. Based on bond counting, atoms inside of an island have 4 nearest neighbors in the adlayer, i. e. they are associated with 2 bonds per atom, whereby edge atoms have only 3 nearest neighbors in the adlayer associated with 1.5 bonds per atom. Therefore, the binding energy of an island corresponds to  $(2A - p/2) E_b$ , where  $A$  and  $p$  are expressed in the number of atoms forming the island and its perimeter, respectively. The binding energy per atom is therefore  $(2 - p/2A) E_b$ . For a square island,  $p = 4\sqrt{A}$ , and the bond energy per atom is given by  $(2 - 2/\sqrt{A}) E_b$ . For the ramified islands, however, we have found  $p = 2A/22 + 2\cdot 22$ , which results in a bond energy per atom of  $(2 - 1/22 - 22/A) E_b$ . Hence, in this simple bond counting model, for very large islands, the energy gain of forming square-shaped with respect to ramified islands,  $E^*$  is  $1/22$  of the dimer bond energy  $E_b$  per atom.

The dimer bond energy can be derived from the Arrhenius behavior of the island density in the saturation regime, when the size of the critical nucleus is larger than one and the migration barrier is known [43]. (The case of Cu/Ni(100) is discussed in Ref. [48], in detail.) In general, the value  $E_b$  is associated with a very large error bar, since there are usually only a few data points in a rather narrow temperature interval (see. Fig. 7.12). For the present study, we have assumed that the attempt frequency for the  $i = 1$  and for the  $i = 3$  regime is identical in agreement with previous studies [48]. A combined fit using all data of the  $i = 1$  and  $i = 3$  regimes including their error bars results not only in a well determined value for the migration barrier but also for the dimer bond energy. The obtained values for the migration barrier  $(0.37 \pm 0.03)$  eV, for the attempt frequency  $5 \times 10^{(11 \pm 1)}$  Hz, and for  $E_b = (0.34 \pm 0.03)$  eV confirm our previous study, but the error bar of  $E_b$  is reduced by a factor of 6 since the intersections of the  $i = 1$  and  $i = 3$  curves with ordinate are well defined due to the combined fit.  $E_b$  corresponds exactly to the value predicted by Evans and Bartelt [166] for a critical island transition temperature of 320 K based on

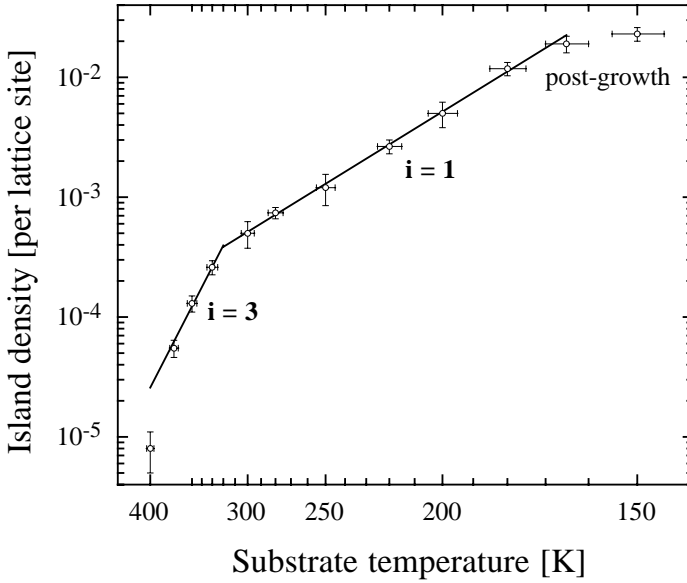


**Fig. 7.12.** Arrhenius plot of the measured saturation island density of Cu on Ni(100) (flux:  $1.5 \times 10^{-3}$  ML/s; coverage 0.1 ML).

kinetic Monte-Carlo simulations for square substrates. Using  $E_b = (0.34 \pm 0.03)$  eV, the energy gain  $E^*$  corresponds to  $(15 \pm 2)$  meV per island atom. This value, which is comparable to strain energies calculated from bulk properties, is relatively small and it is reasonable to assume that the difference can be overbalanced by the energy gain associated with the more effective strain relief at the longer edges of ramified islands.

## 7.7 Conclusion

The strain relaxation at the edges of copper islands on Ni(100) drives a transition from compact to ramified islands at a critical island size of about 500 atoms. The ramified islands exhibit a preferential armwidth of  $(22 \pm 1)$  atoms, which is associated with anisotropic strain relief. This phenomenon, predicted theoretically by Tersoff and Tromp, is expected to be of general importance in heteroepitaxy on square lattices with a positive lattice misfit. The present experiments show that ramified island shapes cannot only be caused by diffusion limitations at low temperatures but also by strain relief at elevated temperatures.

MBE growth, which is a dynamic, nonequilibrium phenomenon, is characterized by the competition between growth kinetics and thermodynamics. While thermodynamics embodies the essence of the behavior of the adlayer/substrate system in equilibrium, kinetics controls the pathway of the system towards an equilibrium state within the thermodynamic limitations. The present study gives an illustrative example of thermodynamic limitations: the ramified island growth at submonolayer coverages due to the lattice strain in heteroepitaxy cannot be outwitted by the choice of substrate temperature and deposition rate. On the other hand, one can employ this phenomenon to realize nanostructures even at elevated substrate temperatures. These nanostructures, which represent an equilibrium state of the heterosystem, are expected to be quite stable because they form within a large range of growth conditions.



## Chapter 8

# Outlook

The aim of this thesis was to contribute to a better understanding of the role of surface strain in epitaxial growth and nanostructure formation on metal surfaces. Two aspects are important in this context: On the one hand side, surfaces or thin films are generally under tensile stress. This often leads to formation of dislocation patterns in thin films or in some cases even to reconstruction of clean surfaces. These dislocation patterns may sensitively influence the local binding and diffusion potentials for adatoms and thus lead to unusual nucleation and growth scenarios. On the other hand, strain relaxation can be a decisive parameter in the formation of nanostructures, since e.g. strain energy minimization can be shape-determining. In the present work we addressed in particular the effect of surface dislocations on adatom mobility and the influence of lattice mismatch on the shape of two-dimensional islands, which were studied by means of variable temperature STM.

The effects of surface dislocations in thin film growth were investigated with the reconstructed Au(111) surface. We demonstrate that for the Al/Au(111) system the presence of the reconstruction dislocation pattern fundamentally modifies the nucleation behaviour. At low temperature, the dislocation lines of the reconstruction act as repulsive barriers for adatom diffusion and lead to confined nucleation. The usage of confined nucleation by a periodic strain relief pattern is a fascinating new route for the fabrication of nanostructures. Every surface exhibiting a dislocation pattern may be upon choice of the right growth conditions a suitable candidate to grow nanostructures of different sizes and shapes. Depending on the geometry of the dislocation pattern, different types of confinement can evolve: E.g. two-dimensional with hexagonal symmetry as for the case

of Ag nucleation on the second, strained layer of Ag on Pt(111) or unidimensional as for the Au(111) surface. Confined nucleation is up to now the only technique that permits to artificially create a high and rather uniform density of structures with a narrow size distribution in a massive parallel process. E.g. Brune et al. used the hexagonal moiré pattern evolving for the second monolayer of Cu on the Pt(111) surface to create laterally well ordered arrays of Fe islands [167] with a remarkable peaked size distribution. Another interesting example which might be used for growth of linear nanostructures is the uni-dimensional dislocation pattern evolving with thick Cu layers on Pd(110) [168]. In this case long nanowires are expected to form on the surface which might be a very interesting model system for e.g. one-dimensional magnetism. Nevertheless, the controlled fabrication of such nanostructures on a large scale is still an experimental challenge as the ability to modify dislocation patterns into a desired geometry by choosing adequate materials and growth conditions is still in its infancy.

The Cu on Ni(100) served as model system for the study of strain effects resulting from the lattice mismatch on the shape of two-dimensional islands. We demonstrate that for this particular system the strain is relieved at low coverages by a ramification of Cu islands exceeding a critical size. This study is the first experimental verification of such a shape transition in growth of monolayer-high islands. Similar mechanisms can certainly be expected for other systems with square symmetry and positive lattice misfit. The observed strain relief mechanism is thus of fundamental importance in heteroepitaxial growth and must be taken into account for the growth of nanostructures as it demonstrates that it might be impossible to grow small compact islands by self-assembly for certain systems. On the other hand, the ramification leads to an increased island perimeter, which might result in an increased chemical reactivity of the island. In order gain insight how to take advantage of island ramification further experiments need to be performed, not least from the perspective of catalysis.

An unexpected and striking observation for both the Al/Al(111) and Al/Au(111) systems are the extremely low diffusion barriers for adatom migration (for Al on Au(111) this concerns the diffusion barrier within the pseudomorphic stacking areas) and the exceptionally low values obtained for the attempt frequencies. The barriers of  $30 \pm 5$  and  $42 \pm 4$  meV are the lowest diffusion barriers ever measured for metal on metal systems. The attempt frequencies associated with these barriers, are by many orders of magnitude lower than the expected "universal" frequency for metal on metal systems ( $10^3 \text{ s}^{-1}$  and  $10^7 \text{ s}^{-1}$  vs.  $10^{13} \text{ s}^{-1}$  for Al/Au(111) and Al/Al(111) respectively). The fact that these migration barriers are close to surface phonon energies

(which may reach 20 meV at Al(111)) and thermal energies (e.g. 18 meV at 200 K) presumably strongly influences the surface diffusion as it has been proven that for some systems when  $kT_s$  is close to  $E_m$  *long jumps* are activated [90, 169]. This possibly puts into question the validity of the transition state theory ansatz for systems with very low diffusion barriers. A description within diffusion theory of liquids might be the adequate approach for an appropriate description of such systems. We believe that these findings are of general importance for surface diffusion as well as nucleation and growth scenarios in the low friction regime.



# Acronyms

<b>AES</b>	Auger electron spectroscopy
<b>ARUPS</b>	angle resolved ultraviolet photoelectron spectroscopy
<b>CVD</b>	chemical vapor deposition
<b>DFT-LDA</b>	density functional theory – local density approximation
<b>DLA</b>	diffusion limited aggregation
<b>EAM</b>	embedded atom method
<b>EMT</b>	effective medium theory
<b>fcc</b>	faced centered cubic
<b>FIM</b>	field ion microscope
<b>FWHM</b>	full-width at half-maximum
<b>HAS</b>	helium atom scattering
<b>hcp</b>	hexagonal close-packed
<b>LDA</b>	local density approximation
<b>LEED</b>	low energy electron diffraction
<b>MBE</b>	molecular beam epitaxy
<b>MD</b>	molecular dynamics
<b>ML</b>	monolayer
<b>SPA-LEED</b>	spot profile analysis low energy electron diffraction
<b>STM</b>	scanning tunneling microscopy
<b>TST</b>	transition state theory
<b>UHV</b>	ultra high vacuum
<b>UPS</b>	ultraviolet photoelectron spectroscopy
<b>XPS</b>	x-ray photoelectron spectroscopy



# Bibliography

- [1] D. H. Lowndes, D. B. Geohegan, A. A. Puretsky, D. P. Norton and C. M. Rouleau, *Science* **273**, 898 (1996).
- [2] R. F. Service, *Science* **273**, 878 (1996).
- [3] J. Faist, F. Capasso, D. L. Sivco, C. Sirtori, A. L. Hutchinson and A. Y. Cho, *Science* **264**, 553 (1994).
- [4] M. F. Doerner and R. L. White, *Mat. Res. Soc. Bull.* **21**, 28 (1996).
- [5] W. D. Sproul, *Nature* **273**, 889 (1996).
- [6] M. F. Crommie, C. P. Lutz and D. M. Eigler, *Science* **262**, 218 (1993).
- [7] P. Avouris, *Atomic and Nanometer Scale Modification of Materials: Fundamentals and Applications*, (Kluwer, Dordrecht, Netherlands, 1993).
- [8] P. Avouris, *Accounts Chem. Res.* **28**, 95 (1995).
- [9] H. Röder, E. Hahn, H. Brune, J. P. Bucher and K. Kern, *Nature* **366**, 141 (1993).
- [10] T. Gritsch, D. Coulman, R. J. Behm and G. Ertl, *Surf. Sci.* **257**, 297 (1991).
- [11] J. V. Barth, H. Brune, G. Ertl and R. J. Behm, *Phys. Rev. B* **42**, 9307 (1990).
- [12] D. P. Woodruff, *J. Phys. Condens. Matter.* **6**, 6067 (1994).
- [13] L. P. Nielsen, F. Besenbacher, E. Laegsgaard and I. Stensgaard, *Phys. Rev. B.* **44**, 13156 (1991).
- [14] J. Yoshinobu, *Phys. Rev. B* **51**, 4529 (1995).
- [15] H. Röder, R. Schuster, H. Brune and K. Kern, *Phys. Rev. Lett.* **71**, 2086 (1993).

- [16] L. P. Nielsen, F. Besenbacher, E. Laegsgaard, I. Stensgaard, C. Engdahl, P. Stoltze, K. W. Jacobsen and J. K. Nørskov, Phys. Rev. Lett. **71**, 754 (1993).
- [17] J. Tersoff, Phys. Rev. Lett. **74**, 434 (1995).
- [18] J. A. Meyer, J. D. Baikia, E. Kopatzki and R. J. Behm, Surf. Sci. **365**, L647 (1996).
- [19] F. Besenbacher, L. P. Nielsen and P. T. Sprunger, in *Growth and Properties of Ultrathin Epitaxial Layers*, vol. 8, D. A. King and D. P. Woodruff, Eds. (The Chemical Physics of Solid Surfaces, and Heterogeneous Catalysis, Amsterdam, 1997).
- [20] M. Bott, T. Michely and G. Comsa, Rev. Sci. Instrum. **66**, 4135 (1995).
- [21] H. Brune, H. Röder, K. Bromann and K. Kern, Thin Solid Films **264**, 230 (1995).
- [22] K. Besocke, Surf. Sci. **181**, 145 (1987).
- [23] G. Binnig and D. P. E. Smith, Rev. Sci. Instrum. **57**, 1688 (1986).
- [24] H. Röder, Ph.D. Thesis, Ecole Polytechnique Fédérale de Lausanne, (1994).
- [25] K. Bromann, Ph.D. Thesis, EPFL, (1997).
- [26] B. Gasser, A. Menck, H. Brune and K. Kern, Rev. Sci. Instrum. **67**, 1925 (1996).
- [27] Besocke-Delta-Phi-Elektronik, Postfach 2243, 52428 Jülich, Germany.
- [28] STM 2000, RHK Technology Inc., Rochester Hills, MI 48309, USA.
- [29] Eurotherm 818, Eurotherm Regler GmbH, Limburg, Germany.
- [30] Staveley Sensors Inc, East Hartford, England. EBL product line (piezo used: EBL#1).
- [31] M. Okano, K. Kajimura, S. Wakiyama, F. Sakai, W. Mizutani and M. Ono, J. Vac. Sci. Technol. A **5**, 3313 (1987).
- [32] S. Günter, Ph.D. Thesis, Ulm, (1995).
- [33] S. Behler, M. K. Rose, D. F. Ogletree and M. Salmeron, Rev. Sci. Instrum. **68**, 124 (1997).
- [34] L. Nedelmann, Ph.D. Thesis, EPFL, (1997).
- [35] H. Ibach, in Proceedings of *17. IFF Ferienkurs* K.-f. Jülich, Eds. 1986).
- [36] E. Bauer, Z. Kristallogr. **110**, 372 (1958).
- [37] A. Madhukar, Surf. Sci. **132**, 344 (1983).
- [38] E. Bauer and H. Poppa, Thin Solid Films **12**, 167 (1972).
- [39] E. Bauer, Appl. Surf. Sci. **11/12**, 479 (1982).
- [40] R. Kern, G. L. Lay and J. J. Metois, in *Current Topics in Materials Science*, Vol. 3, vol. E. Kaldis, Eds. (North-Holland, 1979), pp. 135.



- [41] J. H. v. d. Merwe, D. L. Tönsing and P. M. Stoop, *Surf. Sci.* **312**, 387 (1994).
- [42] G. Ehrlich, *Surf. Sci.* **246**, 1 (1991).
- [43] J. A. Venables, G. D. T. Spiller and M. Hanbücken, *Rep. Prog. Phys.* **47**, 399 (1984).
- [44] G. Rosenfeld, B. Poelsema and G. Comsa, in *Growth and properties of ultrathin epitaxial growth*, vol. 8, D. A. King and D. P. Woodruff, Eds. (The Chemical Physics of Solid Surfaces, and Heterogeneous Catalysis, Amsterdam, 1997), pp. 66.
- [45] D. R. Lide, *Handbook of chemistry and physics*, vol. 76. ed., (CRC Press, (Boca Raton - New York - London - Tokyo), (1995).
- [46] H. Brune, *Surf. Sci. Rep.* **in press**, (1998).
- [47] J. G. Amar and F. Family, *Phys. Rev. Lett.* **74**, 2066 (1995).
- [48] B. Müller, B. Fischer, L. Nedelmann, H. Brune and K. Kern, *Phys. Rev. B* **54**, 17858 (1996).
- [49] D. Pramanik, *MRS Bulletin* **20**, 57 (1995).
- [50] R. Stumpf and M. Scheffler, *Phys. Rev. B* **53**, 4958 (1996).
- [51] B. J. Hinch, R. B. Doak and L. H. Dubois, *Surf. Sci.* **286**, 261 (1993).
- [52] G. Polanski and J. P. Toennies, *Surf. Sci.* **260**, 250 (1992).
- [53] W. J. Wytenburg, R. M. Ormerod and R. M. Lambert, *Surf. Sci.* **282**, 205 (1993).
- [54] C. J. Barnes, H. Asonen, A. Salokatve and M. Pessa, *Surf. Sci.* **184**, 163 (1987).
- [55] B. Frick and K. Jacobi, *Surf. Sci.* **178**, 907 (1986).
- [56] A. Bogicevic (private communication).
- [57] Y. W. Mo, J. Kleiner, M. B. Webb and M. G. Lagally, *Phys. Rev. Lett.* **66**, 1998 (1991).
- [58] B. S. Swartzentruber, *Phys. Rev. Lett.* **76**, 459 (1996).
- [59] K. Bromann, H. Brune, H. Röder and K. Kern, *Phys. Rev. Lett.* **75**, 677 (1995).
- [60] J. A. Meyer, J. Viemoeth, H. A. v. d. Vegt, E. Vlieg and R. J. Behm, *Phys. Rev. B* **51**, 14790 (1995).
- [61] T. Michely, M. Hohage, M. Bott and G. Comsa, *Phys. Rev. Lett.* **70**, 3943 (1993).
- [62] E. Hahn, E. Kampshoff, N. Wälchli and K. Kern, *Phys. Rev. Lett.* **74**, 1803 (1995).

- [63] S. Günther, E. Kopatzki, M. C. Bartelt, J. W. Evans and R. J. Behm, Phys. Rev. Lett. **73**, 553 (1994).
- [64] R. Q. Hwang, J. Schröder, C. Günther and R. J. Behm, Phys. Rev. Lett. **67**, 3279 (1991).
- [65] M. Hohage, M. Bott, M. Morgenstern, Z. Zhang, T. Michely and G. Comsa, Phys. Rev. Lett. **76**, 2366 (1996).
- [66] H. Brune, K. Bromann, J. Jacobsen, K. Jacobsen, P. Stoltze, J. Nørskov and K. Kern, Surf. Sci. Lett. **349**, L115 (1996).
- [67] H. Brune, C. Romainczyk, H. Röder and K. Kern, Nature **369**, 469 (1994).
- [68] H. Röder, K. Bromann, H. Brune and K. Kern, Phys. Rev. Lett. **74**, 3217 (1995).
- [69] R. Stumpf and M. Scheffler, Phys. Rev. Lett. **72**, 254 (1994).
- [70] P. Ruggerone, C. Ratsch and M. Scheffler, in *Growth and Properties of Ultrathin Epitaxial Layers*, vol. 8, D. A. King and D. P. Woodruff, Eds. (The Chemical Physics of Solid Surfaces, and Heterogeneous Catalysis, Amsterdam, 1997).
- [71] W. Meyer and H. Neldel, Z. Tech. Phys. **12**, 588 (1937).
- [72] G. Boisvert, L. J. Lewis and A. Yelon, Phys. Rev. Lett. **75**, 469 (1995).
- [73] J. A. Gaspar, A. G. Eguluz, K. D. Tsuei and E. W. Plummer, Phys. Rev. Lett. **67**, 2854 (1991).
- [74] A. Lock, J. P. Toennies, C. Wöll, V. Bortolani, A. Franchini and G. Santoro, Phys. Rev. B **37**, 7087 (1988).
- [75] T. A. Witten and L. M. Sander, Phys. Rev. Lett. **47**, 1400 (1981).
- [76] T. A. Witten and L. M. Sander, Phys. Rev. B **27**, 5686 (1983).
- [77] H. Brune, H. Röder, C. Romainczyk, C. Boragno and K. Kern, Appl. Phys. A **60**, 167 (1995).
- [78] J. Jacobsen, K. W. Jacobsen and J. K. Nørskov, Surf. Sci. **359**, 37 (1996).
- [79] J. Jacobsen, K. W. Jacobsen, P. Stoltze and J. K. Nørskov, Phys. Rev. Lett. **74**, 2295 (1995).
- [80] C. Günther, S. Günther, E. Kopatzki, R. Q. Hwang, J. Schröder, J. Vrijmoeth and R. J. Behm, Ber. Bunsenges. Phys. Chem. **97**, 522 (1993).
- [81] M. G. Lagally, Physics Today **November**, 24 (1993).
- [82] H. Brune and K. Kern, in *Growth and Properties of Ultrathin Epitaxial Layers*, vol. 8, D. A. King and D. P. Woodruff, Eds. (The Chemical Physics of Solid Surfaces, and Heterogeneous Catalysis, Amsterdam, 1997), pp. 149.
- [83] G. Ehrlich, Surf. Sci. **331-333**, 865 (1995).
- [84] G. L. Kellogg, Surf. Sci. Rep. **21**, 1 (1994).

- [85] H. Brune, H. Röder, C. Boragno and K. Kern, Phys. Rev. Lett. **73**, 1955 (1994).
- [86] J. A. Strosio and D. T. Pierce, Phys. Rev. B **49**, 8522 (1994).
- [87] M. Bott, M. Hohage, M. Morgenstern, T. Michely and G. Comsa, Phys. Rev. Lett. **76**, 1304 (1996).
- [88] J. P. Bucher, E. Hahn, P. Fernandez, C. Massobrio and K. Kern, Europhys. Lett. **27**, 473 (1994).
- [89] T. R. Linderoth, J. J. Mortensen, K. W. Jacobsen, E. Laegsgaard, I. Stensgaard and F. Besenbacher, Phys. Rev. Lett. **77**, 87 (1996).
- [90] T. R. Linderoth, S. Horch, E. Lægsgaard, I. Stensgaard and F. Besenbacher, Phys. Rev. Lett. **78**, 4978 (1997).
- [91] J. W. Evans and M. C. Bartelt, J. Vac. Sci. Technol. **A 12**, 1800 (1994).
- [92] M. Bott, M. Hohage, T. Michely and G. Comsa, Phys. Rev. Lett. **70**, 1489 (1993).
- [93] J. A. Meyer, P. Schmid and R. J. Behm, Phys. Rev. Lett. **74**, 3864 (1995).
- [94] H. Brune, K. Bromann, H. Röder, K. Kern, J. Jacobsen, P. Stolze, K. Jacobsen and J. Nørskov, Phys. Rev. B **52**, R14380 (1995).
- [95] T. Michely, M. Hohage, S. Esch and G. Comsa, Surf. Sci. **349**, L89 (1996).
- [96] D. D. Chambliss, R. J. Wilson and S. Chiang, Phys. Rev. Lett. **66**, 1721 (1991).
- [97] D. D. Chambliss, R. J. Wilson and S. Chiang, J. Vac. Sci. Technol. B **9**, 933 (1991).
- [98] B. Voigtländer, G. Meyer and N. M. Amer, Surf. Sci. **255**, L529 (1991).
- [99] J. A. Strosio, D. T. Pierce, R. A. Dragoset and P. N. First, J. Vac. Sci. Technol. A **10**, 1981 (1992).
- [100] B. Voigtländer, G. Meyer and N. M. Amer, Phys. Rev. B **44**, 10354 (1991).
- [101] J. Wollschläger and N. M. Amer, Surf. Sci. **277**, 1 (1992).
- [102] M. A. Krzyzowski, Berichte des Forschungszentrums Jülich #3077, (1995).
- [103] M. Mansfield and R. J. Needs, J. Phys.: Condens. Matter **2**, 2361 (1990).
- [104] A. H. Smith, R. A. Barker and P. J. Estrup, Surf. Sci. **136**, 327 (1994).
- [105] L. D. Roelofs, J. W. Chung, S. C. Ying and P. J. Estrup, Phys. Rev. B **33**, 6537 (1986).
- [106] A. R. Sandy, S. G. J. Mochrie, D. M. Zehner, G. Grübel, K. G. Huang and D. Gibbs, Phys. Rev. Lett. **68**, 2192 (1992).
- [107] A. Zangwill, in *Physics at surfaces*, vol. Chapter 5, C. U. Press, Eds. Cambridge, 1992), .
- [108] Y. Hasegawa and P. Avouris, Science **258**, 1763 (1992).

- [109] B. Fischer, J. V. Barth, A. Fricke, L. Nedelmann and K. Kern, *Surf. Sci.* **389**, 366 (1997).
- [110] M. A. Krzyzowski, Ph.D. Thesis, Universität Bonn, (1995).
- [111] J. A. Meyer and R. J. Behm, *Surf. Sci.* **322**, L275 (1995).
- [112] J. A. Venables, *Philos. Mag.* **17**, 697 (1973).
- [113] J. J. Mortensen, B. Hammer, O. H. Nielsen, K. W. Jacobsen and J. K. Nørskov, in *Elementary Processes in Excitations and Reactions on Solid Surfaces*, Solid State Sciences Series, vol. 121, A. Okiji, H. Kasai and K. Makoshi, Eds. (Springer, 1996), pp. 173.
- [114] J. Jacobsen, K. W. Jacobsen and P. Stoltze, *Surf. Sci.* **317**, 8 (1994).
- [115] J. Jacobsen, Ph.D. Thesis, Technical University of Denmark, (1996).
- [116] D. E. Wolf, in *Scale Invariance, Interfaces, and Non-Equilibrium Dynamics*, vol. M. Droz, K. J. McKane, J. Vannimenus and D. E. Wolf, Eds. (Plenum, New York, 1994), pp. 1.
- [117] A. F. Voter, *Phys. Rev. B* **34**, 6819 (1986).
- [118] J. Maddox, *Nature* **372**, 403 (1994).
- [119] M. C. Tringides and R. Gomer, *Surf. Sci.* **155**, 254 (1985).
- [120] G. Ehrlich, *J. Chem. Phys.* **44**, 1050 (1966).
- [121] H. Brune, G. S. Bales, C. Boragno, J. Jacobsen and K. Kern, *Phys. Rev. B* **to be published**, (1998).
- [122] G. Ayrault and G. Ehrlich, *J. Chem. Phys.* **60**, 281 (1974).
- [123] S. C. Wang and G. Ehrlich, *Surf. Sci.* **239**, 301 (1990).
- [124] S. C. Wang and G. Ehrlich, *Phys. Rev. Lett.* **62**, 2297 (1989).
- [125] A. F. Voter and J. D. Doll, *J. Chem. Phys.* **80**, 5832 (1984).
- [126] S. Liu, L. Bönig, J. Detchev and H. Metiu, *Phys. Rev. Lett.* **74**, 4495 (1995).
- [127] P. J. Feibelman, J. S. Nelson and G. L. Kellogg, *Phys. Rev. B* **49**, 10548 (1994).
- [128] H. Brune, *Thèse d'habilitation* EPFL (1997).
- [129] G. S. Bales and D. C. Chrzan, *Phys. Rev. B* **50**, 6057 (1994).
- [130] A. R. Sandy, S. G. J. Mochrie, D. M. Zehner, K. G. Huang and D. Gibbs, *Phys. Rev. B* **43**, 4667 (1991).
- [131] U. Harten, A. M. Lahee, J. P. Toennies and C. Wöll, *Phys. Rev. Lett.* **54**, 2619 (1985).
- [132] J. V. Barth, R. J. Behm and G. Ertl, *Surf. Sci.* **302**, L319 (1994).
- [133] E. I. Altman and R. J. Colton, *Surf. Sci.* **304**, L400 (1994).
- [134] J. V. Barth, R. J. Behm and G. Ertl, *Surf. Sci.* **341**, 62 (1995).
- [135] A. R. Miedema, *Z. Metallk.* **69**, 287 (1978).

- [136] W. R. Tyson, *Can. Metall. Quart.* **14**, 307 (1975).
- [137] H. Brune, K. Bromann, K. Kern, J. Jacobsen, P. Stoltze, K. Jacobsen and J. Nørskov, *Surf. Sci. Lett.* **349**, L115 (1996).
- [138] J. W. Evans and M. C. Bartelt, *Langmuir* **12**, 217 (1996).
- [139] D. D. Chambliss and K. E. Johnson, *Phys. Rev. B* **50**, 5012 (1994).
- [140] M. Hohage, T. Micheley and G. Comsa, *Surf. Sci.* **337**, 249 (1995).
- [141] H. Büchler and K.-J. Range, *J. Less-Common. Met.* **160**, 143 (1990).
- [142] J. L. Murray, H. Okamoto and T. B. Massalski, *Bull. Alloy Phase Diag.* **8**, 20 (1987).
- [143] H. Okamoto, *J. Phase Equil.* **12**, 114 (1991).
- [144] J. L. Stevens and R. Q. Hwang, *Phys. Rev. Lett.* **74**, 2078 (1995).
- [145] B. E. Koel, A. Sellidji and M. T. Paffet, *Phys. Rev. B* **46**, 7846 (1992).
- [146] M. Ellner, K. Kolatschek and B. Predel, *J. Less-Common. Met.* **170**, 171 (1991).
- [147] M. Ellner and B. Predel, in *Intermetallic compounds Vol. 1*, vol. J. H. Westbrook and R. L. Fleischer, Eds. (John Wiley & Sons, 1994), pp. 91.
- [148] Z. Zhang, X. Chen and M. G. Lagally, *Phys. Rev. Lett.* **73**, 1829 (1994).
- [149] E. Kopatzki, S. Günther, W. Nichtl-Pecher and R. J. Behm, *Surf. Sci.* **284**, 154 (1993).
- [150] J. A. Strosio, D. T. Pierce and R. A. Dragoset, *Phys. Rev. Lett.* **70**, 3615 (1995).
- [151] C. L. Liu, *Surf. Sci.* **316**, 294 (1994).
- [152] P. Stoltze, *J. Phys. Condens. Matter* **6**, 9495 (1994).
- [153] M. A. Grinfeld, *Sov. Phys. Dokl.* **31**, 831 (1986).
- [154] D. Srolovitz, *Acta Metall.* **37**, 621 (1989).
- [155] B. J. Spencer, P. W. Voorhees and S. H. Davis, *Phys. Rev. Lett.* **67**, 3696 (1991).
- [156] J. Tersoff and R. M. Tromp, *Phys. Rev. Lett.* **70**, 2782 (1993).
- [157] B. Müller, B. Fischer, L. Nedelmann, A. Fricke and K. Kern, *Phys. Rev. Lett.* **76**, 2358 (1996).
- [158] B. Müller, L. Nedelmann, B. Fischer, A. Fricke and K. Kern, *J. Vac. Sci. Technol. A* **14**, 1878 (1996).
- [159] J. P. Bucher, E. Hahn, P. Fernandez, C. Massobrio and K. Kern, *Europhys. Lett.* **27**, 473 (1994).
- [160] F. B. Rasmussen, J. Baker, M. Nielsen and R. Feidenhans'l, *Phys. Rev. Lett.* **79**, 4413 (1997).
- [161] J. Tersoff, *Phys. Rev. Lett.* **74**, 434 (1994).

- [162] J. Fassbender, U. May, B. Schirmer, R. M. Jungblut, B. Hillebrands and G. Güntherodt, Phys. Rev. Lett. **75**, 4476 (1995).
- [163] M. Henzler, C. Homann, U. Malaske and J. Wollschläger, Phys. Rev. B **52**, 17060 (1995).
- [164] J. Wollschläger and A. Meier, Apl. Surf. Sci. **104/105**, 392 (1996).
- [165] L. Nedelmann, B. Müller, B. Fischer, K. Kern, D. Erdös and J. Wollschläger, Surf. Sci. **376**, 113 (1997).
- [166] J. W. Evans and M. C. Bartelt, in *Surface diffusion: atomistic and collective processes*, vol. M. Scheffler and M. C. Tringides, Eds. (NATO ASI, New York, 1997), pp. in press.
- [167] H. Brune, M. Giovannini, K. Bromann, K. Kern, Nature, submitted.
- [168] E. Hahn, E. Kampshoff, A. Fricke, J. P. Bucher, K. Kern, Surf. Sci. **319**, 277 (1994).
- [169] K. D. Dobbs and D. J. Doren, J. Chem. **97**, 3722 (1992).

# Acknowledgements - Remerciements!

Un grand merci à tous les membres de l'institut de physique expérimentale pour l'excellente atmosphère dans laquelle j'ai pu accomplir ce travail de doctorat. En particulier, je souhaite exprimer ma plus sincère gratitude aux diverses personnes qui ont contribué à l'élaboration de cette thèse. Ce sont:

Le professeur Klaus Kern, qui m'a donné la possibilité d'effectuer ce travail dans son groupe et qui m'a guidé tout au long de ma thèse.

Johannes Barth, Harri Brune, Alex Fricke et Bert Müller, mes différents post-docs durant ces années, pour leur aide précieuse, leur compétences ainsi que leurs innombrables conseils et suggestions concernant le manuscrit et l'exposé oral. En particulier, la version définitive de ce travail doit énormément à Johannes.

MM. les membres du jury: Prof. B. Deveaud-Pledran, Prof. F. Besenbacher, Dr. J. Bonneville et Prof. J. Osterwalder pour avoir bien voulu juger ce travail.

Lorenz Nedelmann pour son aide lors des mesures et de l'analyse de données; spécialement en ce qui concerne le chapitre 7 de ma thèse.

Max Epple et Bork-Martial Blanc mes chers collègues de bureau pour m'avoir soutenu avec des quantités incroyables de gâteau, biscuits et autres denrées alimentaires. Un merci spécial à Martial pour ses nombreuses corrections d'orthographe que j'ai énormément appréciées (et abusées) et pour la correction de ces remerciements.

Toute l'équipe du secrétariat, de l'atelier de mécanique et d'électronique de l'IPE pour leur grand soutien et leur disponibilité tout au long de ce travail.

Caire-Lise Bandelier pour l'énorme travail qu'elle y a investi afin que les figures et images de cette thèse soient les plus parfaites que possible.

Mes parents, mes amis et surtout Nathalie qui m'a donné de très précieux coups de mains à la veille de diverses échéances et, surtout pour ses encouragements dont j'avais besoin à certains moments plus difficiles.



# Curriculum vitae

## Données personnelles

Nom:	Bjørn Fischer
Date de naissance:	25 juillet 1966
Nationalité:	suisse, originaire de Coppet
Etat-civil:	marié

## Formation

1973-1982	Scolarité obligatoire (à Nyon et Coppet).
1982-1986	Ecole d'ingénieurs de Genève en section mécanique.
26 juin 1986	Obtention du diplôme d'ingénieur ETS en mécanique.
1986-1987	Université de Genève (faculté des sciences).
1987-1994	Ecole Polytechnique de Lausanne en section de physique.
30 mars 1994	Obtention du diplôme d'ingénieur physicien EPF.
1994-1998	Thèse à l'institut de physique expérimentale de l'EPFL.